



GEORG-AUGUST-UNIVERSITÄT
GÖTTINGEN

FAKULTÄT FÜR PHYSIK



MAX-PLANCK-GESELLSCHAFT

BACHELOR THESIS

Computer simulations of discotic liquid crystals in nanoconfinement

Computersimulation von discotischen Flüssigkristallen in Nanoconfinement

Due: 13. April 2015

Arne Wolf Zantop

arne.zantop@stud.uni-goettingen.de

Advisor & First Referee: **Dr. Marco G. Mazza**

Second Referee: **Prof. Dr. Jörg Enderlein**

Max-Planck-Institut für
Dynamik und Selbstorganisation

Abteilung
Dynamik Komplexer Fluide



Abstract

Discotics, that is liquid crystals formed by disk-like molecules, draw interest due to their applications as conductive nanowires confined in nanoporous templates. In this work we study the influence of different sizes of cylindrical nanoconfinement and surface anchoring on the phase behaviour of a discotic Gay-Berne fluid. The phase behaviour strongly differs from the bulk. We observe radially aligned nematic and radial poly-domain columnar configurations. Mono-domain hexagonal columnar phases were found with both face- and edge-on anchoring. Furthermore, geometrical frustration of hexagonal columnar and crystal phases is observed. Smaller pores with edge-on anchoring exhibit a configuration with a columnar outer layer and an isotropic core. The phase behaviour is investigated by means of several order parameters, some specific for the special orientational configuration in cylindrical confinement. We investigate the structure by means of radial distribution functions, and the dynamics using van Hove correlation functions.

Zusammenfassung

Discotische Flüssigkristalle, welche aus scheibenförmigen Molekülen bestehen, wecken aufgrund ihrer Anwendung als Nanokabel, in auf Nanoscala porösen Materialien eingebracht, großes Interesse. In dieser Arbeit wird die Auswirkung von zylindrischer Eingrenzung mit orientierungsabhängiger Wechselwirkung auf das Phasendiagramm eines Gay-Berne Modells für discotische Flüssigkristalle untersucht. Das resultierende Phasendiagramm zeigt deutliche Unterschiede zum unbegrenzten Gegenstück. Es treten radial angeordnete nematische und säulenartige Phasen auf, letztere aus vielen Domänen bestehend. Hexagonale säulenartige Phasen mit nur einer einzigen Domäne traten sowohl entlang der Zylinderachse ausgerichtet, als auch radial ausgerichtet auf. Es wurde auch eine Unterdrückung der Hexagonalen Phase und Kristallphase durch die zylindrische Eingrenzung beobachtet. Unter dem Einfluss Wandwechselwirkung, welche die nematische Ausrichtung senkrecht zur Oberfläche bevorzugt, traten Konfigurationen mit säulenartige angeordneter Hülle und ungeordnetem Zentrum auf. Die unterschiedlichen Phasen wurden mittels verschiedener Ordnungsparameter, einige davon speziell für die zylindrische Geometrie untersucht. Die Strukturen wurden mittels Paarkorrelationsfunktionen, die Dynamik wurde mittels van Hove Korrelationsfunktionen untersucht.

Contents

1	Theory	1
1.1	Introduction	1
1.2	Basics of Liquid Crystals	1
1.2.1	Chemical Structure	2
1.2.2	Discotic Liquid Crystal Phases	3
1.3	Statistical Mechanics	5
1.3.1	Ergodic Hypotesis	6
1.4	Computational Methods	7
1.4.1	Equations of Motion	7
1.4.2	Finite Difference Method of the Verlet Algorithm	8
1.4.3	Intermolecular Potential Model	9
1.4.3.1	Site-Site Potentials	9
1.4.3.2	Overlap Potential	9
1.4.3.3	Gay-Berne Model	10
1.4.3.4	Improvement	11
1.4.4	Reduced Units	12
1.4.5	Fluid-Wall Interaction	12
1.5	Order Parameters and Correlation Functions	13
1.5.1	Structural Properties	13
1.5.1.1	Scalar and Tensor Order Parameter	13
1.5.1.2	Maier-Saupe Theory	15
1.5.1.3	Hexagonal Order Parameter	17
1.5.1.4	Local Nematic Order Parameter	18
1.5.1.5	Radial Distribution Function	18
1.5.2	Additional Structural Properties	19
1.5.2.1	Radial Nematic Order Parameter	19
1.5.2.2	Axial Nematic Order Parameter	19
1.5.3	Dynamic Properties	20
1.5.3.1	Van Hove Function	20
1.5.3.2	Mean Square Displacement and Self Diffusion	21
2	Implementation	22
2.1	Model Parameters	22
2.2	Simulations	22
2.2.1	Confinement	23
2.3	Data processing	23
3	Results	25
3.1	Bulk	25
3.1.1	Order Parameters	25
3.1.2	Structural Properties	26
3.1.3	Dynamic Properties	27
3.1.3.1	Self-Diffusion and Mean Square Displacement	27
3.1.4	Phase Diagram	32
3.2	Confined System	33
3.2.1	Face-on Anchoring	34
3.2.1.1	Pore Diameter $10\sigma_{ee}$	34
3.2.1.2	Pore Diameter $5\sigma_{ee}$	40
3.2.1.3	Pore Diameter $3\sigma_{ee}$	44
3.2.2	Edge-on Anchoring	46
3.2.2.1	Pore Diameter $10\sigma_{ee}$	46

3.2.2.2	Pore Diameter $5\sigma_{ee}$	48
3.2.2.3	Pore Diameter $3\sigma_{ee}$	51
3.3	Discussion	52
4	Conclusions	53
4.1	Face-on Anchoring	53
4.2	Edge-on Anchoring	54
Appendix		I
A.1	Fluid-Wall Force	I
A.2	Code	III
A.2.1	Maier-Saupe Theory	III
A.2.2	Hexagonal Order Parameter	IV
Acknowledgements		VII
Erklärung		IX

Chapter 1: Theory

1.1 Introduction

Nowadays, liquid crystals play a very important role in everyday's life. Liquid crystal displays are ubiquitous in computer monitors. They made displays flat and cheap. Although the knowledge of liquid crystals is rather old, the field of research is still very active. Besides the use in liquid crystal displays, liquid crystals are applied in optics [1], thermometers [2] and as laser medium [3]. Liquid crystals are very beneficial because they have self-ordering and defect-healing properties, as one can easily see by gently pressing on the surface of a liquid crystal display. Therefore there is interest in the development of further applications of liquid crystals. One of these could be electrically conductive nanowires [4] made out of discotics or batteries with liquid crystalline room temperature ionic liquids [5]. To investigate dynamical properties of liquid-crystalline materials, molecular dynamics (MD) simulations are a good approach. They can easily be compared to experimental results and additionally provide detailed structural information which is not easily experimentally determinable. We study the Gay-Berne model of discotic liquid crystals in bulk and in a cylindrical pore nanoconfinement. To study the phase diagram we use various order parameters, some of them specifically designed for cylindrical confinement. We also study the structure of the fluid via the radial distribution function and the dynamics via the van Hove distribution function. The structure of the thesis is the following.

In section 1.3 we describe the the main theoretical ideas at the basis of this work. Section 1.4 describes the model potentials employed and the numerical details. In section 1.5.1 we specify the used order parameters and the radial distribution function. The specific order parameters for the confinement are described in section 1.5.2. In section 1.5.3 the van Hove correlation function for dynamical study is described.

We explain the details of the implementation and the simulation in chapter 2.

Chapter 3 is dedicated to the analysis of the results. We start with the bulk, subsequently investigating the two cases of nanoconfinement, the different radii separately. The chapter ends with a summary of the main features of the phase diagrams of the confined systems.

In chapter 4 we discuss aspects of the methods used in the preceding chapter and give some outlooks.

1.2 Basics of Liquid Crystals

Liquid crystals are very interesting materials. They possess properties of crystals and still flow like liquids. Those properties manifest themselves in so called *mesophases*, that liquid crystals show between the ordinary crystal and liquid phase. Substances showing this behaviour are also often called *mesogens*. For the liquid crystals of interest in this thesis, these phases occur as a function of temperature. Therefore they are called *thermotropic* liquid crystals.

Historically, liquid crystals were first observed by Reinitzer in 1888 [6]. He described the appearance of colours in melts of cholesterol acetate and benzoate and particularly the double melting behaviour of those.

On heating these substances in crystalline form up to the *melting point*, they first melt into a cloudy liquid, which is one of the aforementioned mesophases. It possess anisotropic properties that make it distinct from an ordinary liquid. For example, it exhibits an orientation dependent polarisation of the incident light. One would not relate this behaviour, i.e., the coloured phenomenon, to a liquid but rather to a crystal. Upon further heating, the cloudy liquids subsequently clarify at a certain temperature, the *clearing point*. When this transition occurs, the anisotropic properties vanish and the mesogen behaves like an ordinary liquid.

Besides thermotropics, there are lyotropic liquid crystals, that show phase transitions as a function of their concentration in a solvent. Generally, liquid crystals are a large group of materials, in which the occurring mesophases arise mostly from the shape, but also from other properties of the constituent molecules. In contrast to ordinary liquids, where the constituent molecules have an isotropic shape, mesogens are anisotropic in shape and properties.

The most common shapes among liquid crystals are long rod-like molecules called *calamitics*, or disk-shaped molecules called *discotics*. The discotics are the mesogens of interest here. As a function of temperature they exhibit the phases listed in Table 1.1 [7]:

	Phase	Abbreviation
temperature ↓	crystal	Cr
	<i>hexagonal columnar</i>	Col _h
	<i>rectangular columnar</i>	Col _r
	<i>discotic nematic</i>	N
	isotropic	I

Table 1.1: Some discotic liquid crystal phases

To understand the properties and the formation of the mesophases, it is necessary to know the properties of the mesogens, that arise from their chemical structure.

1.2.1 Chemical Structure

Mesogens have very rigid cores, that provide their shape. Such a core consists of aromatic rings. Figure 1.1 shows two examples of mesogens containing aromatic rings, notice that the cores are flat. The dashed lines represent the delocalised electrons in the π -orbitals, that form from the overlap of the p-orbitals of the carbon atoms. This state is energetically favourable, and provides the flat regular hexagonal shape. Like mentioned before, discotics are considered disk-like, which may look more reasonable for larger molecules.

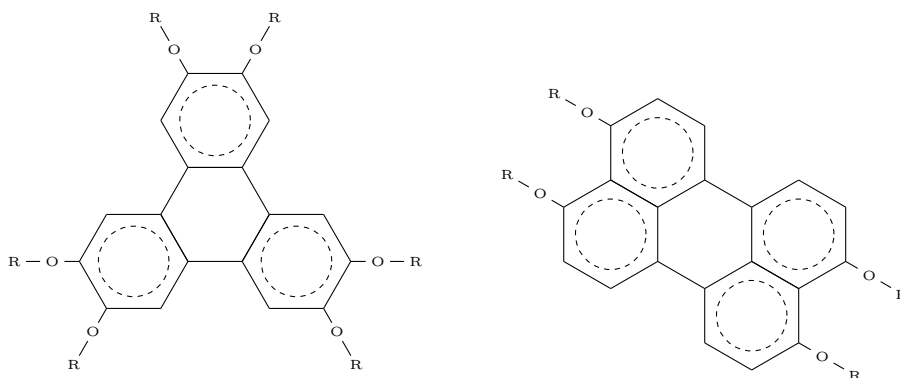


Figure 1.1: Structural formulas of a triphenylene derivate (left) and a perylene derivate (right).

In Fig 1.1, the letter R denotes aliphatic side chains, which may vary. In contrast to the core, the side chains are quite flexible. Early investigations on discotics began with benzene, the smallest aromatic core. Nowadays the trend goes to even larger cores than the aforementioned. This evolution is linked to the ability of synthesising new molecules. The stability and appearance of the different liquid crystal phases appears to increase with the size of the core, up to a certain limit of course. If stacked on top of each other, electrons are able to hop from one to the next molecule.

This becomes more efficient with a larger core size. Theoretically, the electron hopping rate can be described according to the Marcus theory, i.e. as a function of the orbital overlap of the π -orbitals and the internal energy difference of a charged and an uncharged molecules.

For the use as nanowires, the columnar phases of discotic liquid crystals are required, because the columns are electrically conductive (cf. Sect. 1.2.2). Hence, a discotic liquid crystal is conductive in one dimension. To establish applicable nanowires, the columnar discotic mesophases need to form at ambient temperature. One way of tuning the temperature dependence of the transition temperatures is changing the length of the side chains. Nevertheless creating mesogens that exhibit liquid crystalline phases at ambient temperature is difficult; aliphatic side chains quite different from linear are required.

The molecules have different electric and magnetic susceptibilities in the direction normal to the core's plane compared to directions lying in the core's plane. Because the molecules are not chiral, there is no up or down along this normal axis. Thus for notation a unit vector $\hat{\mathbf{e}}$, named the molecular director, is used. Because of the head-tail symmetry $\hat{\mathbf{e}}$ is equivalent to $-\hat{\mathbf{e}}$. [8, 7]

1.2.2 Discotic Liquid Crystal Phases

When classifying phases and discussing their properties, symmetries play an important role [7]. The molecules are normally regarded as axisymmetric, which means they have a $D_{\infty h}$ symmetry, in Schönflies notation. This means that the molecules are symmetric upon proper rotations of an arbitrary angle about a distinct axis, here, the axis through the middle of the disk and normal to its plane. The same applies for improper rotations, which is a rotation followed by a reflection in a plane perpendicular to the axis of rotation, which here is the same as before. We now describe the most important mesophases for discotics, starting from the high temperature end.

Isotropic:

Like the name of the phase already says, it posses complete spatial symmetry, that means there is no special orientation. Physical properties are the same in all directions, because the molecules all are oriented isotropically. The large kinetic energy prevents an alignment of the molecules. So, on average, their anisotropic properties vanish. Nevertheless, there are short-range correlations as always in ordinary liquids. At close distances, there are separations, that pairs of particles favour. Compared to that, in an ideal gas there is no such correlation, while in a crystal, there is long-range correlation, i.e. a lattice. This phase is the clear liquid mentioned before.



Figure 1.2: Isotropic phase of a Gay-Berne fluid (see Sect. 1.4.3.3). Images are parts of different bulk simulations, they were visualised using QMGA[9].

Nematic:

Upon cooling, the transition into the nematic phase involves a spontaneous symmetry breaking. Now there is a director, along which the molecules orient on average, as one can see in Fig. 1.3. The colouring of the molecules there visualises the deviation from the mean particle orientation,

where blue means that the particle has the average orientation.

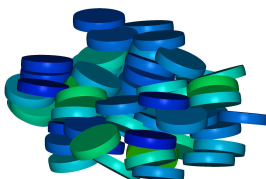


Figure 1.3: Nematic mesophase of a Gay-Berne fluid.

Like in the isotropic phase, there are short-range correlations, and still the nematic phase is completely fluid. As a consequence of the orientational order of the molecules, the whole material now exhibits the anisotropic physical properties of the constituent molecules and is thus optically uniaxial, because of the anisotropy of the electric susceptibility. The nematic phase therefore possess a $D_{\infty h}$ symmetry. Every direction perpendicular to the director is consequently equivalent.

To understand the formation of this phase, consider the interaction between a pair of neutral atoms through isotropic dispersion forces. The corresponding material would reveal isotropic gaseous and liquid states. The interaction potential has a well at a certain distance which is therefore favoured by the atoms, if the temperature is low enough. The interaction between large molecules like liquid crystals can therefore be seen as a superposition of many of the aforementioned interactions at representative fixed sites in the space occupied by the molecule. When now disk-like molecules are stacked on top of each other, probably many sites in one molecule are at the favoured distance to one side of the other molecule and at close distance. The stacked configuration therefore minimises the overall potential energy of all individual sites. Similar arguments apply to rod-like molecules. This is why disk-shaped molecules tend to stack on top of each another, while rod-like ones favour aligning side by side.

But as the temperature is still very high in the nematic phase, just an orientational correlation is induced, mostly by the shape anisotropy. Simulations showed that even without a force anisotropy, hard sphere ellipsoidal particles exhibit a nematic phase [7, 10].

Columnar:

Upon further cooling, discotic mesogens stack face-to-face and form column. Those columns extend over large distances in columnar phases and then arrange in a two-dimensional lattice.



Figure 1.4: Hexagonal columnar mesophase of a Gay-Berne fluid.

Figure 1.4 shows a hexagonal columnar phase in the bulk. Rectangular arrangement is also possible. Those two lattices reduce the symmetry form $D_{\infty h}$ to D_{2h} and D_{6h} , respectively. Nanoconfine-

ment, though, can also induce other arrangements among the columns. The discotics are still fluid along the columns axis, so in this phase it is a liquid in one dimension and a solid in the two others.

The columnar mesophases are of large interest, because electrons are mobile along the column axis. This has found applications in the formation of nanowires in organic electronics. The big advantage is that the system heals defects autonomously and it is self-organising, which makes them easy to produce [11, 4].

When molecules are stacked on top of each other, electrons from π -orbitals are free to hop to the next molecule. So obviously for application in nanowires, perfect columns over long distances are necessary [7, 10, 12]. The stability could be increased by a cylindrical nanoconfinement, which has $D_{\infty h}$ symmetry, because a medium subject to an external constraint changes its symmetry in order to keep only those symmetry elements shared with the constraint. This is called the ‘‘Curie Principle’’.

Crystal:

The model used in this work exhibits an orthorhombic body-centred crystal phase.

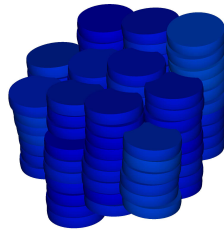


Figure 1.5: Crystal phase of a Gay-Berne fluid.

Following course: In the following subsection a brief motivation of molecular dynamic simulations will be given. After introducing the tensor and scalar order parameter, that are necessary to determine the phase diagram, the Maier-Saupe theory will be presented. It deals with a mean field approach that uses the scalar order parameter, and exhibits an isotropic to nematic phase transition which can be solved analytically.

1.3 Statistical Mechanics

When classical molecular dynamic simulations are performed, Newton’s equations of motions are solved by numeric algorithms. The computer is used to solve a rather large system of ordinary differential equations. The forces are calculated based on the potentials that model the molecular interaction. An observable macroscopic physical property \mathcal{A}_{obs} is calculated through a time average over the N_t observations:

$$\mathcal{A}_{obs} = \langle \mathcal{A} \rangle_{\text{time}} = \frac{1}{N_t} \sum_{t=0}^{N_t} \mathcal{A}(\mathbf{\Gamma}(t, \mathbf{\Gamma}_0)),$$

where $\mathbf{\Gamma}(t, \mathbf{\Gamma}_0)$ is the $6N$ dimensional vector, i.e. positions and momenta, describing the state of the system. Formally, the value of the observable depends on the initial condition, the system then evolves according to the equations of motion. This is also how temperature and pressure are calculated.

However, this is not the approach to thermodynamic quantities made in statistical mechanics. In thermodynamics, the state of a system is typically described by a small set of macroscopic parameters like number of particles N , pressure P and temperature T or one containing a conjugate property. Other thermodynamic properties can then be obtained with the knowledge of the equations of state.

If one assumes that, like above, it is possible to write the current value of a macroscopic property \mathcal{A} as a function of the microscopic state $\mathbf{\Gamma}(t, \mathbf{\Gamma}_0)$, the above procedure is not yet justified. An experimentally measured value, realistically, is also a time average over the measurement interval Δt :

$$\langle \mathcal{A} \rangle_{\text{time}} = \lim_{\Delta t \rightarrow \infty} \frac{1}{\Delta t} \int_0^{\Delta t} \mathcal{A}(\mathbf{\Gamma}(t, \mathbf{\Gamma}_0)) dt. \quad (1.1)$$

In statistical mechanics the time average is replaced by an ensemble average, because of the complex time evolution of $\mathcal{A}(\mathbf{\Gamma}(t, \mathbf{\Gamma}_0))$ and the explicit dependence of $\mathbf{\Gamma}(t, \mathbf{\Gamma}_0)$ on the initial condition. An ensemble means a vast collection of possible states $\mathbf{\Gamma}$ of the system, distributed according to a probability density $\rho(\mathbf{\Gamma}(t))$. This probability density is determined by the macroscopic state of the system, determined by e.g. number of particles, pressure and temperature. In this treatment, a macroscopic property is then calculated via

$$\langle \mathcal{A} \rangle_{\text{ens}} = \int \rho(\mathbf{\Gamma}) \mathcal{A}(\mathbf{\Gamma}) d\mathbf{\Gamma}. \quad (1.2)$$

In this approach, there is neither knowledge of the actual state of the system nor of its time evolution. We are looking for the connection of our macroscopic properties to the microscopic properties of the system. Using a finite time average, it is possible for the system not to move through the entire phase space, depending on the initial condition, leading to false results. The reasons can be nearly periodic trajectories or phase space volumes only connected through bottlenecks. So, the question arises: under which condition can we replace the ensemble average with a finite time average using an arbitrary but definite starting condition, since we want to use the procedure of molecular dynamic simulation. Generally the same issue arises if one wants to use e.g. a thermometer to determine the temperature of a system [13].

1.3.1 Ergodic Hypothesis

There is a time $t_0 < \infty$, for which a system, independent from the initial condition, explores each possible point in phase space [14].

If so, one can freely send the observation time Δt to infinity, because there won't be any additional information after t_0 . One can then for $\tau > t_0$ write

$$\begin{aligned} \langle \mathcal{A} \rangle &= \lim_{\Delta t \rightarrow \infty} \frac{1}{\Delta t} \int_0^{\Delta t} \mathcal{A}(\mathbf{\Gamma}(t, \mathbf{\Gamma}_0)) dt = \lim_{\Delta t \rightarrow \infty} \left[\frac{1}{\Delta t} \int_0^{\tau} \mathcal{A}(\mathbf{\Gamma}(t, \mathbf{\Gamma}_0)) dt + \frac{1}{\Delta t} \int_{\tau}^{\Delta t} \mathcal{A}(\mathbf{\Gamma}(t, \mathbf{\Gamma}_0)) dt \right] \\ &= \lim_{\Delta t \rightarrow \infty} \frac{1}{\Delta t} \int_0^{\tau} \mathcal{A}(\mathbf{\Gamma}(t, \mathbf{\Gamma}_0)) dt + \lim_{T \rightarrow \infty} \frac{1}{\Delta t} \int_0^{\Delta t - \tau} \mathcal{A}(\mathbf{\Gamma}(t, \mathbf{\Gamma}'_0)) dt. \\ &= \lim_{\Delta t \rightarrow \infty} \frac{1}{\Delta t} \int_0^{\Delta t} \mathcal{A}(\mathbf{\Gamma}(t, \mathbf{\Gamma}'_0)) dt, \end{aligned}$$

where $\mathbf{\Gamma}'_0 \equiv \mathbf{\Gamma}(\tau, \mathbf{\Gamma}_0)$. So, if the above assumption holds, the time average for $\Delta t \rightarrow \infty$ is independent from the initial condition. In general, one has to be cautious, because ergodicity does

not apply for many systems. For instance, in a ferromagnet below the Curie temperature, there should be no net magnetisation if the system would explore all states of magnetisation in phase space. So this system is not ergodic.

In relation to the goal of connecting the time average with the ensemble average one can rewrite the observable with the δ distribution.

$$\mathcal{A}(\gamma(t)) = \int \delta(\mathbf{\Gamma} - \gamma(t)) \mathcal{A}(\mathbf{\Gamma}) d\mathbf{\Gamma}.$$

Plugging this in the above equation (1.1), the time integral and the integral over phase space can be exchanged:

$$\langle \mathcal{A} \rangle_{\text{time}} = \int \mathcal{A}(\mathbf{\Gamma}) \lim_{\Delta t \rightarrow \infty} \frac{1}{\Delta t} \int_0^{\Delta t} \delta(\mathbf{\Gamma} - \gamma(t)) dt d\mathbf{\Gamma}.$$

With the definition of the probability density to find a system in the vicinity of $\mathbf{\Gamma}$

$$\rho(\gamma) \equiv \lim_{\Delta t \rightarrow \infty} \frac{1}{\Delta t} \int_0^{\Delta t} \delta(\gamma - \mathbf{\Gamma}(t)) dt,$$

we obtain the desired connection to (1.2)

$$\langle \mathcal{A} \rangle_{\text{time}} = \langle \mathcal{A} \rangle_{\text{ens}} = \int \rho(\mathbf{\Gamma}) \mathcal{A}(\mathbf{\Gamma}) d\mathbf{\Gamma}.$$

1.4 Computational Methods

The previous two parts on statistical mechanics justify choosing an arbitrary initial configuration of the system of interest, and simulating its dynamics over a sufficient time span. The molecular motions are described classically, since for large systems, quantum calculations must agree with classical calculations, according to the correspondence principle of quantum mechanics, and since the thermal de Broglie wavelengths are much smaller than molecular distances.

1.4.1 Equations of Motion

A physical system of N molecules is described by a set of coupled ordinary differential equations. For each molecule i with the mass m Newton's second law says that

$$m\ddot{\mathbf{x}}_i = \mathbf{F}_i = -\nabla_{\mathbf{x}_i} V(\mathbf{x}_1, \dots, \mathbf{x}_N, \hat{\mathbf{e}}_1, \dots, \hat{\mathbf{e}}_N).$$

Here, $\hat{\mathbf{e}}_1, \dots, \hat{\mathbf{e}}_N$ stand for the molecule orientations, since the potentials are anisotropic for the liquid crystals. The scalar potential of the conservative force \mathbf{F}_i can also be written as the sum over all pairwise interaction potentials

$$m\ddot{\mathbf{x}}_i = -\nabla_{\mathbf{x}_i} \sum_{j \neq i} V(\mathbf{x}_{ij}, \hat{\mathbf{e}}_i, \hat{\mathbf{e}}_j),$$

with the intermolecular vector \mathbf{x}_{ij} . Here one can see the coupling of the differential equations given that the overall potential depends on all the molecular positions. There is then a system of $3N$ second-order differential equations to solve, in order to compute the trajectories of the molecular centres of mass.

1.4.2 Finite Difference Method of the Verlet Algorithm

The dynamics is given by an initial condition together with the the equations of motion, in general ordinary differential equations. This is a so-called initial value problem. There is a standard method for solving initial value problems, namely the finite difference method. The first approach is as follows. Given the initial condition of the system, i.e. the molecular positions, their orientation, and corresponding velocities, at a time t , we want to know the dynamic state of the system at a later time $t + \delta t$. There is a large number of differential equations to solve, which is not possible to accurately solve in a feasible amount of time. So we have to be content with a solution of sufficient accuracy. The whole dynamics can then be obtained by subsequently applying the method again on the state of the system at the later time. There are many algorithms falling in the class of finite difference methods.

For example, maybe the simplest one of the methods is the Euler method, which is based on a Taylor expansion of the trajectory $x(t)$. The underlying differential equation is $\dot{x} = f(x)$, where $f(x)$ does not depend explicitly on time. Neglecting quadratic and higher order terms in the Taylor expansion one obtains

$$x(t + \delta t) = x(t) + \dot{x}(t)\delta t + w \quad \text{or} \quad \int_t^{t+\delta t} f(x)dt \approx \dot{x}(t)\delta t.$$

For the Verlet algorithm, the Taylor expansion of $x(t \pm \delta t)$ with an error of order $\mathcal{O}(\delta t^4)$ are

$$x(t + \delta t) = x(t) + \dot{x}(t)\delta t + \frac{\ddot{x}(t)\delta t^2}{2} + \frac{\dddot{x}(t)\delta t^3}{6} + \mathcal{O}(\delta t^4) \quad (1.3)$$

and

$$x(t - \delta t) = x(t) - \dot{x}(t)\delta t + \frac{\ddot{x}(t)\delta t^2}{2} - \frac{\dddot{x}(t)\delta t^3}{6} + \mathcal{O}(\delta t^4). \quad (1.4)$$

The summation of (1.3) and (1.4) then yields

$$x(t + \delta t) = 2x(t) - x(t - \delta t) + \ddot{x}(t)\delta t^2 + \mathcal{O}(\delta t^4). \quad (1.5)$$

As one can see, the velocities are not needed for the computation of the trajectories, but they are very much necessary for computing e.g. the kinetic energy. The can be calculated with the stored values of $x(t \pm \delta t)$ by the formula

$$\dot{x}(t) = \frac{x(t + \delta t) - x(t - \delta t)}{2\delta t}.$$

It is also obtained by adding the Taylor expansion (1.3) and (1.4), this time neglecting terms of order $\mathcal{O}(\delta t^2)$, simply because $x(t \pm \delta t)$ are the only stored values.

Importantly, the basic Verlet algorithm is time reversible, as both $x(t + \delta t)$ and $x(t - \delta t)$ contribute in the same way.

Unfortunately, while the positions are accurate up to $\mathcal{O}(\delta t^4)$ errors, the velocities have an error of order $\mathcal{O}(\delta t^2)$. A more accurate estimate of $\dot{x}(t)$ could be made if more variables would be stored. Because of (1.5), all necessary computation for the new position is been performed in one single step, which requires a bigger adjustment of the algorithm. This leads us to the velocity Verlet algorithm [15], which stores positions, velocities and accelerations all at the same time. It takes the form

$$\begin{aligned} x(t + \delta t) &= x(t) - v(t)\delta t + \frac{a(t)\delta t^2}{2} \\ v(t + \delta t) &= v(t) + \delta t \frac{a(t) + a(t + \delta t)}{2}. \end{aligned}$$

Additionally, it also minimises round-off errors [13].

1.4.3 Intermolecular Potential Model

In order to perform MD simulations, one needs models for the intermolecular interaction. Since the force fields completely arise from electromagnetic forces, which are conservative, the resulting forces are also conservative. So for the models of interaction, this means finding a suitable potential based on which forces and torques can then be derived. To solve the actual interaction between molecules as large as mesogens is extremely complex. Despite that fact, mesophases and realistic dynamics can be observed by assuming surprisingly simple interaction models. One distinguishes between site-site and single-site potentials. Site here means a point in space for which the potential energy is calculated. In the first category, there is a number of sites representing the molecule. In the latter potentials depend on a single position and an orientation [13, p. 7-23].

1.4.3.1 Site-Site Potentials

A very accurate classical model would probably be a superposition of many Lennard-Jones interactions. Each molecule is then modelled by a number of N sites, arranged in a fixed, representative way, between which the Lennard-Jones potential is then calculated. Unfortunately, mesogens are typically quite large molecules. The complexity of calculating all pairwise interactions is of order $O(N^2)$. Therefore potentials of these type are usually too expensive for the use in MD simulations. A workaround is the use of asymmetric single-site potentials [13, p. 7-23].

1.4.3.2 Overlap Potential

The first single site potential, that is mathematically controllable, is the overlap potential of Berne and Pechukas [10]. Its simple form is obtained by calculating the overlap integrals of two identical, three dimensional, elliptical Gaussians for arbitrary relative orientation:

$$G(\mathbf{r}) = \exp[-(x^2 + y^2)/\sigma_{ee}^2 - z^2/\sigma_{ff}^2].$$

This yields

$$S(\hat{\mathbf{e}}_1, \hat{\mathbf{e}}_2, \mathbf{r}) = \underbrace{\{\epsilon_0[1 - \chi^2(\hat{\mathbf{e}}_1 \cdot \hat{\mathbf{e}}_2)^2]^{-1/2}\}}_{\epsilon(\hat{\mathbf{e}}_1, \hat{\mathbf{e}}_2)} \cdot \exp[-r^2/\sigma^2(\hat{\mathbf{e}}_1, \hat{\mathbf{e}}_2, \hat{\mathbf{r}})], \quad (1.6)$$

where \mathbf{r} is the vector between the centres of the two Gaussians, $r \equiv |\mathbf{r}|$, $\hat{\mathbf{r}} = \frac{\mathbf{r}}{r}$ and $\hat{\mathbf{e}}_1, \hat{\mathbf{e}}_2$ are unit vectors pointing in the direction of the axis of symmetry of each Gaussian, respectively. The coefficient $\epsilon(\hat{\mathbf{e}}_1, \hat{\mathbf{e}}_2)$ in Eq. (1.6) is called strength parameter, and

$$\sigma(\hat{\mathbf{e}}_1, \hat{\mathbf{e}}_2, \hat{\mathbf{r}}) = \sigma_0 \left(1 - \frac{1}{2}\chi \left[\frac{(\hat{\mathbf{r}} \cdot \hat{\mathbf{e}}_1 + \hat{\mathbf{r}} \cdot \hat{\mathbf{e}}_2)^2}{1 + \chi(\hat{\mathbf{e}}_1 \cdot \hat{\mathbf{e}}_2)} + \frac{(\hat{\mathbf{r}} \cdot \hat{\mathbf{e}}_1 - \hat{\mathbf{r}} \cdot \hat{\mathbf{e}}_2)^2}{1 - \chi(\hat{\mathbf{e}}_1 \cdot \hat{\mathbf{e}}_2)} \right] \right)^{-1/2}, \quad (1.7)$$

is called the range parameter. The shape anisotropy parameter χ is defined as

$$\chi \equiv (\sigma_{ff}^2 - \sigma_{ee}^2)/(\sigma_{ff}^2 + \sigma_{ee}^2),$$

where ϵ_0 and σ_0 are simply constants, and σ_{ff}, σ_{ee} are the face-face and end-end distances, respectively, that is the short and long molecular axis. The overlap potential is then assembled out of the range and strength parameters, obtained via the overlap integral, and the Lennard-Jones potential functional form:

$$V(\hat{\mathbf{e}}_1, \hat{\mathbf{e}}_2, \mathbf{r}) = 4\epsilon(\hat{\mathbf{e}}_1, \hat{\mathbf{e}}_2) \left\{ \left[\frac{\sigma(\hat{\mathbf{e}}_1, \hat{\mathbf{e}}_2, \hat{\mathbf{r}})}{r} \right]^{12} - \left[\frac{\sigma(\hat{\mathbf{e}}_1, \hat{\mathbf{e}}_2, \hat{\mathbf{r}})}{r} \right]^6 \right\}.$$

For arbitrary relative orientations $\hat{\mathbf{e}}_1, \hat{\mathbf{e}}_2$ the potential always keeps the basic look of the Lennard-Jones potential.

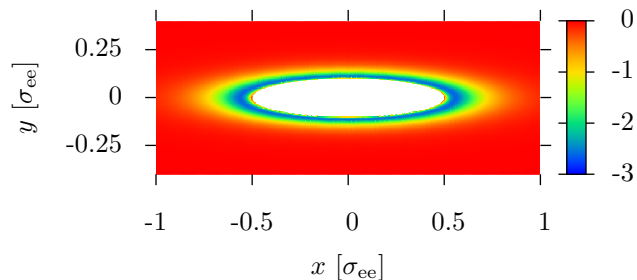


Figure 1.6: Heatmap of the potential energy for the Berne-Pechukas model for two parallel discotic particles pointing into the y -direction with $\sigma_{\text{ff}}/\sigma_{\text{ee}} = \frac{1}{5}$.

The decisive benefit of this potential is that forces and torques can easily be obtained by differentiation. This makes it suitable for the use in computer simulations because the dynamics can then be computed completely analytically.

Let's take a look at the properties of $V(\hat{\mathbf{e}}_1, \hat{\mathbf{e}}_2, \mathbf{r})$. Figure (1.6) shows the heat map of the potential energy between a particle at the origin and a second particle at different positions, both particles with the orientation $\hat{\mathbf{e}}_1 = \hat{\mathbf{e}}_2 = \hat{\mathbf{y}}$. At $\sigma(\hat{\mathbf{e}}_1, \hat{\mathbf{e}}_2, \hat{\mathbf{r}}) = |\mathbf{r}|$ the repulsive and attractive part of the potential cancel each other out, and at a closer distance the potential is strongly repulsive, which can be seen in the inner white region of the plot, which is positive and thus repulsive. Therefore, this distance can be treated as the distance where the ellipsoids touch each other.

When keeping in mind that the overlap potential is designed to mimic various multiple site potentials, one will easily notice unrealistic behaviour in the nature of the potential. One can see that on the one hand, the side-side alignment is not preferred as requested, as the wells-depths are the same in all relative position because $\epsilon(\hat{\mathbf{e}}_1, \hat{\mathbf{e}}_2)$ does not depend on $\hat{\mathbf{r}}$. On the other hand, the width of the wells is wider for the side-side alignment, which is unrealistic when thinking of the site-site model potential.

1.4.3.3 Gay-Berne Model

Based on the overlap potential of Berne and Pechukas, Gay and Berne introduced a improved single-site potential [10]. Like the overlap potential, it is based on the Lennard-Jones potential. But instead of stretching the potential with the range parameter $\sigma(\hat{\mathbf{e}}_1, \hat{\mathbf{e}}_2, \hat{\mathbf{r}})$ (see Eq. (1.7)), it is displaced by the same amount, i. e.

$$\frac{\sigma(\hat{\mathbf{e}}_1, \hat{\mathbf{e}}_2, \hat{\mathbf{r}})}{r} \rightarrow \frac{1}{r - \sigma(\hat{\mathbf{e}}_1, \hat{\mathbf{e}}_2, \hat{\mathbf{r}}) + 1}, \quad (1.8)$$

so that the well-width is independent of the relative position of the molecules. The potential then looks like

$$V(\hat{\mathbf{e}}_1, \hat{\mathbf{e}}_2, \mathbf{r}) = 4\epsilon(\hat{\mathbf{e}}_1, \hat{\mathbf{e}}_2, \hat{\mathbf{r}}) \left\{ \left[\frac{1}{r - \sigma(\hat{\mathbf{e}}_1, \hat{\mathbf{e}}_2, \hat{\mathbf{r}}) + 1} \right]^{12} - \left[\frac{1}{r - \sigma(\hat{\mathbf{e}}_1, \hat{\mathbf{e}}_2, \hat{\mathbf{r}}) + 1} \right]^6 \right\}, \quad (1.9)$$

where $\epsilon(\hat{\mathbf{e}}_1, \hat{\mathbf{e}}_2, \hat{\mathbf{r}})$ is a new parameter

$$\epsilon(\hat{\mathbf{e}}_1, \hat{\mathbf{e}}_2, \hat{\mathbf{r}}) = \epsilon_1^V(\hat{\mathbf{e}}_1, \hat{\mathbf{e}}_2) \cdot \epsilon_2^H(\hat{\mathbf{e}}_1, \hat{\mathbf{e}}_2, \hat{\mathbf{r}}) \quad (1.10)$$

with $\epsilon_1(\hat{\mathbf{e}}_1, \hat{\mathbf{e}}_2)$ as in Eq. (1.6), that is, the Berne-Pechukas strength parameter, and $\epsilon_2(\hat{\mathbf{e}}_1, \hat{\mathbf{e}}_2, \hat{\mathbf{r}})$ defined as

$$\epsilon_2(\hat{\mathbf{e}}_1, \hat{\mathbf{e}}_2, \hat{\mathbf{r}}) = 1 - \frac{1}{2}\chi' \left[\frac{(\hat{\mathbf{r}} \cdot \hat{\mathbf{e}}_1 + \hat{\mathbf{r}} \cdot \hat{\mathbf{e}}_2)^2}{1 + \chi'(\hat{\mathbf{e}}_1 \cdot \hat{\mathbf{e}}_2)} + \frac{(\hat{\mathbf{r}} \cdot \hat{\mathbf{e}}_1 - \hat{\mathbf{r}} \cdot \hat{\mathbf{e}}_2)^2}{1 - \chi'(\hat{\mathbf{e}}_1 \cdot \hat{\mathbf{e}}_2)} \right].$$

The role of $\epsilon_2(\hat{\mathbf{e}}_1, \hat{\mathbf{e}}_2, \hat{\mathbf{r}})$ is to make the wells deeper in the face-to-face configuration, which makes V a more realistic interaction. For discotics the choices $\nu = 2$ and $\mu = 1$ are suitable [12]. If ϵ_{ee} is the value of the strength parameter in the end-to-end configuration and ϵ_{ff} for the face-to-face configuration then

$$\chi' \equiv (\epsilon_{ee}^\mu - \epsilon_{ff}^\mu) / (\epsilon_{ee}^\mu + \epsilon_{ff}^\mu).$$

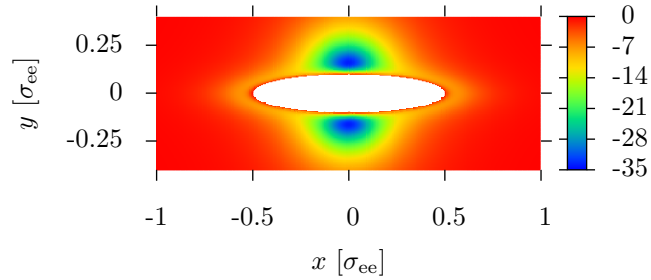


Figure 1.7: Heatmap of the potential energy for the Gay-Berne potential for two parallel discotic particles pointing into the y -direction with $\sigma_{ff}/\sigma_{ee} = \frac{1}{5}$ for comparability and χ' take according to [12].

As one can readily see in Fig. 1.7, the interaction prefers the face-to-face configuration. Additionally, the potential does not have the unwanted stretching of the well width in the elongated direction of the shape, which is $\hat{\mathbf{x}}$. This is the improvement on the overlap potential which is achieved with the modification in Eq. (1.8).

So, compared to the overlap potential there are two major characteristics of the Gay-Berne potential:

- (i) like the overlap potential, the Gay-Berne potential features a steric anisotropy, which is, however, improved compared to the overlap potential
- (ii) there is now a controllable force anisotropy, that makes the potential much more realistic.

1.4.3.4 Improvement

In 1996 Bates and Luckhurst [16] introduced a modification on the Gay-Berne Potential for discotics, which they called GBDII. It fixes the issue that if two model-particles approach each other in the face-face configuration, the potential does not become infinite at zero distance but at $\sigma_{ee} - \sigma_{ff}$, which is negative. This came from the expansion of the application of the GB model introduced for modelling calamitic liquid crystals to modelling discotic LCs. The issue can be corrected introducing

$$V(\hat{\mathbf{e}}_1, \hat{\mathbf{e}}_2, \mathbf{r}) = 4\epsilon(\hat{\mathbf{e}}_1, \hat{\mathbf{e}}_2, \hat{\mathbf{r}}) \left\{ \left[\frac{\sigma_{ff}}{r - \sigma(\hat{\mathbf{e}}_1, \hat{\mathbf{e}}_2, \hat{\mathbf{r}}) + \sigma_{ff}} \right]^{12} - \left[\frac{\sigma_{ff}}{r - \sigma(\hat{\mathbf{e}}_1, \hat{\mathbf{e}}_2, \hat{\mathbf{r}}) + \sigma_{ff}} \right]^6 \right\}. \quad (1.11)$$

We will use this model for our work. The forces and torques between molecules follow from

$$\mathbf{F} = -\nabla_{\mathbf{r}} V \quad \text{and} \quad \boldsymbol{\tau} = -\nabla_{\mathbf{e}} V.$$

1.4.4 Reduced Units

For the present system consisting only of one type of particle, it is reasonable to use reduced units, as they bring a lot of simplifications. Therefore the particles mass is set to one $m_i = 1$. Also the fluid-fluid interaction energy ϵ_0 and the long molecular diameter σ_{ee} are set to one. This saves computation time, because the values do not appear in the computer program. Another great benefit is that both pairs i.e. the momentum \mathbf{p} and the velocity \mathbf{v} , and the force \mathbf{F} and acceleration \mathbf{a} become identical in the numerical program. Also the results from the simulations can be scaled for different actual systems. From these definitions the units of other quantities also follow (see Table 1.2) [13].

quantity	dependency
length	$\sigma_{ee} = 1$
energy	$\epsilon_0 = 1$
temperature	$T^* = k_B T / \epsilon_0$
pressure	$P^* = P \sigma_{ee}^3 / \epsilon_0$
time	$t^* = t \sqrt{\epsilon_0 / m \sigma_{ee}^2}$
force	$\mathbf{F}^* = \mathbf{F} \sigma_{ee} / \epsilon_0$
torque	$\boldsymbol{\tau}^* = \boldsymbol{\tau} / \epsilon_0$
diffusion coefficient	$D^* = D \sigma_{ee} / t^*$

Table 1.2: Reduced units of some quantities.

1.4.5 Fluid-Wall Interaction

To achieve the effect of the ‘‘CURIE Principle’’, stabilising the columnar phase by imposing a similar symmetry, cylindrical nanopores are necessary. Those pores can be found in membranes of porous etched silica (pSiO₂) or alumina (pAl₂O₃). The channel radii can be controlled in the preparation process. Experiments have been performed with pores with radii in the range of 5 to 25 nm.

The fluid-wall (fw) interaction additionally exhibits an orientation dependence, and typically two different anchoring cases are investigated. The preferred orientation of a LC particle in the vicinity of the wall arises from the hydrophilic nature of the surfaces. In this case the *homeotropic* i.e. face-on (subscript \parallel) anchoring of discotic liquid crystals occurs.

For the the purpose of stabilising the the columnar phase, aiming at applications as nanowires, a different anchoring is desired. Through silanisation, the surfaces can be made more hydrophobic. This way, the aliphatic side chains of the discotic liquid crystals molecules are attracted to the wall. This so called *homeogeneous* i.e. edge-on (subscript \perp) anchoring does not favour a specific direction, the minimum orientational energy occurs when the molecular orientation vector is perpendicular to the surface normal [17].

The model potential is obtained by integrating a 12-6 Lennard Jones (LJ) interaction between a spherical particle and a semi-infinite wall composed of spherical particles arranged on a (111) plane of an fcc lattice [18]. The attractive part of the resulting standard 9-3 LJ model potential is additionally modulated by an orientation dependent prefactor $g_{orient} \in [0 : 1]$, called anchoring function. The model potential reads

$$V_{fw}(\hat{\mathbf{e}}, \mathbf{r}) = \epsilon_{fw} \left[\frac{2}{15} \left(\frac{\sigma_o}{d_w} \right)^9 - \left(\frac{\sigma_o}{d_w} \right)^3 g_{orient}(\hat{\mathbf{u}}(\mathbf{r}), \hat{\mathbf{e}}) \right],$$

where d_w is the minimum distance to the wall, $\hat{\mathbf{e}}$ the molecular orientation vector and $\hat{\mathbf{u}}$ the surface normal. The interaction energy ϵ_{fw} must have different values for the edge-on anchoring and for the face-on anchoring. This is due to the fact that as a reason of the symmetry of the columnar phases and the spacial restrictions entropically favour the edge-on alignment [19]. To ensure comparison with the work of Busselez *et. al.* [18], $\sigma_o = \sigma_{ff}$ has been chosen.

Because the force is independent of z coordinate, which has been chosen as the pores axis in the simulations, \mathbf{r} becomes

$$\mathbf{r} = \begin{pmatrix} x \\ y \end{pmatrix}$$

The distance to the wall is

$$d_w = \frac{d}{2} - |\mathbf{r}|,$$

where d is the pore diameter. The local surface normal in the cylindrical confinement is the negative of the particles unit position vector

$$\hat{\mathbf{u}} = -\frac{\mathbf{r}}{|\mathbf{r}|} \quad \Rightarrow \quad (\hat{\mathbf{u}} \cdot \hat{\mathbf{e}})^2 = (\hat{\mathbf{r}} \cdot \hat{\mathbf{e}})^2,$$

so that the face-on anchoring function is

$$g_{orient \parallel} = (\hat{\mathbf{r}} \cdot \hat{\mathbf{e}})^2.$$

For the *homeogeneous* anchoring occurring at the silanised surfaces [20] the potential has its minimum when the molecules orientation vector is perpendicular to the surface normal. For this case, the anchoring function is

$$g_{orient \perp} = (1 - |\hat{\mathbf{r}} \cdot \hat{\mathbf{e}}|)^2 = (1 - \sqrt{(\hat{\mathbf{r}} \cdot \hat{\mathbf{e}})^2})^2$$

The fluid-wall forces and torques follow from

$$\mathbf{F} = -\nabla_{\mathbf{r}} V_{fw} \quad \text{and} \quad \boldsymbol{\tau} = -\nabla_{\mathbf{e}} V_{fw}$$

1.5 Order Parameters and Correlation Functions

1.5.1 Structural Properties

1.5.1.1 Scalar and Tensor Order Parameter

Orientalional correlation is fundamental for the macroscopic features of a liquid crystalline material, since they arise from the anisotropic molecular features. Hence, it is necessary to introduce order parameters, which provide a measure of the orientational alignment. A good way to measure and introduce this correlation is to use a material property that determines the response to an applied external field. The magnetic susceptibility is most convenient for this task, because there are no local field effects contributing to an effective field, since the magnetic field does not induce dipoles.

As we will see later, this will lead us to a form also convenient for use in molecular dynamics simulations, which output distinct molecular orientations.

For the uniaxial molecules the magnetic susceptibility in the molecular axis system is of the form [21]

$$\chi_{ij}^m = \begin{pmatrix} \chi_{\perp}^m & 0 & 0 \\ 0 & \chi_{\perp}^m & 0 \\ 0 & 0 & \chi_{\parallel}^m \end{pmatrix}.$$

The molecular axis described by a unit vector $\hat{\mathbf{e}}$ in the laboratory coordinate system can be written as

$$\hat{\mathbf{e}} = \begin{pmatrix} \sin \theta \cos \varphi \\ \sin \theta \sin \varphi \\ \cos \theta \end{pmatrix} = \begin{pmatrix} 0 \\ \sin \theta \\ \cos \theta \end{pmatrix}.$$

Since there is no azimuthal correlation in an uniaxial material, φ is arbitrary and one can therefore without loss of generality choose $\varphi \stackrel{!}{=} \frac{\pi}{2}$. So in order to write the molecular property χ_{ij}^m in the laboratory frame, the tensor has to be rotated from the molecular coordinate system:

$$\chi_{ij}^m(\theta) = \mathbf{R}_x(\theta) \chi_{ij}^m \mathbf{R}_x^{-1}(\theta) = \mathbf{R}_x(\theta) \chi_{ij}^m \begin{pmatrix} 1 & 0 & 0 \\ 0 & \cos \theta & \sin \theta \\ 0 & -\sin \theta & \cos \theta \end{pmatrix},$$

which is

$$\chi_{ij}^m(\theta) = \chi_{\perp}^m \delta_{ij} + \underbrace{(\chi_{\parallel}^m - \chi_{\perp}^m) \begin{pmatrix} 0 & 0 & 0 \\ 0 & \sin^2 \theta & \cos \theta \sin \theta \\ 0 & \sin \theta \cos \theta & \cos^2 \theta \end{pmatrix}}_{= \hat{\mathbf{e}} \otimes \hat{\mathbf{e}}}.$$

When the bulk shows an orientational order, one expects the magnetic susceptibility to deviate in a specific direction. Hence, the aim is to determine the degree of order via the magnitude of the deviation of the magnetic susceptibility in a specific direction.

The separation of $\chi_{ij}^m(\theta)$ into its isotropic and anisotropic part yields:

$$\chi_{ij}^m(\theta) = \bar{\chi}^m \delta_{ij} + \Delta\chi^m \begin{pmatrix} -\frac{1}{3} & 0 & 0 \\ 0 & \sin^2 \theta - \frac{1}{3} & \cos \theta \sin \theta \\ 0 & \sin \theta \cos \theta & \cos^2 \theta - \frac{1}{3} \end{pmatrix} = \bar{\chi}^m \delta_{ij} + \Delta\chi^m \underbrace{\left(e_i e_j - \frac{1}{3} \delta_{ij} \right)}_{\text{anisotropic part}}$$

Whith $\bar{\chi}^m = \frac{1}{3}(2\chi_{\perp}^m + \chi_{\parallel}^m)$ the average susceptibility and $\Delta\chi^m = (\chi_{\parallel}^m - \chi_{\perp}^m)$ the anisotropy.

The bulk nematic order parameter is defined as the average over the entire system of the anisotropy $\Delta\chi^m$, $Q_{ij} \equiv \langle e_i e_j - \frac{1}{3} \delta_{ij} \rangle$. The scalar order parameter is defined as the largest eigenvalue of Q_{ij} , and the corresponding eigenvector is the nematic director. To simplify matters one can always choose the orientation of the laboratory frame so that the $\hat{\mathbf{z}}$ -axis coincides with the average orientation of the molecules, denoted by a unit vector $\hat{\mathbf{n}}$, the so-called director. The distribution function $f(\theta)$ will then look like in Fig. ???. One can already assume how the scalar order parameter

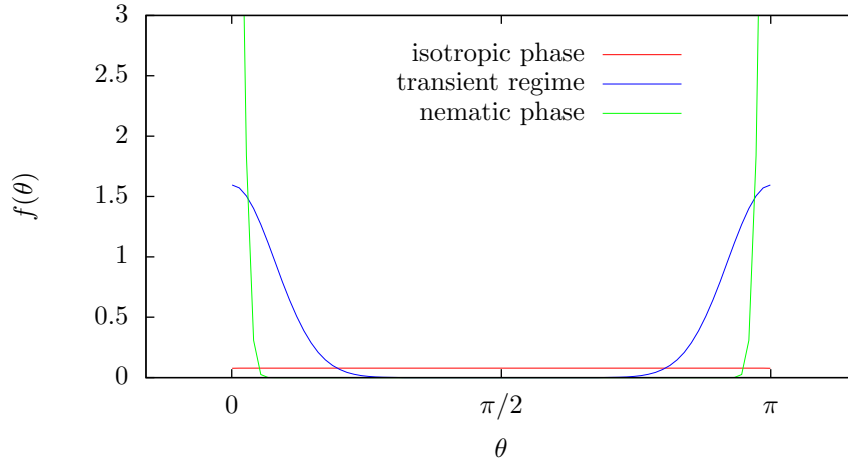


Figure 1.8: Qualitative distribution function $f(\theta)$ for different degrees of orientational order.

is going to look like, since Q_{ij} is diagonal due to the symmetry of the distribution function. The tensor order parameter can also be written as

$$Q_{ij} = \left\langle e_i e_j - \frac{1}{3} \delta_{ij} \right\rangle = S \left(n_i n_j - \frac{1}{3} \delta_{ij} \right) \quad (1.12)$$

Whith the scalar order parameter

$$S = \langle P_2(\hat{\mathbf{e}} \cdot \hat{\mathbf{n}}) \rangle, \quad P_2(x) = \frac{3}{2}x^2 - \frac{1}{2}. \quad (1.13)$$

$P_2(x)$ is the second Legendre polynomial, that corresponds to a quadrupole moment, so that one can say that our orientational ordered phase possess a quadrupole symmetry [7]. If we denote with θ the angle between each molecule and the nematic director, Eq. (1.13) becomes

$$S = \left\langle \frac{1}{2} (3 \cos^2(\theta) - 1) \right\rangle. \quad (1.14)$$

1.5.1.2 Maier-Saupe Theory

The most famous and succesfull theory for the behavior of the nematic order parameter at the phase transition temperature is the Maier-Saupe theory. It is a mean field theory in which the interaction energy is assumed to be an intermolecular dipole-dipole interaction, which means neglecting the anisotropic molecular shape. The interaction energy for a particle in the surrounding mean field is then

$$W_{int}(\theta_i) = -\frac{A}{V} S \left(\frac{3}{2} \cos^2(\theta_i) - \frac{1}{2} \right),$$

where A is a constant, dependent on the molecules. V is the volume, the inverse of the number density. S is the nematic order parameter of the surrounding medium and if $S > 0$ then θ_i is the angle between the molecules orientation vector an the nematic director, else an arbitrary reference axis. According to de Gennes formalism, this may be written as

$$G_1(\theta_i) = -\frac{1}{2} U(P, T) S \underbrace{\left(\frac{3}{2} \cos^2(\theta_i) - \frac{1}{2} \right)}_{\mu},$$

with the intermolecular interaction energy U . Note that $\langle \mu \rangle = S$, therefore the theory is also called S^2 interaction theory [22].

With the Gibbs free enthalpy of the isotropic phase $G_I(P, T)$, the expected value of the free enthalpy per molecule near T_{NI} is then

$$\begin{aligned} G(P, T) &= G_I(P, T) + k_B T \int f(\theta) \ln(f(\theta)) d\Omega + \langle G_1(P, T) \rangle [f] \\ &= G_I(P, T) + k_B T \int f(\theta) \ln(f(\theta)) d\Omega - \frac{U(P, T)}{2} \left(\int \mu f(\theta) d\Omega \right)^2. \end{aligned}$$

With $d\Omega = \sin(\theta) d\theta d\varphi$. This is then minimised through calculus of variations, with the constraint that the distribution function $f(\theta)$ is normalised. The appropriate functional then is

$$\mathcal{L}[f] = G_I(P, T) + k_B T \int f \ln(f) d\Omega - \frac{U(P, T)}{2} \left(\int \mu f d\Omega \right)^2 + \lambda \left(\int f d\Omega - 1 \right).$$

We consider an infinitesimal variation of f , $f + \epsilon \mu$, and minimise with respect to ϵ

$$\begin{aligned} \frac{d}{d\epsilon} \{ \mathcal{L}[f + \epsilon \eta] \} (\epsilon) &= k_B T \int \eta (\ln(f + \epsilon \eta) + 1) d\Omega \\ &\quad - \frac{U}{2} \left(2 \underbrace{\int \mu (f + \epsilon \eta) d\Omega}_{(\dots)|_{\epsilon=0} = S} \right) \int \eta \mu d\Omega + \lambda \int \eta d\Omega \end{aligned}$$

So with the condition that

$$\left[\frac{d}{d\epsilon} \mathcal{L}[f + \epsilon \eta] \right]_{\epsilon=0} \stackrel{!}{=} 0,$$

one gets

$$\begin{aligned} 0 &= \ln(f) + \frac{1}{k_B T} (k_B T - US \mu + \lambda) \\ \Rightarrow f(\theta) &= \exp \left(-\frac{1}{k_B T} \left[k_B T - \frac{US}{2} + \lambda \right] \right) \exp \left(\frac{3}{2} \frac{US}{k_B T} \cos^2(\theta) \right) \end{aligned}$$

via factoring out the variation η . The above then follows because a product is zero, when one of the factors is zero.

λ can now be determined by the normalisation constraint of f .

$$1 \stackrel{!}{=} \int f(\theta) d\Omega = \exp \left(-\frac{1}{k_B T} \left[k_B T - \frac{US}{2} + \lambda \right] \right) \int \exp \left(\frac{3}{2} \frac{US}{k_B T} \cos^2(\theta) \right) d\Omega$$

Thus, the distribution function is

$$f(\theta) = \frac{1}{Z} \exp(m \cos^2(\theta)),$$

with the partition function Z

$$Z = \int_0^\pi \exp(m \cos^2(\theta)) \sin(\theta) d\theta, \quad m = \frac{3US}{2k_B T}.$$

Yet, f is not independent of S . S can then be obtained by making an ansatz of self consistency, i.e. $\langle S \rangle = S$. The obtained integrals

$$\langle S \rangle = \frac{\int_0^\pi \left(\frac{3}{2} \cos^2(\theta) - \frac{1}{2} \right) \exp(m \cos^2(\theta)) \sin(\theta) d\theta}{\int_0^\pi \exp(m \cos^2(\theta)) \sin(\theta) d\theta} = \frac{\int_{-1}^1 \left(\frac{3}{2} x^2 - \frac{1}{2} \right) \exp(mx^2) dx}{\int_{-1}^1 \exp(mx^2) dx}$$

may be calculated numerically. Figure 1.9 shows the numerical solution obtained. Zero is always a solution.

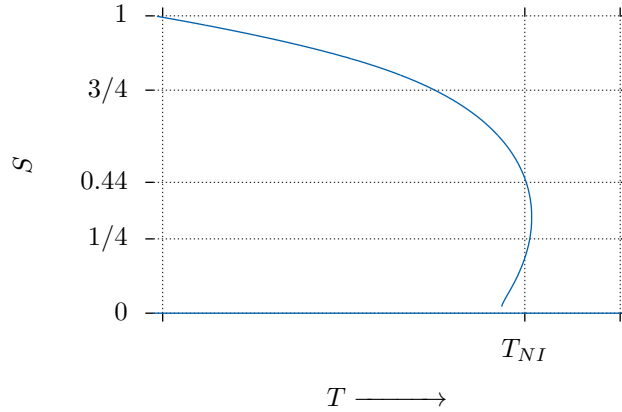


Figure 1.9: Numerically calculated values where $\langle S \rangle = S$ as a function of T (code in App. B.2).

For low values of $U/k_B T$ there are two solutions for $\langle S \rangle = S$ corresponding to minima in the Gibbs free enthalpy, zero is one of them. Zero corresponds to an isotropic and the other to a nematic fluid. In the vicinity of the transition, there is another unstable solution. To decide which one will physically be observed, one has to compare their free enthalpies. For T below

$$\frac{k_B T_c}{U(T_c)} = 4.55$$

the nematic phase is stable, whereas above that temperature, the isotropic state is stable [22], so at T_c the order parameter will discontinuously jump from zero to

$$S = 0.44$$

right below the transition [22].

1.5.1.3 Hexagonal Order Parameter

In order to determine hexagonal columnar phases, it is convenient to define another order parameter. The arrangement among the columns is characterised by the correlation of triplets of particles.

Those triplets are located in the neighbourhood of a particular particle. The correlation is then averaged over all particles and times. The hexagonal order parameter is defined as

$$\Psi_6 \equiv \left\langle \left| \frac{1}{N} \sum_j \frac{1}{|n_j|} \sum_{kl \in n_j} \exp(6i \cdot \theta_{kl}) \right| \right\rangle, \quad (1.15)$$

where $\langle \dots \rangle$ denotes the time average. The letter n_j denotes the set of neighbours of the j -th particle. The angle θ_{kl} is the angle between the two intermolecular vectors $\hat{\mathbf{r}}_{jk}$ and $\hat{\mathbf{r}}_{jl}$ of the two neighbours projected on the plane perpendicular to the j^{th} particles orientation vector. The neighbourhood of a particle is defined as the volume of a thick annulus, with the particle in its centre. The thickness is $1.5 \sigma_{\text{ff}}$, the radii of the small and large circle of the annulus $0.5 \sigma_{\text{ee}}$ and $1.5 \sigma_{\text{ee}}$, respectively. Other definitions may consider a cylindrical neighbourhood, but this reduces the values of Ψ_6 by reason of the non-perfect orientational alignment of the two particles stacked above and below the particle under consideration.

1.5.1.4 Local Nematic Order Parameter

In the confined system, in order to resolve the phase transitions over the pore radius, a local nematic order parameter is necessary. The order parameter is defined quite similarly to the hexagonal order parameter, for each particle, the nematic order in the neighbourhood is calculated. It is defined as

$$S_L \equiv \left\langle \frac{1}{N} \sum_i \frac{1}{|n_i|} \sum_{j \in n_i} S(n_i) \right\rangle. \quad (1.16)$$

The neighbourhood of the j -th particle this time is defined as a sphere of radius $1.5 \sigma_{\text{ee}}$. The nematic order parameter S is calculated by finding the largest eigenvalue of the tensor order parameter (Eq. 1.12).

1.5.1.5 Radial Distribution Function

Fluids, in contrast to ideal gases, possess short range spatial correlations. Like for crystals, these correlations can be observed via diffraction patterns. But, since there is no regular lattice in fluids, the diffraction patterns do not exhibit sharp peaks. X-ray and neutron diffraction experiments therefore can be performed in order to yield equilibrium static structure properties. The way incident light is spatially scattered into a pattern by a material is mathematically described by the static structure factor

$$S(\mathbf{k}) = 1 + \int_V e^{i\mathbf{k} \cdot \mathbf{r}} (g(\mathbf{r}) - 1) d\mathbf{r},$$

where $g(\mathbf{r})$ is the so-called pair correlation function or radial distribution function (RDF). While the density describes the probability of finding a particle in a region of space, the radial distribution function describes the probability of finding a second particle at the separation \mathbf{r} of a reference particle. It represents the average density distribution a particle of the system would see around itself.

Compared to the structure factor, the radial distribution has the advantage of its clear physical meaning and simplicity of visualising it.

For an isotropic fluid, the radial distribution only depends on the distance between two particles. For a complex fluid exhibiting nematic phase, the radial distribution looks different for the direction parallel to the nematic director and the direction perpendicular to it, due to the anisotropy of the nematic liquid crystal.

When a discotic liquid crystal is in a columnar phase, distinct peaks can be observed. On the

one hand, a LC in a columnar phase is a crystal in 2D, so the arrangement of the columns is static and ordered. For a hexagonal columnar phase Col_h , peaks in the *perpendicular* RDF at positions typical for a two dimensional hexagonal lattice are exhibited, i.e. $r_\perp = \sqrt{1+n+n^2} = \{\sqrt{3}, \sqrt{7}, \dots\}$, $n \in \mathbb{N}$.

The perpendicular RDF is defined as the probability distribution of finding a second particle at separation r_\perp perpendicular to the orientation vector of the first.

On the other hand, also the *parallel* RDF shows well resolved peaks in columnar phase, since it is an image of the density distribution. Therefore it shows the short range correlation also present in an ordinary liquid. The two pair distribution functions are calculated as

$$g_\perp(r) = \frac{V}{N^2 \sigma_{\text{ff}} 2\pi r} \left\langle \sum_i^N \sum_{i \neq j}^N \delta(r - r_{ij}^\perp) \theta(\sigma_{\text{ff}} - |r_{ij}^\parallel|) \right\rangle$$

and

$$g_\parallel(r) = \frac{V}{N^2 2\pi \text{d}r \sigma_{\text{ee}}} \left\langle \sum_i^N \sum_{i \neq j}^N \delta(r - r_{ij}^\parallel) \theta\left(\frac{\sigma_{\text{ee}}}{2} - |r_{ij}^\perp|\right) \right\rangle,$$

The two components of the intermolecular vector are calculated via

$$\mathbf{r}_{ij}^\parallel = (\mathbf{r}_{ij} \cdot \hat{\mathbf{e}}_i) \hat{\mathbf{e}}_i$$

and

$$\mathbf{r}_{ij}^\perp = \mathbf{r}_{ij} - (\mathbf{r}_{ij} \cdot \hat{\mathbf{e}}_i) \hat{\mathbf{e}}_i.$$

1.5.2 Additional Structural Properties

In order to characterise the more complex phase behaviour of the confined system, I introduce two more order parameters. We expect the system to show different behaviour from the bulk, since walls, when untreated, strongly favour face-on anchoring for discotics [23]. This could produce a kind of radial nematic phase.

1.5.2.1 Radial Nematic Order Parameter

To determine the degree of radial alignment imposed by the face-on anchoring next to the wall of a cylindrical pore, I introduce a *radial nematic order parameter*.

$$S_R \equiv \left\langle \frac{1}{N} \sum_i^N (\hat{\mathbf{e}}_i \cdot \hat{\mathbf{u}})^2 \right\rangle. \quad (1.17)$$

With the surface normal $\hat{\mathbf{u}}$. It is necessary to take the square of the scalar product to meet the head-tail symmetry of the discotic liquid crystals. For a system where all particles are oriented radially, it is one, while it is zero for a global nematic phase with the director coinciding with the pore axis. For the computation of the parameter, I took the vector $\hat{\mathbf{r}}$ for $\hat{\mathbf{u}}$ since $\hat{\mathbf{u}} \parallel \hat{\mathbf{r}}$ in the confined geometry, which is easy to compute.

In the case that the system reaches a nematic phase with the director pointing in a direction perpendicular to the pore axis $\hat{\mathbf{a}} = \hat{\mathbf{z}}$, we can expect S_R to take a value of approximately 0.5.

1.5.2.2 Axial Nematic Order Parameter

The opposite case of particles aligning along the pore axis can be quantified by an *axial nematic order parameter*. It is defined following the same scheme as for S_R

$$S_A \equiv \left\langle \frac{1}{N} \sum_i^N (\hat{\mathbf{e}}_i \cdot \hat{\mathbf{z}})^2 \right\rangle, \quad (1.18)$$

where the unit vector $\hat{\mathbf{z}}$ has been aligned with the pore axis. The combination of S_R and S_A gives us the possibility to spatially resolve the different alignments in very simple manner.

1.5.3 Dynamic Properties

Since the main interest in liquid crystals arises from their dynamical properties, i.e. self-organisation and defect healing properties, we will introduce the *van Hove Function* (VHF) and the *mean square displacement* (MSD) in the following, that will be important to characterise the dynamical properties.

1.5.3.1 Van Hove Function

From scattering experiments with slow neutrons ($\lambda \gtrsim 1\text{\AA}$) one can also analyse the energy distribution of the scattered neutrons. This yields the dynamic structure factor. Like for the static structure factor linked to the radial distribution function, there is a relatively easy function linked to the dynamic structure factor [24]. It is a generalisation of the RDF to the so called van Hove Function $G(\mathbf{r}, \Delta t)$, that depends on the spatial separation \mathbf{r} and the time interval Δt . I will only stick to the part relevant for Boltzmann statistics.

Without quantum effects $G(\mathbf{r}, t)$ has meaning similar to the RDF. It describes the average density at a given time $t_0 + \Delta t$ as seen from the position of a particle at time t_0 but it does not depend on the time t_0 . For the simplest case of $t = 0$, the VHF becomes the RDF.

In the present case the system is composed of distinguishable particles, so the VHF splits naturally into two parts, the first, called *self*, describes the average probability of finding the same particle at separation \mathbf{r} to its former position after the time interval Δt .

The second, so-called *distinct* part, describes the the average probability of finding another particle after Δt at a point $\mathbf{r}(t_0 + \Delta t)$ separated from the position of a particle at time t_0 .

For liquid crystals one distinguishes the parallel and perpendicular direction to the molecular orientation. The parallel and perpendicular displacements are

$$\begin{aligned} \mathbf{r}^{\parallel}(\Delta t) &= \{[\mathbf{r}(t_0 + \Delta t) - \mathbf{r}(t_0)] \cdot \hat{\mathbf{u}}_i(t_0)\} \hat{\mathbf{u}}_i(t_0) \\ \mathbf{r}^{\perp}(\Delta t) &= [\mathbf{r}(t_0 + \Delta t) - \mathbf{r}(t_0)] - \mathbf{r}^{\parallel}(\Delta t). \end{aligned}$$

The parallel and perpendicular components of the self part of the Van Hove Function (SVHF) are

$$G_s^{\parallel}(r, \Delta t) = \frac{1}{N} \left\langle \sum_i^N \delta(r - r_i^{\parallel}(\Delta t)) \right\rangle \quad (1.19)$$

and

$$G_s^{\perp}(r, \Delta t) = \frac{1}{N} \left\langle \sum_i^N \delta(r - r_i^{\perp}(\Delta t)) \right\rangle, \quad (1.20)$$

respectively. In the simple cases of diffusion in gases and liquids, the SVHF has approximately the form of a Gaussian. This also holds for harmonic oscillations in crystals. For the behaviour of the complex fluid under consideration, there will be a different behaviour.

The distinct part (DVHF) is convenient to characterise the collective motion of particles. For e.g. in a crystal one expects, that even after long time intervals, the probability of finding another particle at another lattice point is high, which will give sharp peaks in the DVHF for long t .

The parallel and perpendicular parts of the distinct van Hove Function are given as

$$G_d^{\perp}(r, \Delta t) = \frac{V}{N^2 \sigma_{\text{ff}} 2\pi r \, dr} \left\langle \sum_i^N \sum_{i \neq j}^N \delta(r - |r_{ij}^{\perp}(\Delta t)|) \theta\left(\sigma_{\text{ff}} - |r_{ij}^{\parallel}(t)|\right) \right\rangle$$

and

$$G_d^{\parallel}(r, \Delta t) = \frac{V}{N^2 2\pi r \sigma_{\text{ee}}} \left\langle \sum_i^N \sum_{i \neq j}^N \delta(r - |r_{ij}^{\parallel}(\Delta t)|) \theta\left(\frac{\sigma_{\text{ee}}}{2} - |r_{ij}^{\perp}(\Delta t)|\right) \right\rangle,$$

where

$$\begin{aligned}\mathbf{r}_{ij}^{\parallel}(\Delta t) &= \{[\mathbf{r}(t_0 + \Delta t) - \mathbf{r}(t_0)] \cdot \hat{\mathbf{e}}_i(t_0)\} \hat{\mathbf{e}}_i(t_0) \\ \mathbf{r}_{ij}^{\perp}(\Delta t) &= [\mathbf{r}(t_0 + \Delta t) - \mathbf{r}(t_0)] - \mathbf{r}^{\parallel}(\Delta t).\end{aligned}$$

When a high orientational correlation develops in the cylindrical nanoconfinement, we used a modified DVHF. In this case, the particle orientation vector $\hat{\mathbf{e}}_i(t_0)$ is changed to the cylinder axis $\hat{\mathbf{z}}$. The modified function can reveal structural reorganisations, as proposed by Busselez *et. al.* [18].

1.5.3.2 Mean Square Displacement and Self Diffusion

With the self part of the Van Hove Function being the probability of finding a particle at a displacement r after a time interval t one can easily calculate the mean square displacement $\langle r^2(t) \rangle$ [18], the expected value of $r^2(t)$. Again, we distinguish the parallel and perpendicular parts

$$\langle r_{\parallel}^2(\Delta t) \rangle = \int_0^{\infty} 2r^2 G_s^{\parallel}(r, \Delta t) dr \quad (1.21)$$

and

$$\langle r_{\perp}^2(\Delta t) \rangle = \int_0^{\infty} 2\pi r r^2 G_s^{\perp}(r, \Delta t) dr. \quad (1.22)$$

At short time scales, a particle is strongly correlated with its next neighbours. In this so-called collision regime $\langle r^2(t) \rangle$ grows as t^2 . The first dynamic regime is caused by a nearly free motion. At intermediate time scale, for dense fluids, a plateau in $\langle r^2(t) \rangle$ emerges, because of the frequent collisions with the first neighbour shell of the reference particle.

After the plateau follows the diffusive regime. As follows from the diffusion equation, the mean square displacement now increases linearly in time and is linked to the self-diffusion coefficient D

$$\langle r^2(\Delta t) \rangle = 3dD\Delta t$$

where d is the number of dimensions [25].

Chapter 2: Implementation

2.1 Model Parameters

The model potential used in the present work is presented in Eq. (1.11). It is parametrized as shown in Tab. 2.1,

Parameter	value
σ_{ff}/σ_{ee}	0.2
$\epsilon_{ff}/\epsilon_{ee}$	0.1
μ	1
ν	2

Table 2.1: Parameters used in the present work for the Gay-Bern potential.

These values were chosen in order to obtain a large columnar section in the phase diagram, since we are about to investigate the influence of the nanoconfinement mainly on the columnar phase. This model potential was proposed by Caprion *et. al.* 2003 [26]. The size anisotropy is representative for a hexa-azitrinaphthalene discotic molecule.

2.2 Simulations

The MD simulations were conducted using a parallel computing C/CUDA-code. There was an existing code working with the GBDI model potential (Eq. 1.9). I changed the existing code so that it uses the improved GBDII model potential (Eq. 1.11). The equations of motion are solve using a velocity-Verlet algorithm in the scheme of Ilnyitskyi and Wilson [27].

The simulations consisted of 10^5 iterations in isothermal-isobaric ensemble (NPT), starting from random initial positions and orientations. The timestep was set to $\delta t = 1.25 \cdot 10^{-4}$ which is rather small because the fluid-wall potential is quite steep, and to avoid the overlap of the molecular hard-cores for lager timesteps. For the implementation of the NPT ensemble an anisotropic barostat and a Nosé-Hoover thermostat are used. This first part is necessary for the equilibration of the system, because generating a random starting configurations requires a high initial volume. Also when starting a simulation with the results of a preceding simulation at higher temperature, an equilibration is necessary.

This first part is followed by the simulations of another 10^5 iterations in the canonical or NVT ensemble, writing out configurations every $500\delta t$. For the bulk system, periodic boundary conditions were applied on all three dimensions the simulations were then performed using $N = 5000$ particles, starting at a high temperature isotropic state, with the above procedure. The system was then subsequently cooled, with varying temperature steps ranging from 1.0 in stable regions, distant from phase transition points, down to 0.1 close to phase transitions. This is due to the fact that the liquid crystals tend to form domains of different orientation, when they are cooled from the isotropic into the columnar phase too fast, at least for pressures below $P^* = 100$. So this wide range of cooling steps was necessary to combine the explorations of large parts of the phase diagram with the careful determination of phase transitions.

The existing routine generating the random starting configurations also needed a change. The model used in this work exhibits a relatively high force and shape anisotropy. The existing code checked the distance from each placed particle to the already placed particles. When it was too close to one of them, which would lead to high energies, it called a retry of the random placing for the particle.

This distance check was extended to check the distances parallel and perpendicular to the particles director separately. In this way denser starting configurations were produced. The the equilibration process was thereby shortened. For the bulk simulation the random initial orientation of particles was implemented with a preferred axis because the system tended to crystallise in multiple domains otherwise.

2.2.1 Confinement

The existing CUDA-code already had a fluid-wall interaction potential, originally for calamitic LC confined between two planes. The corresponding routine, already called with the right flags, and the allocation of the GPU cores for the calculations of the force and torque for each particle therefore just had to be modified to fit the data dependency needs and to calculate a different interaction. As before only the essential data is passed to the GPU units, since data transmission should be held at minimum.

Other changes, that were applied on the code are:

Periodic boundaries

Change of the periodic boundary of the bulk simulation, throughout the whole code, so that periodicity is just kept in the z -direction of the pore axis. Also the volume changes in cylindrical confinement.

Barostat

The code works with a barostat, changing the size of the simulated space. Particle positions are stored in a unit box. On the one hand, this way the periodic boundary condition can be calculated with the efficient `rint()` function, on the other hand only the simulation-box sidelengths have to be modified by the barostat algorithm. Due to the static pore diameter, the anisotropic barostat originally working in each x , y and z direction had to be changed. The strength of the barostat additionally had to be adapted to the new conditions.

Initial configuration

The function placing particles randomly had to be modified, so that it places the particles in the pore and keeps some distance to the wall. Otherwise the initial configuration contains huge energies, which can lead to unrealistic events and crashes. The simulations using edge-on anchoring were performed starting with an initial configuration similar to the bulk counterpart, with a preferred orientation along the pore axis. For the other case of face-on wall anchoring, the initial configuration was created placing particles with a preferred orientation parallel to radial direction.

Output

The data output has to compute the new fluid-wall interaction energy.

The confined system was in general simulated the same way as the bulk counterpart. Since the most common discotic liquid crystal molecules used in experiments are triphenylene and pyrene derivatives, which have a comparable diameter of ca. 2 nm, pore diameters $d = 3\sigma_{ee}$, $d = 5\sigma_{ee}$ and $d = 10\sigma_{ee}$ have been used in order to cover the range of the pore diameters investigated experimentally [17]. For the two larger pore diameters I simulated $N = 3500$ particles, for the smaller diameter $N = 1260$. This way, the system was always bigger than the cutoff length of the force calculations.

2.3 Data processing

In order to compute the quantities and order parameters presented in the aforementioned, several other programs were necessary. With an existing code for the nematic order parameter S and the radial distribution function, I wrote programs computing the following quantities

- (i) hexagonal order parameter
- (ii) radial and axial nematic order parameter
- (iii) local nematic order parameter
- (iv) spatial resolved order parameters for state points
- (v) order parameters as a function of temperature, for different layers in the pore
- (vi) self and distinct parts of the van Hove function, for confinement also modified to take the pore axis as orientation vector
- (vii) radial distribution functions for $t = 0$ case of the DVHF
- (viii) mean square displacements calculated via the SVHF

The hexagonal order parameter has been implemented using a neighbour list, in order to reduce the computational cost of three nested `for` loops. The calculation of the DVHF is quite expensive because correlation has to be calculated between all times i.e. written configurations (`nconf`) and all particles. The computation time scales with

$$t \sim \mathcal{O}(N^2(\text{nconf})^2).$$

To compensate this, I parallelised the computation of 1.-3. and 6. with the `OpenMP` protocol.

Chapter 3: Results

3.1 Bulk

Although the main goal and focus of this thesis is the study of confined discotic liquid crystals, we studied also bulk systems to fully understand the effects of confinement on the structure and dynamics of discotic liquid crystals.

The bulk liquid crystal exhibits four different phases as a function of temperature and pressure. These are a orthorhombic body-centred crystal phase (Cr), a large hexagonal columnar region (Col_h), a nematic region (N) at high pressure and an isotropic phase (I).

3.1.1 Order Parameters

The phase behaviour can be studied easily using the nematic and hexagonal order parameters S and Ψ_6 , respectively. Figure 3.1 shows the dependence of these order parameters on temperature, each at a different fixed pressure.

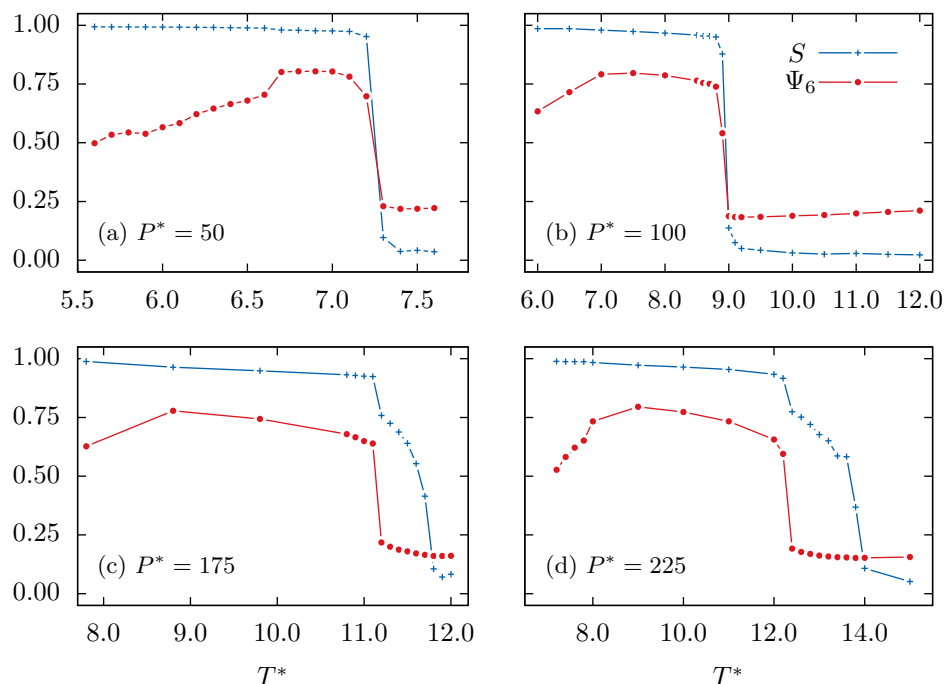


Figure 3.1: Dependence of the nematic and hexagonal order parameters S (blue) and Ψ_6 (red) on temperature, for different fixed pressures. Pressures are labelled in the bottom left hand side of each plot.

The order parameters exhibit sharp jumps between high and low temperature domains, which shows the first order behaviour of all phase transitions.

In Fig. 3.1(a) and 3.1(b) we can see that the system directly goes from the isotropic into the nematic phase, as the jumps in the the order parameters appear simultaneously. The hexagonal order parameter takes values of ca. $\Psi_6 = 0.8$ while the nematic order increases nearly up to the maximum of $S = 1$. At low temperatures, Ψ_6 decreases again (Fig. 3.1(a)), which corresponds to the transition into the crystal phase, that does not show D_{6h} symmetry, but still orientational

correlation, reflected in the large value of the nematic order parameter. We can also see, that the crystal posses higher orientational order, since the transition also introduces a slight increase in the nematic order.

Figures 3.1(c) and 3.1(d) reveal that, at high pressure, the system also has a nematic phase. When following the order parameters from high to low temperature, the system exhibits nematic orientational order, before exhibiting hexagonal symmetry. In the evolution of S we can also see the likeness of the isotropic to nematic phase transition desired by the Maier-Saupe theory (see. Fig. 1.9). The transition from the nematic into the hexagonal phase also shows behaviour of a first order transition. In Fig. 3.1(d) we can again see the transition into a crystal, accompanied with a decrease in Ψ_6 . We can also see, that the crystal possesses higher orientational order, since the transition also introduces a slight additional increase in the nematic order.

3.1.2 Structural Properties

To study the structure within the different phases in more detail, the radial distribution function (RDF) is convenient. We show the parallel in Fig. 3.2(a) and perpendicular Fig. 3.2(b) for different temperatures at constant pressure of $P^* = 50$.

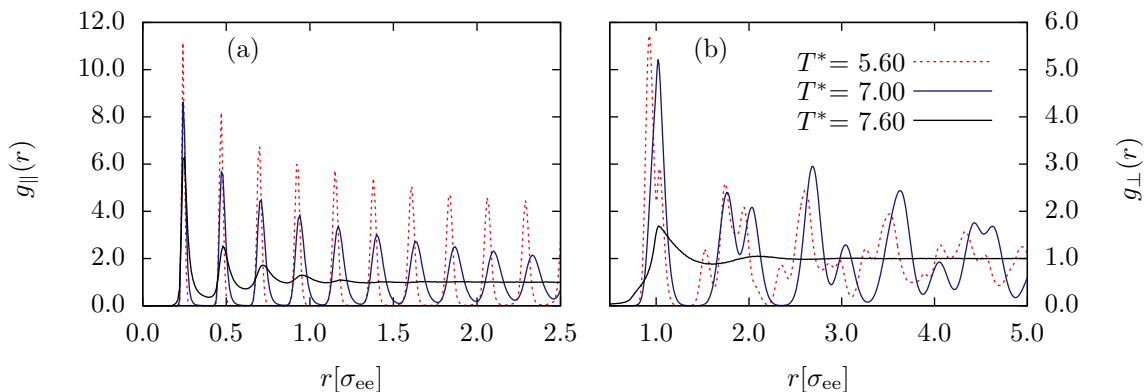


Figure 3.2: (a) Parallel and (b) perpendicular part of the RDF at $P^* = 50$, for temperatures revealing the 3 different phases Cr (dotted red), Col_h (blue) and I (black).

The red curves in Fig. 3.2(a) and 3.2(b) show the pair correlation in the crystal phase. The particles are close packed in the direction parallel to the particle orientation due to the particles shape anisotropy and orientational correlation. The parallel radial distribution function does not take the body-centred neighbours into account, by its definition. In Fig. 3.2(b) we can also see the peaks for the body-centred neighbour and the next neighbour in the cuboid, both close to $r_{\perp} = 1$. In the blue curve in Fig. 3.2(b) we can see peaks, characteristic for a hexagonal phase, at $r_{\perp} = \sqrt{3}\sigma_{ee}, \sqrt{7}\sigma_{ee}, \dots$ and multiples, together with the peaks at multiples of σ_{ee} .

Also the columnar nature of the phase is reflected in the peaks at multiples of approximately σ_{ff} in the parallel RDF 3.2(a) (blue curve). As expected, they are more loose and more distant than in the crystal.

The decay of the height of the probability peaks suggest a finite correlation length for the columnar phase at the picked points of the phase diagram.

The isotropic phase, drawn in black, shows a first neighbour shell in the perpendicular direction and a stronger positional correlation in the parallel direction, that we can expect to vanish at higher temperatures. At long ranges, the probability density approaches unity, agreeing with the uniform density of a liquid phase.

Figure 3.3 shows the RDF at $P^* = 175$, from which we can compare the structural behaviour of the nematic phase with the columnar and isotropic phase.

We can see that the nematic phase shows a first neighbour shell like the isotropic phase. Also, both RDFs of nematic and isotropic phase approach unity at larger distances. As a result of the

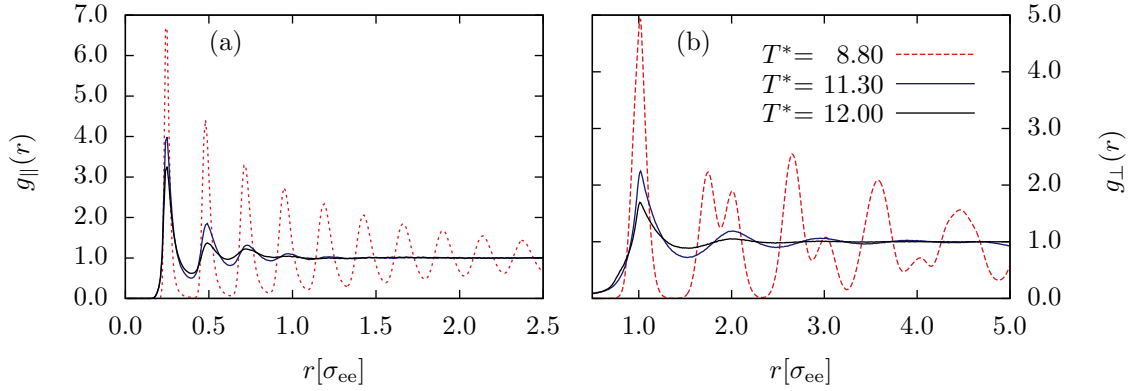


Figure 3.3: (a) Parallel and (b) perpendicular part of the RDF at $P^* = 175$, for temperatures revealing the 3 different phases Col_h (dotted red), N (blue) and I (black).

orientational order, the nematic phase shows a longer range of positional correlation in the parallel direction.

The correlation length along the parallel direction in the Col_h appears to be smaller in the higher pressure, we see that $g_{\parallel}(r)$ approaches unity much faster in Fig. 3.3(a) than at $P^* = 50$ in Fig. 3.2(a). Both curves correspond to the maximum of Ψ_6 in 3.1(a) and 3.1(c), respectively.

3.1.3 Dynamic Properties

Our interest in liquid crystals mainly arises from their dynamic properties. They are fluid while exhibiting orientational order in the nematic phase, and fluid in one dimension in the hexagonal phase. We will see this behaviour in the following.

3.1.3.1 Self-Diffusion and Mean Square Displacement

As we can see in Fig. 3.4, the self-diffusivity of the model liquid crystal changes over 5 orders of magnitude in the direction parallel and perpendicular to the molecular director.

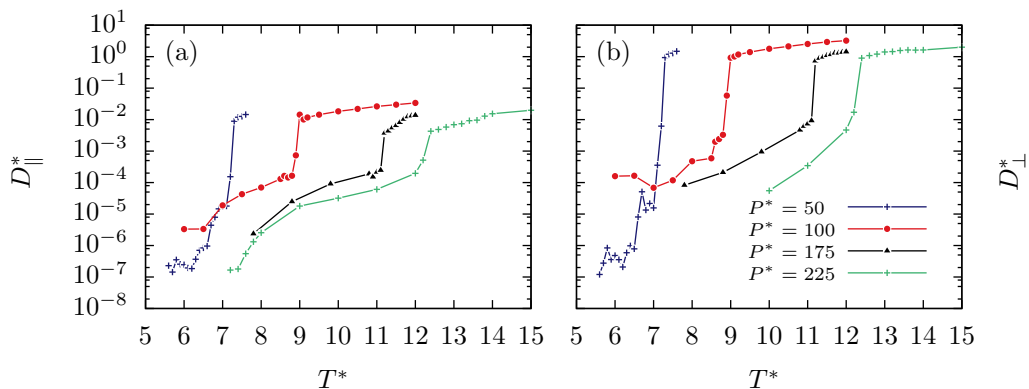


Figure 3.4: Reduced self-diffusion coefficients D^* (a) parallel and (b) perpendicular to the molecular orientation as a function of temperature for different pressures

The data at the lowest temperatures for the perpendicular direction is not very reliable, due to the relatively short simulation time and the low self-diffusivity, in the columnar phase. From the MSD, we see that particles do not change their lattice point, at some phase points. This made

linear fits to the mean square displacement difficult. Following a curve from the low temperature region in Fig. 3.4, we can first see that the self-diffusivity increases with the transition from crystal to columnar phase. There is also self-diffusivity in the perpendicular direction, more than in the parallel direction. The parallel self-diffusivity then increases with decreasing slope, while in the columnar region.

The transition into the isotropic phase occurs with a sudden increase in the self-diffusivity, as we can see from pressures $P^* = 50$ and $P^* = 100$.

At pressures $P^* = 175$ and $P^* = 225$ the system exhibits also the nematic phase. Here we see an approximately linear increase of the self-diffusivity for $T \in [11.1, 11.7]$ and $T \in [12.2, 13.5]$, respectively, after the same jump at the transition from the columnar to nematic phase.

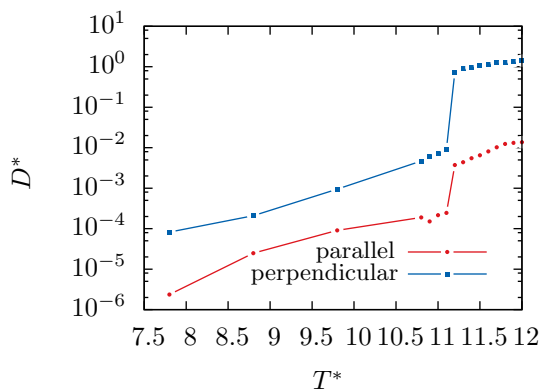


Figure 3.5: Diffusion coefficients in the parallel direction for pressure $P^* = 175$ as a function of temperature.

In Fig. 3.5 we directly compare the parallel and perpendicular part of D^* . The increase in the self-diffusivity in the nematic region is much stronger in the perpendicular part. The perpendicular self-diffusivity reaches much higher values in the isotropic phase, which is a result of the relatively small perpendicular pair correlation length in the nematic and isotropic phase, that we were able to see in Figs 3.2(a) and 3.3(a). Even in the isotropic phase, particles still form stacks of 3 or 4, as suggested by the strong peaks indicating the first and second neighbour shell in this direction.

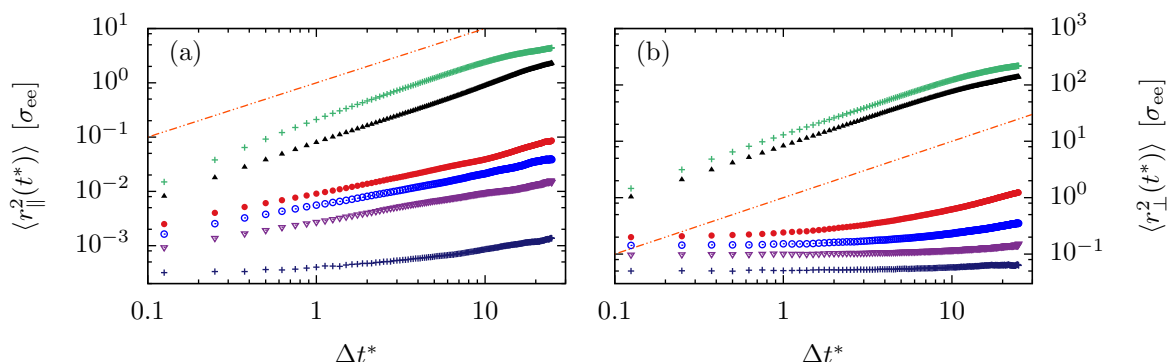


Figure 3.6: Mean square displacement for $P^* = 175$. Blue crosses for $T^* = 7.80$, purple triangles for $T^* = 8.80$, empty yellow circles $T^* = 9.80$, red dots $T^* = 10.80$, black pyramids $T^* = 11.30$ and green crosses for $T^* = 12.00$. The grey line has the slope characteristic for the diffusive regime.

Figure 3.6 shows the mean square displacement for different temperatures at constant pressure. For the highest two temperatures plotted, we can see a decrease of the slope due to the effects of the finite cutoff range, used for the calculation of the SVHF. As the mean particle velocity times

the observation time gets much higher than the cutoff range, this leads to errors. The particles still appear to be relatively slow, so that the decrease of the MSD only starts at long times. We can also see that the effect gets shifted to the left, as the mean particle velocity increases with temperature (see Fig. 3.6(b) black and green curves). But as we are already in the diffusive regime and only interested in the slope, the data is still useful. Unfortunately the linear time interval I chose was not sufficiently small to cover the ballistic regime. On the right hand side we can also see, that only the red curve exceeds 1 at the timescale of the simulation. This suggests that we have to perform longer simulations in order to describe self-diffusivity reliably.

Figure 3.7 shows the SVHF for a reduced pressure of $P^* = 50$.

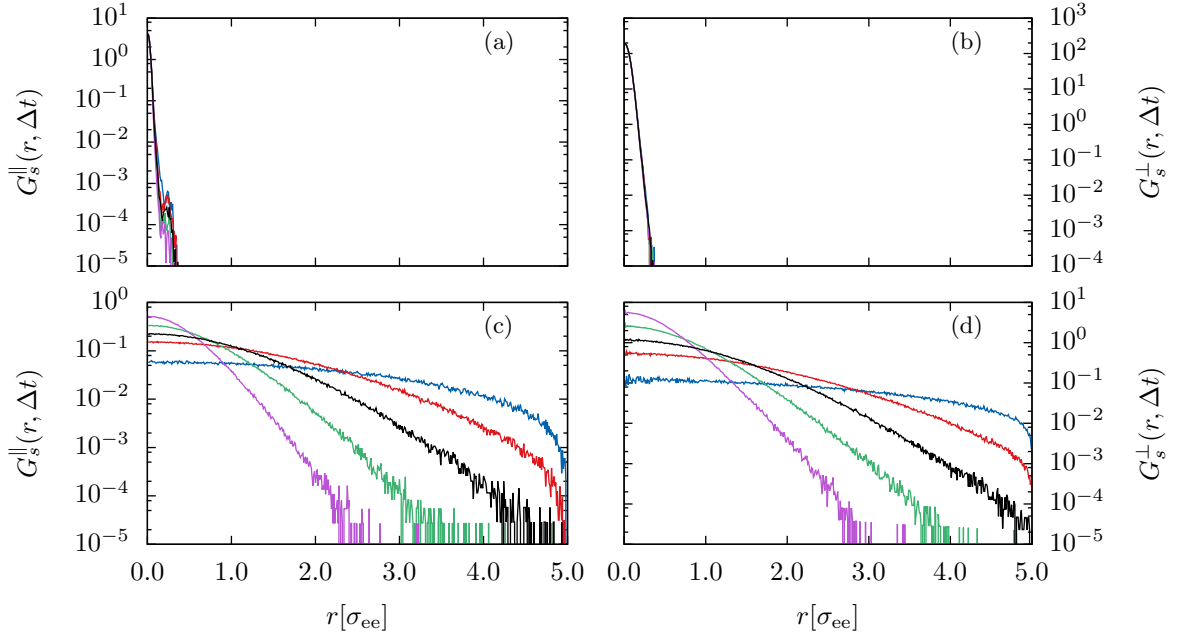


Figure 3.7: Parallel SVHF in panels (a) and (c), perpendicular SVHF in panels (b) and (d), all at $P^* = 50$. The top upper panels are points in crystal phase ($T^* = 5.60$), the lower isotropic phase ($T^* = 7.60$). The colours purple, green, black, red and blue correspond to curves for time intervals Δt^* equal to 2.5, 5, 10, 20 and 80, respectively.

We can see the approximately Gaussian shape for both the crystal (top panels) and the isotropic phase (bottom panels).

In Fig. 3.8(b) we can also see the crystalline nature of the columnar phase in the perpendicular direction by a Gaussian at $r = 0$. Figure 3.8(a) on the other hand shows, that columns drift along their axis, with respect to each other, since the the SVHF broadens with time. In Fig. 3.2 we can see the RDFs corresponding to those phase points with $P^* = 50$.

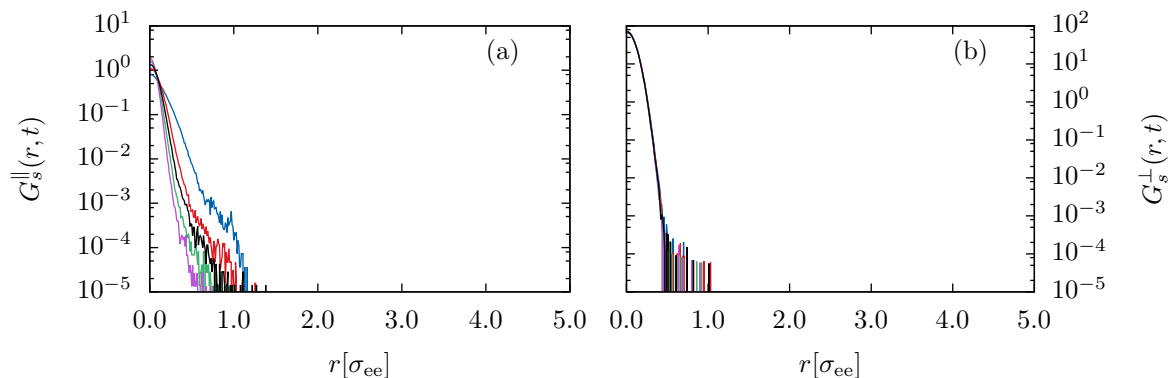


Figure 3.8: Parallel SVHF in panel (a) and perpendicular SVHF in panels (b), for $P^* = 50$, $T^* = 7.00$, corresponding to the Col_h phase. The colours purple, green, black, red and blue correspond to curves for time intervals Δt^* equal to 2.5, 5, 10, 20 and 80, respectively.

At pressures higher than $P^* = 50$ we can see that particles can hop from one column to the next.

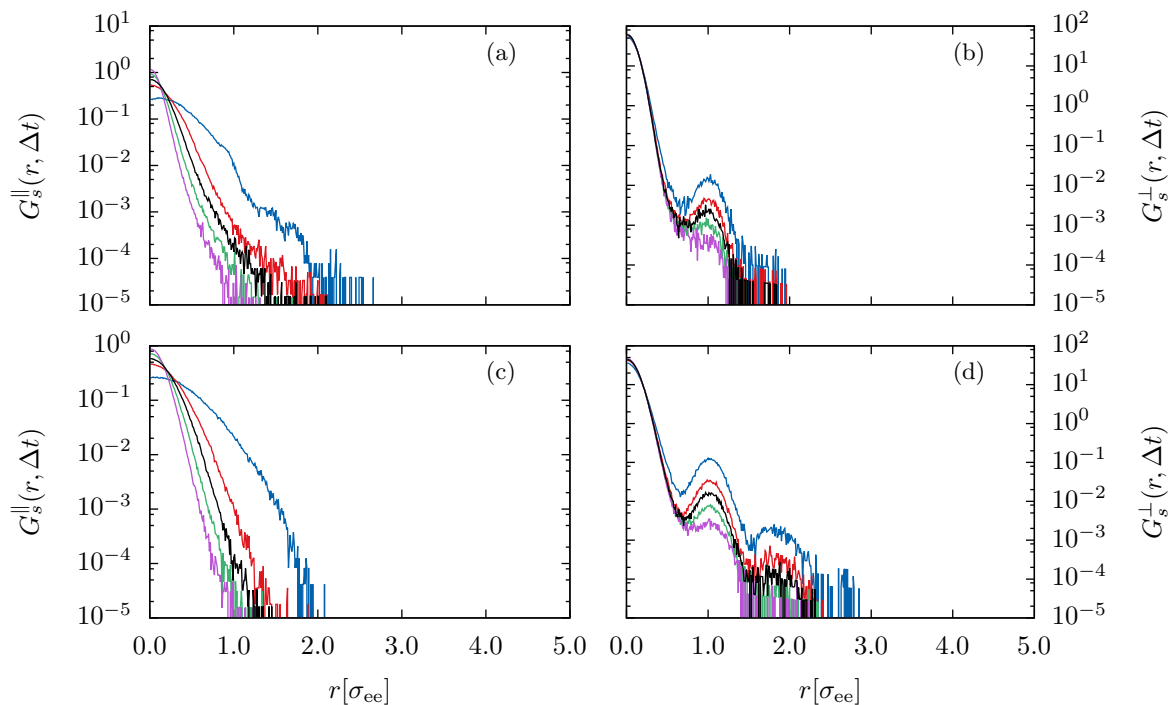


Figure 3.9: Parallel SVHF in panels (a) and (c), perpendicular SVHF in panels (b) and (d). **Top panels:** $P^* = 100$, $T^* = 8.5$ - **bottom panels:** $P^* = 175$, $T^* = 10.8$. All panels are state points in the hexagonal phase. The colours purple, green, black, red and blue correspond to curves for time intervals Δt^* equal to 2.5, 5, 10, 20 and 80, respectively.

The peak at $r^\perp = 1$ in Fig. 3.9(b) tells us that if a particle was at the origin at the beginning, we may find it displaced by $r^\perp \approx 1$, i.e. in the next column after a sufficient time interval. This hopping between columns has also been observed by Busselez *et. al.* [18]. Figure 3.9(c) and (d) show an increase of the hopping at higher pressure, together with an increase of the self-diffusivity, i.e., a broadening in Fig. 3.9(c) compared to the upper panels. The two blue lines in 3.9(b) and (d) reveal that on average, a particle changes its column one, respectively two times, in a time interval $\Delta t = 80$.

To study the dynamics of the structure the DVHF is the method of choice. In Fig. 3.10(a) and (b) we can see that the crystal phase is stable over the whole simulation time as we expect, because the DVHF keeps the form of the RDF over all time intervals. In contrast, we can see that short range spatial correlations decay fast also in time in the isotropic phase. The DVHF in Fig.3.10(c) and (d) is constant even for relatively short time intervals.

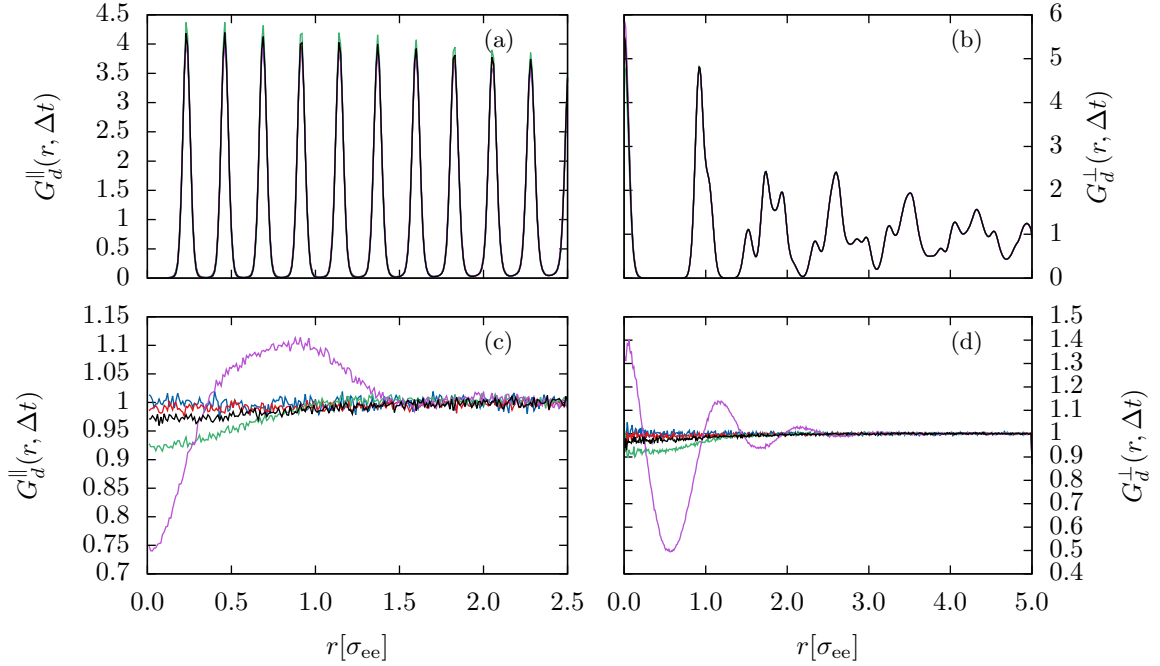


Figure 3.10: Parallel SVHF in panels (a) and (c), perpendicular SVHF in panels (b) and (d), at $P^* = 50$. The two upper panels are state points in the crystal phase, the lower isotropic phase. The colours purple, green, black, red and blue correspond to curves for time intervals Δt^* equal to 1.25, 5, 10, 20 and 80, respectively.

In Fig. 3.11 we can see a good example for the dynamic properties of the hexagonal columnar phase. It is fluid in the parallel direction (a), the positional correlation we can see at the shortest time interval (purple) decays quite fast, becoming uniformly distributed equal to Fig. 3.10(c).

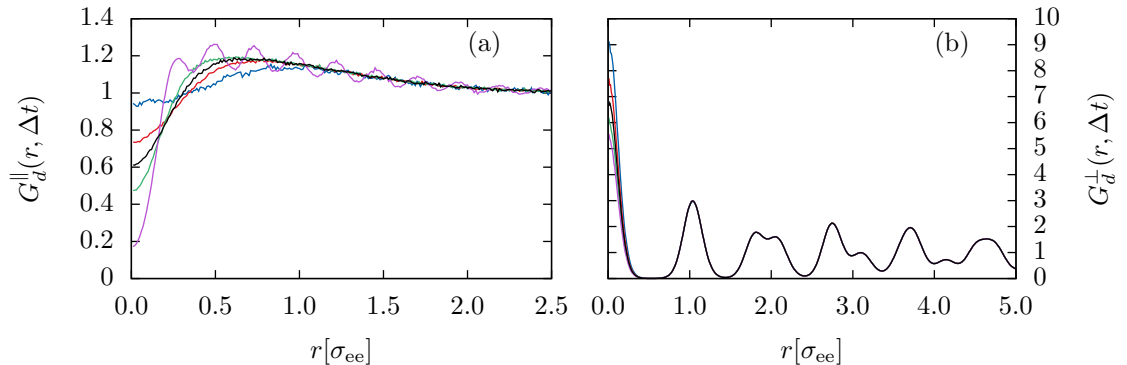


Figure 3.11: Parallel DVHF (a), perpendicular DVHF (b), at $P^* = 175$, $T^* = 10.8$. Both panels are for state points in the hexagonal phase. The colours purple, green, black, red and blue correspond to curves for time intervals Δt^* equal to 1.25, 5, 10, 20 and 80, respectively.

In the perpendicular direction (Fig. 3.11(b)) we can clearly see the crystalline behaviour similar

to Fig. 3.10(a) and (b). The hexagonal lattice persists for the whole simulation time.

3.1.4 Phase Diagram

Through the analysis of the properties discussed in the previous sections, a complete phase diagram can be drawn. A crystal phase can be identified with high nematic and low hexagonal order, low diffusivity, and a stable structure. The columnar phase also possesses high orientational order, hexagonal order, a stable specific structure in two dimensions and more fluid like properties in the remaining dimension. The nematic phase exhibits orientational order.

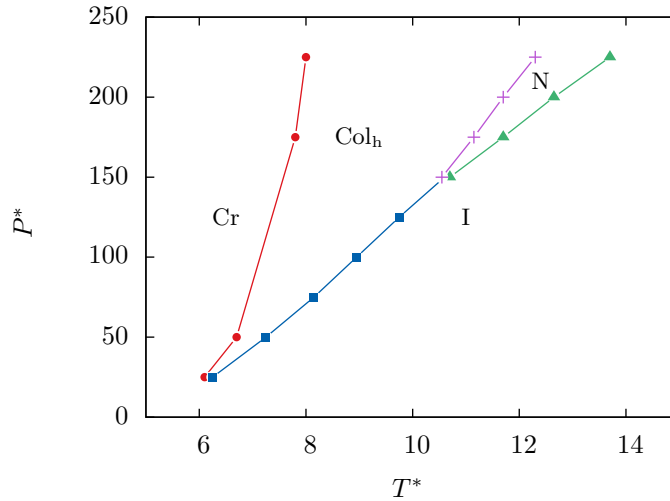


Figure 3.12: Phase diagram for the bulk system.

The phase diagram closely resembles the behaviour of the model investigated by Caprion *et. al.* [26]. I observed the two predicted triple points Cr-Col_h-I and Col_h-N-I, the latter one at the predicted location of $P_t^* = 150$, $T_t^* = 10.5$. The first one appears to be right below $P^* = 25$, the difference between the two transition temperatures T_{ColCr}^* and T_{ICol}^* at $P^* = 25$ is about a tenth of a reduced temperature unit.

3.2 Confined System

For the confined system, we expect that the imposed symmetry of the cylindrical confinement will have effects on the phase transitions for the edge-on anchoring, on the one hand stabilising the D_{6h} symmetrical columnar phase, on the other hand affecting the lateral arrangement between the columns. For the other case of face-on anchoring, we expect that the imposed symmetry and the anchoring force rival. The first favours an axial orientational order of columns, i.e. along the pore axis, the latter a radial.

Since the imposing of the symmetry depends on the pore diameter, I investigated the effect of three different diameters, thereunder $3\sigma_{ee}$, $5\sigma_{ee}$ and $10\sigma_{ee}$.

I chose the wall interaction strength in the face-on anchoring case twice the strength of the edge-on case, $\epsilon_{fw} = 2.5\epsilon_{ff}$, because both entropy and fluid-fluid interactions favour the edge-on anchoring case. Therefore, I expected it to be more difficult to obtain face-on anchoring, but although I probed the PT -plane intensively, face-on anchoring never occurred. This is contradicting experiments, which show that the face-on alignment is quite dominant [17]. Increasing the wall interaction strength above 4 times the edge-on value yielded visible effects.

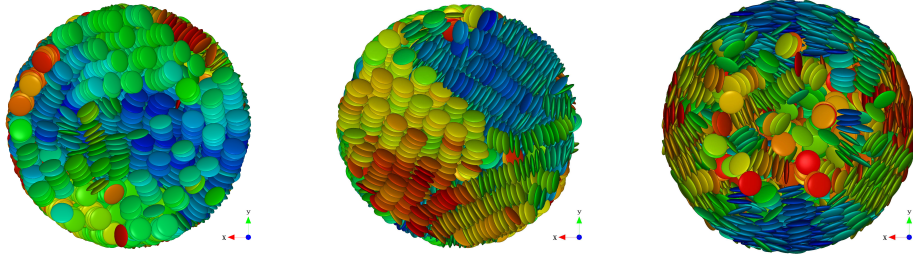


Figure 3.13: Snapshots from simulations with three different energies. From left to right: $\epsilon_{fw} = 10\epsilon_{ff}$, $20\epsilon_{ff}$ and $80\epsilon_{ff}$, all at $P^* = 50$, $T^* = 6.75$. The view is into the pore from above. The pore diameter is $10\sigma_{ee}$

Figure 3.13 shows snapshots from a temperature at $P^* = 50$ where the bulk counterpart is in columnar phase. This low pressure is chosen because although the columnar region of the phase diagram becomes larger with increasing pressure, also the effect of the symmetry imposed by the confinement becomes stronger with increasing pressure. I investigated the behaviour for higher interaction strengths, i.e. $\epsilon_{fw} = 10\epsilon_{ff}$, $20\epsilon_{ff}$, $40\epsilon_{ff}$ and $80\epsilon_{ff}$. The first two interactions strengths still do not resemble the actual behaviour [20, 17]. Columns orient tilted or along the wall, but with the axis perpendicular to the pore axis.

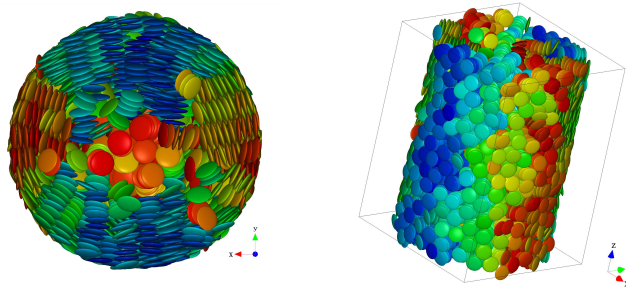


Figure 3.14: Snapshots of $\epsilon_{fw} = 40\epsilon_{ff}$, also at $P^* = 50$, $T^* = 6.75$. The pore diameter is $10\sigma_{ee}$

The highest energy value prohibits the formation of hexagonal arranged columns. However, it shows an interesting behaviour. In the outer section, radially oriented columns dominate while the pore centre seems to be in an isotropic state. For thorough investigations I chose the intermediate

interaction strength of $\epsilon_{fw} = 40\epsilon_{ff}$. The system shows an outer, radially aligned section and a different behaviour in the pore centre. The rim is quite large and exhibits correlation between columns. All the snapshots are taken from cooling runs with the described procedure, all started in the bulks isotropic state.

3.2.1 Face-on Anchoring

3.2.1.1 Pore Diameter $10\sigma_{ee}$

As for the bulk system, we can see the T dependence of the order parameters S and Ψ_6 in Fig. 3.15. The additional order parameters for the confinement are also shown. The T dependence of the S_R is shown in the green curve, the S_A in purple and the local nematic order S_L in black. Figure 3.15 shows the order parameters describing the state point of the snapshots in Fig. 3.14. Compared to the bulk, different behaviour occurs for every pressure. In the following we will go through the different pressures from low to high to discuss the different structures and phases encountered.

Radial Regime - At $P^* = 50$ the system has a very clear radial orientation of the particles even at $T^* = 8.0$ in the isotropic state. As T decreases, S_R increases to and stays over $\frac{3}{4}$, clearly indicating radial alignment.

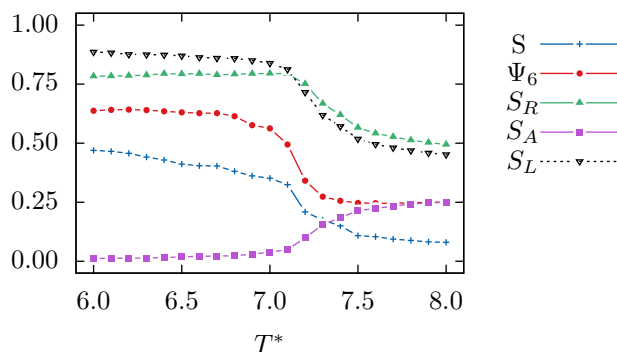


Figure 3.15: Temperature dependence of the nematic S (blue), local nematic S_L (black), radial nematic S_R (green), axial nematic S_A (purple) and hexagonal Ψ_6 (red) order parameters for $P^* = 50$.

The transition into the hexagonal phase appears at a lower temperature than in the bulk and changes into a continuous increase of Ψ_6 with decreasing temperature. The values of Ψ_6 increase to approximately 0.64 which is clearly below those of the bulk counterpart. We can assume, that this arises from the spatial restrictions. The continuous nature of the I-Col_h phase transition has also been reported by Busselez *et. al.* who investigated the phase diagram at $P^* = 100$ for a pore diameter of $5\sigma_{ee}$ with an orientation independent wall interaction [18].

The nematic order parameter S also changes in a continuous fashion, but it stays below 0.5, indicating that there is no global orientational alignment in a specific direction.

In general, the system exhibits one strong transition around $T^* = 7.25$, which involves a complete disappearance of orientational alignment along the pore axis upon cooling. Comparing the green and black curves at low T , we can see, that at higher temperatures, the radial alignment beats the local nematic order. That changes below $T^* = 7.25$, where the radial alignment slightly decreases while the local nematic order grows. This marks a change in the control of alignment from a regime dominated by the confinement before, into a regime where the fluid-fluid interaction plays a larger role.

We can conclude that there is a “quasi-radial-nematic” phase at larger temperature, followed by a radially oriented hexagonal columnar phase, at lower T .

Furthermore, the columnar phase shows several structural changes, involving increases in both the order parameters S and Ψ_6 interrupted by plateaus, one around $T^* = 7$, the other around $T^* = 6.75$, which is better visible in Fig. 3.16. The remaining high radial orientational order indicates the growth of larger radially aligned hexagonal columnar domains. The snapshot in Fig. 3.14 indicates the behaviour in the pore centre to differ from that close to the wall. To characterise this, we look at the order parameters developing in layers around the centre of the pore.

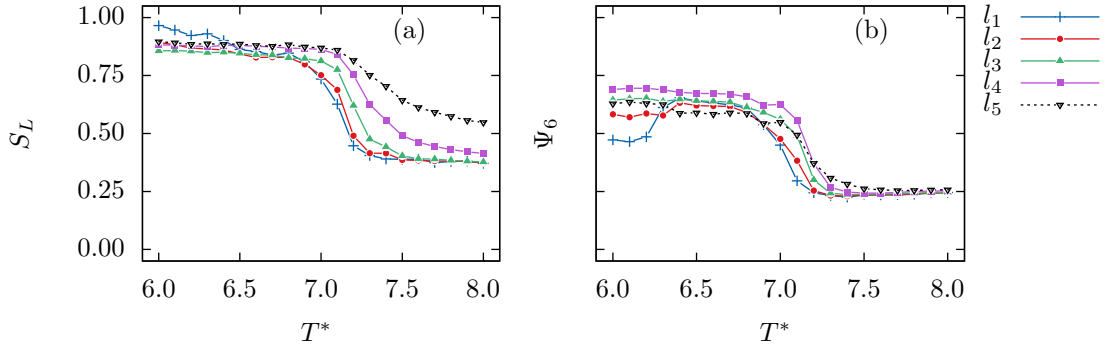


Figure 3.16: Local nematic (a) and hexagonal (b) order parameters for different layer l_i around the pore centre as a function of temperature at $P^* = 50$. The blue curve titled “ l_1 ” shows the centre cylinder of radius σ_{ee} , the others show the values for layers of thickness σ_{ee} , numbered from inside to outside.

Starting at higher temperature, the local nematic order is much higher close wall, further the transition is more continuous. Apart from the wall, the transition is faster and also at lower temperature. The columnar phase nucleates at the wall, as indicated by Ψ_6 . This behaviour is also predicted by a Landau-de Gennes analysis combined with splay deformations [17]. At very low temperature, nematic order in the centre grows again, taking on the maximum value. Ψ_6 show three transitions, when following the curves with decreasing temperature. One continuous, followed by a rapid change for the outer regions, and one below $T^* = 6.4$. The spatial restrictions

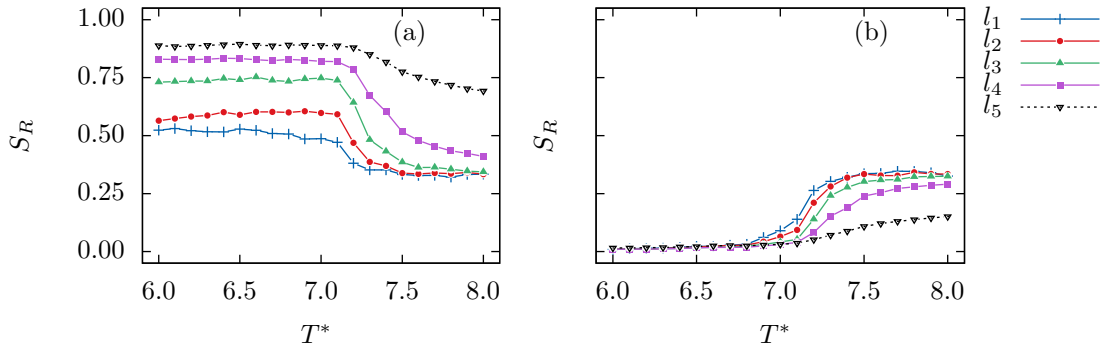


Figure 3.17: Radial (a) and Axial (b) nematic order for different layers around l_i the pore centre as a function of temperature at $P^* = 50$. Labelling follows the same scheme as in Fig. 3.16.

close to the wall hinder the hexagonal alignment, as can be seen by the black curve in Fig. 3.16(b) staying below all the others except the core. The low temperature increase in S_L in the pore centre is accompanied with a decrease in Ψ_6 while it increases close to the wall at the same time. The transition into the radial columnar phase goes along with the disappearing of particles aligning parallel to the pore axis in all regions, as shown by S_A in Fig. 3.17(b). We can also see, that the strong short range correlation indicated by the increasing S_L between particle leads to a lowering

of N_R in the pore centre, where radial alignment would need strong deformations. This can be interpreted as the final state and end of the growth of columnar domains. Compared to the bulk system which we have seen crystalline at $P^* = 50$, $T^* = 6.7$, in confinement the crystal phase is pushed to lower temperature.

To take a closer look at these multiple transitions, Fig. 3.18 shows the RDF. The blue RDF does not show a big structural difference from that show by the black, but the peaks moved towards the origing, indicating, that the system is packed denser.

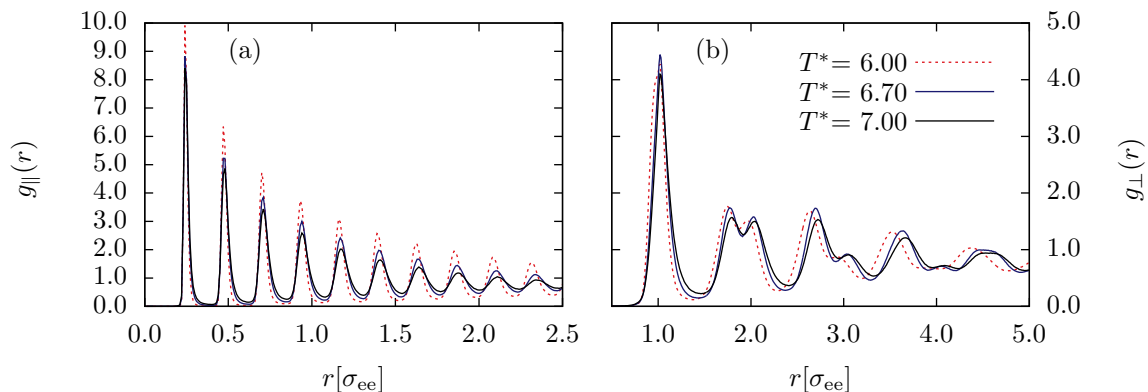


Figure 3.18: (a) Parallel and (b) perpendicular part of the RDF at $P^* = 50$, for temperatures in the observed 3 different plateaus.

The radially alignment of the columns is reflected by the quick decay of the perpendicular RDF to unity, because the correlation in radial aligned columns is smaller. At $T^* = 6.0$ (red in Fig. 3.18) the trend pursues, the peaks approach the offspring further and additionally the next neighbour peak in the perpendicular direction is below unity, which suggests the presents of crystal domains. The sequence of peaks is more one of a hexagonal phase though.

The DVH (Fig. 3.19) for the states at $T^* = 6.00$ and at $T^* = 6.70$ indicates that the warmer one is in a columnar phase, although the correlation in the direction parallel to the particle's orientation is smaller for small time intervals, and it lasts longer, compared to the bulk system.

At $T^* = 6.00$ the correlation decays after relatively small distances compared to the bulk, the high peaks and slow decay with time though suggest a transition regime between crystal and hexagonal columnar phase. Anyway, it is difficult to separate the effects of the different orientations of the domains present in this state from the general translational correlation.

The SVHV (Fig. 3.20) reveals that particles are more mobile than in the bulk columnar phase, even at $T^* = 6.00$. Though, it is not possible to say where this higher mobility takes place, from the data. The pore centre or the layer close to the wall may be candidates.

Competing Regimes - At the higher pressure $P^* = 100$ and $P^* = 150$ in Fig. 3.21(a) and (b), we see some similarities with the behaviour at half the pressure.

The S_R indicates that there still is a preference of radial orientation of particles at state points in the isotropic phase.

At about $T^* = 9.75$ we can see that the systems undergoes a slight transition into a radial nematic phase, as indicated by the increased S_R and S_L , coinciding with a drop in the S_A . The radial orientation increases in a more than linear manner afterwards, upon cooling. Furthermore, we can see that there already seems to be a global trend in the particle orientation, indicated through a simultaneous increase in the nematic order parameter S .

As the local nematic order S_L further increases, the radial nematic phase gives way to an overall orientational correlation. The simultaneous increase in Ψ_6 indicates the growth of a globally expanded columnar domain, which posses some degree of D_{6h} symmetry. The transition occurs

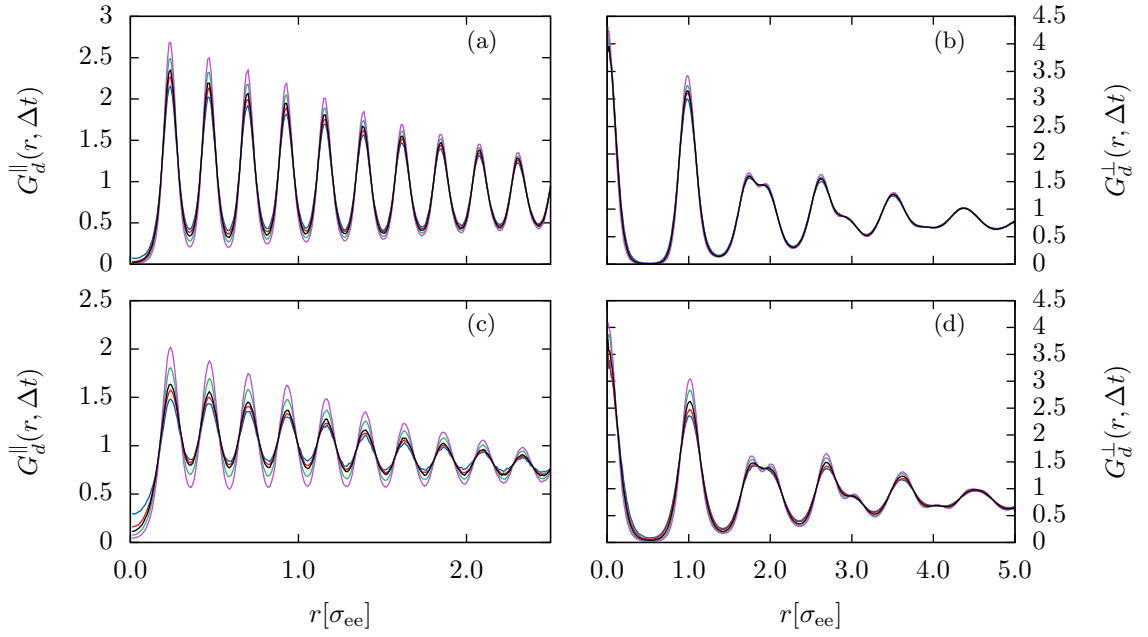


Figure 3.19: Parallel DVHF (a) and (c), perpendicular DVHF (b) and (d). All panels at $P^* = 50$, **Top panels:** $T^* = 6.00$ - **bottom panels:** $T^* = 6.70$. The colours purple, green, black, red and blue correspond to curves for time intervals Δt^* equal to 2.5, 5, 10, 20 and 80, respectively.

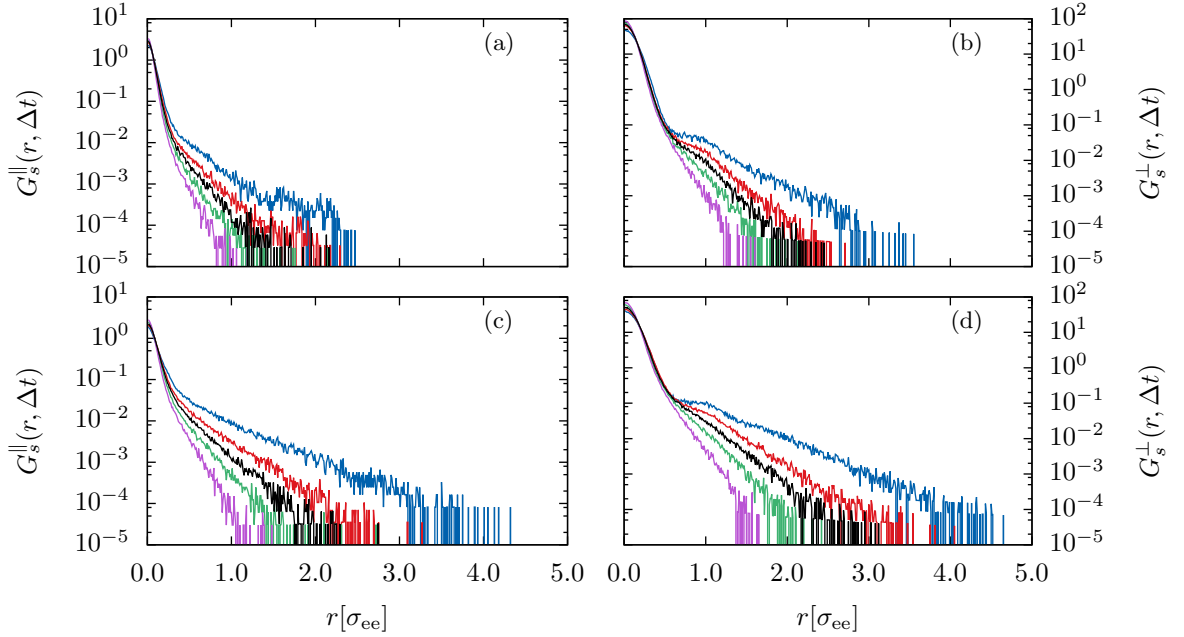


Figure 3.20: Parallel SVHF in (a) and (c), perpendicular SVHF in (b) and (d). $P^* = 50$, **Top:** $T^* = 6.00$ - **bottom:** $T^* = 6.70$. The colours purple, green, black, red and blue correspond to curves for time intervals Δt^* equal to 2.5, 5, 10, 20 and 80, respectively.

only slightly below the transition temperature T_{ICol} of the bulk system. As indicated by the vanishing S_A parameter, the domain's nematic director aligns perpendicular to the pore axis (Fig. 3.22). This behaviour can be verified by snapshots of the system.

The RDF in Fig. 3.23 clearly shows evidence of a crystal phase at the lowest temperature of $T^* = 6$

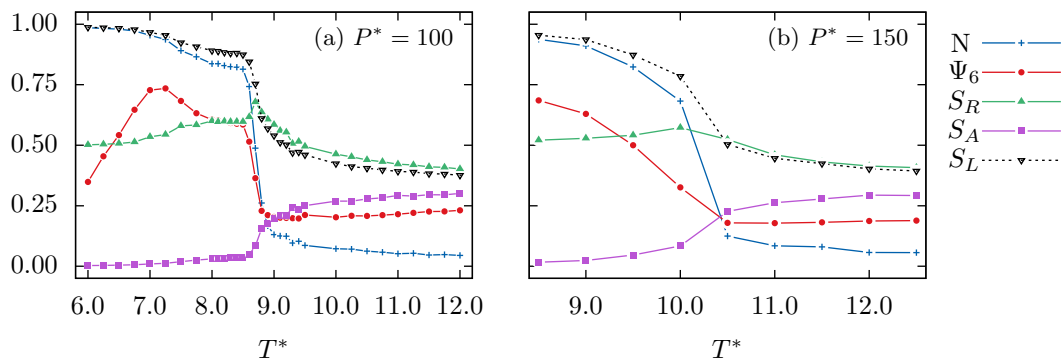


Figure 3.21: Temperature dependence of the nematic S (blue), local nematic S_L (black), radial nematic S_R (green), axial nematic S_A (purple) and hexagonal Ψ_6 (red) order parameters for different pressures.

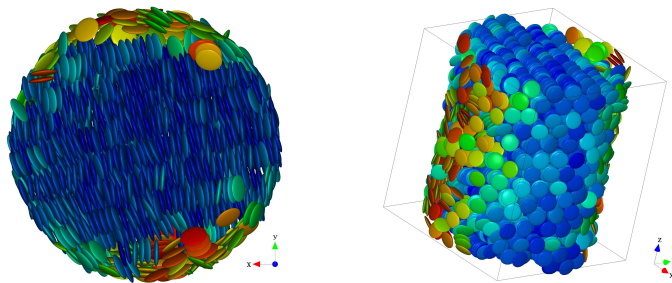


Figure 3.22: Snapshots at $P^* = 100$, $T^* = 8.00$. The pore diameter is $10 \sigma_{ee}$

and a hexagonal columnar phase at $T^* = 7.25$. For the maximum of the S_R it shows a fluid like behaviour, that can also be seen in the corresponding parts of the DVH in Fig. 3.24.

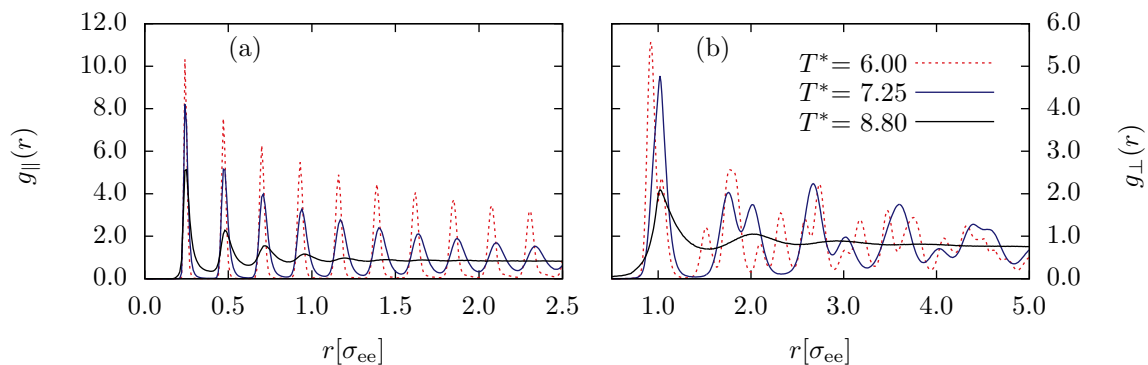


Figure 3.23: (a) Parallel and (b) perpendicular part of the RDF at $P^* = 100$, for the temperatures at the maxima of S_R and Ψ_6 and in the crystal phase.

We also study different order parameters in cylindrical shells, coaxial with the nanopore, to fully characterise the structure of the discotic liquid crystal. Figures 3.25 and 3.26 also show interesting behaviour. The pore centre is almost not affected by the nanoconfinement, showing a developing of the local nematic order and hexagonal order parameter similar to the bulk system, therefore discontinuous. The layer close to the wall shows a radial nematic state over a large region. The plateau in the global hexagonal order parameter shown in Fig. 3.21(a) therefore arises from the

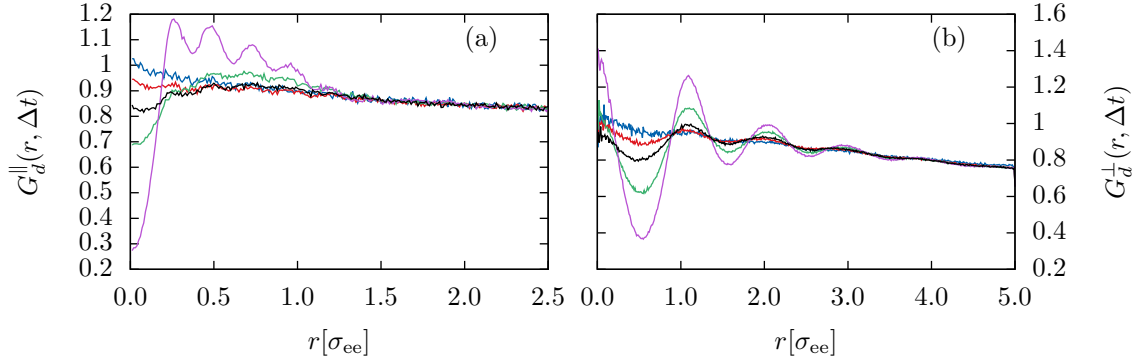


Figure 3.24: Parallel DVHF (a) , perpendicular DVHF (b), $P^* = 100$ $T^* = 8.80$. The coloured curves purple, green, black, red and blue correspond to time intervals Δt^* equal to 1.25, 5, 10, 20 and 80, respectively.

superposition of the different behaviours of Ψ_6 in the pore centre and the outer layers. The system first contains a columnar domain in the centre, which then absorbs particles from the adjacent, i.e. outer regions of the pore.

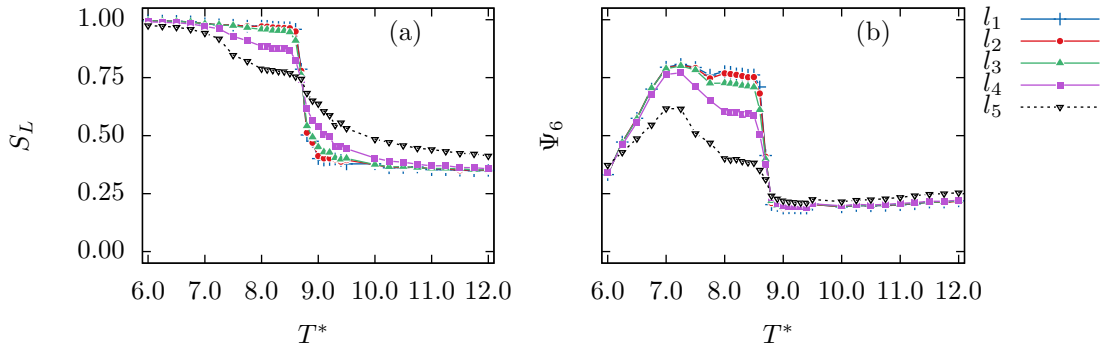


Figure 3.25: Local nematic (a) and hexagonal (b) order parameters for different layers l_i around the pore centre as a function of temperature at $P^* = 100$. The blue curve titled “ l_1 ” shows the central cylindrical shell of radius σ_{ee} , the other curves correspond to layers of thickness σ_{ee} , numbered from the inside to the outside.

At $P^* = 150$, we can still observe the same behaviour as at $P^* = 100$, although with a weaker peak in the S_R . Furthermore, a remarkable jump in the different nematic order parameters can not be seen. This kind of behaviour occurs for all pressures from $P^* = 75$ up to $P^* = 200$. Before forming a columnar domain similar to the one in Fig. 3.22, there is a radial nematic region. But the higher the pressure is, the smaller and weaker the occurring order is.

Furthermore, 3.15(b) shows that the one domain grows with decreasing temperature, since S approaches 1. Also, a completely hexagonal columnar phase forms, where all order parameters change continuously.

Finally, the system loses its D_{6h} again, indicating the transition into the crystalline phase, Ψ_6 thereby decreases to much smaller values than in bulk. The crystal orients with the director perpendicular to the pore axis.

Alignment along the pore axis - In Fig. 3.27 we see that at pressure $P = 225$ the S_R and S_A are equal in the isotropic state. Following S from high to low T , we see the formation of a

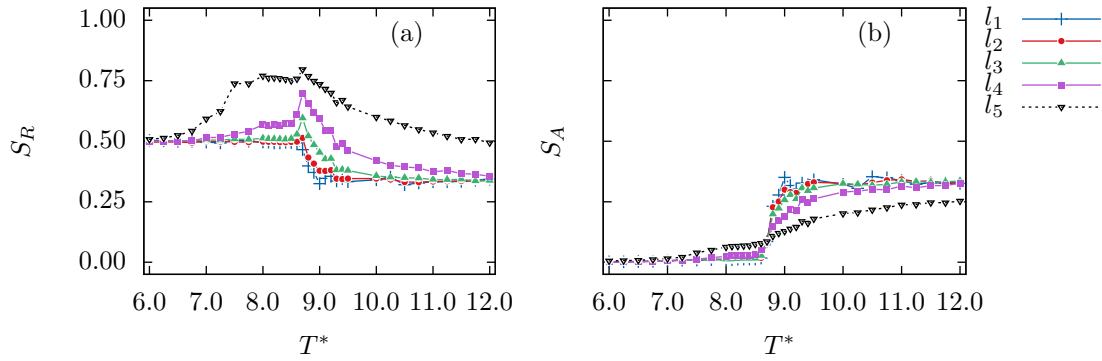


Figure 3.26: Radial (a) and Axial (b) nematic order for different distances from the pore centre as a function of temperature at $P^*=100$. Labelling follows the same scheme as in Fig. 3.25.

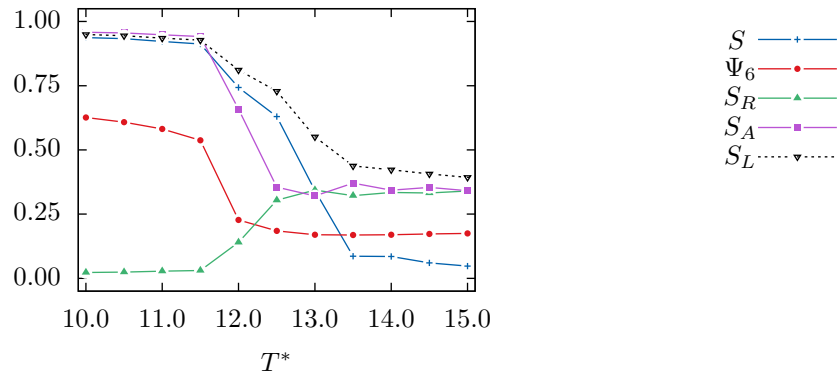


Figure 3.27: Temperature dependence of the nematic S (blue), local nematic S_L (black), radial nematic S_R (green), axial nematic S_A (purple) and hexagonal Ψ_6 (red) order parameters for $P = 255$.

nematic phase at $T^* = 12.5$, which aligns with the nematic director parallel to the pore axis in the next temperature step $T^* = 12$; the overall alignment is indicated by the S_A . Compared to the bulk system, this onset of the orientational correlation is shifted to lower temperatures by approximately one reduced temperature unit. The behaviour of the nematic phase, that develops without a delay in the S_A indicates a destabilisation of the nematic phase by the opposing face-on wall anchoring and the induced symmetry. The symmetry of the nanoconfinement has a stronger effect at higher pressure. The system at $P = 225$ quickly develops a columnar phase, also with columns along the pore axis, as indicated by the S_A which rises to values of approximately 1. The increase in Ψ_6 thereby takes place at almost the same temperature as in the bulk system. The transition is though differing in its continuous fashion.

3.2.1.2 Pore Diameter $5\sigma_{ee}$

For the smaller pore size, there is no new behaviour. The radial poly-domain face-on configuration, present in the larger pore at $P^* = 25$ and $P^* = 50$, disappeared. The face-on columnar configuration, which has been extensively addressed above, is now present at all pressures below $P^* = 200$, while the orientation of the nematic director parallel to the pore axis already occurs at $P^* = 200$. The decrease of Ψ_6 in Figs. 3.28 (b) and (c) at $T \leq 6.5$ is accompanied by an increase in the nematic order parameter, indicating the transition into the crystal phase. The most apparent difference from behaviour in the thicker pore is that at both pressures $P^* = 100$ (Fig. 3.28(b)) and $P^* = 175$ (Fig. 3.28(c)), the transition to nematic is more discontinuous and a global nematic order is present without a plateau after the transition from the isotropic into an aligned phase.

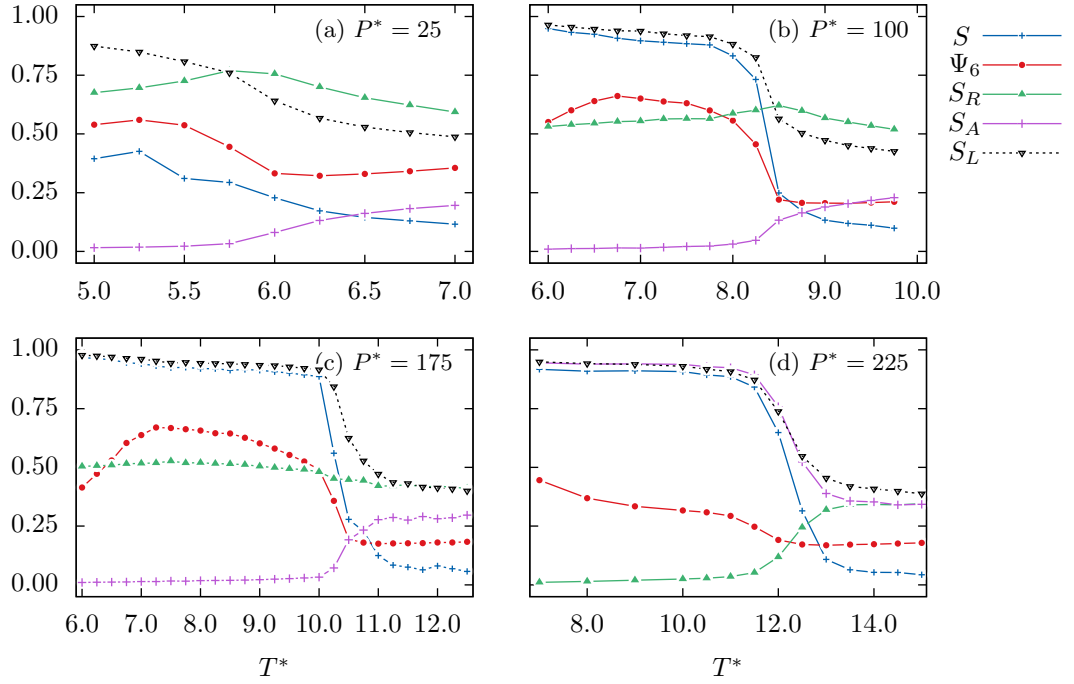


Figure 3.28: Temperature dependence of the nematic S (blue), local nematic S_L (black), radial nematic S_R (green), axial nematic S_A (purple) and hexagonal Ψ_6 (red) order parameters for different pressures.

Also the maximum of the hexagonal order parameter at $P^* = 100$ (Fig. 3.28(b)) is smaller than the one in the system in the thicker pore, probably due to the stronger spatial restrictions. Like the nematic order parameter, the hexagonal order parameter does not exhibit a plateau.

The absence of the plateau in Ψ_6 at $P^* = 100$ is caused by the system developing more as a whole in the thinner pore. Figure 3.29 shows that the local nematic ordering starts at the outer layer and is more continuous there. Although the degree of order reflected by S_L and Ψ_6 is still different in strength, it develops in the same fashion.

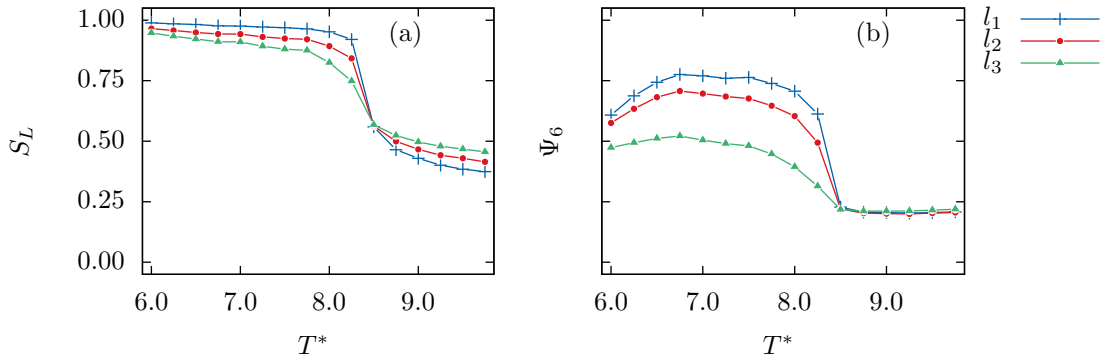


Figure 3.29: Local nematic (a) and hexagonal (b) order parameters for different layers l_i around the pore centre as a function of temperature at $P^* = 100$. The blue curve titled “1” shows the central cylindrical shell of radius σ_{ee} , the other curves correspond to layers of thickness σ_{ee} , numbered from the inside to the outside.

The form of the curve for S_R in Fig. 3.28(a) suggests a face-on mono-domain columnar configuration at $P^* = 25$, but the parameter remains larger than the value of $S_R = 0.5$ that was observed for this configuration before. The snapshot of the system in Fig. 3.30 reveals that it is somewhere between the mono and poly-domain face on columnar configuration. The configuration is stable and already transforms into a crystal at $T^* = 5.0$, given that the hexagonal order parameter starts decreasing.

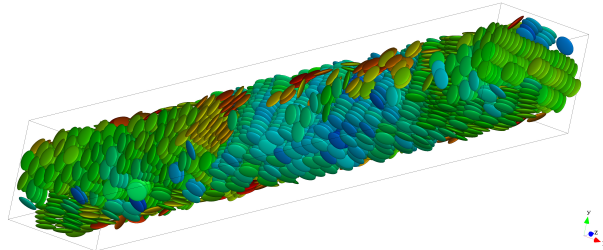


Figure 3.30: Snapshot of the confined discotic liquid crystal system at $P^* = 25$, $T^* = 5.00$. The pore diameter is $5\sigma_{ee}$

Another interesting new behaviour is the low D_{6h} symmetry after the transition in a phase with high nematic order at pressures $P^* = 200$ and $P^* = 225$ (Fig. 3.28(d)). The bulk counterpart exhibits a nematic and a hexagonal columnar phase under these conditions. At the high pressure, the different symmetry of the pore hinders the formation of a hexagonal columnar phase (see Fig. 3.31). The orientation of columns along the pore axis is important for this phenomenon, although the phenomenon is also present for the face-on mono-domain configuration. Similar behaviour, i.e. a plateau at low hexagonal symmetry when columns align along the pore axis, has also been reported by Busselez *et. al.*[18].

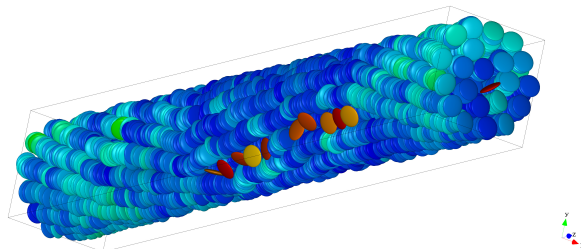


Figure 3.31: Snapshot of the confined discotic liquid crystal system at $P^* = 225$, $T^* = 9.00$. The pore diameter is $5\sigma_{ee}$

For the case of alignment of columns parallel to the pore axis, a modified DVHF has been computed. According to [18] I took the directions relative to the pore axis instead of the particle orientation vector. The confinement DVHF (Fig. 3.39) reveals columnar phases for both the higher and lower regime of Ψ_6 , according to the fluid-like decay of structural correlation over time in the direction parallel to the pore axis.

The columnar phase at the lower pressure exhibits slower dynamics, shown by the slower decay of correlation along the pore, i.e. column axes. On the contrary, it exhibits much sharper peaks in the confinement RDF that indicate the presence of a hexagonal arrangement of columns.

The parallel part of the confinement RDF has two length scales of the decay of the heights of peaks, one fast at the beginning and one slow at bigger distances. This could be because of the tilt and twist visible in Fig. 3.31.

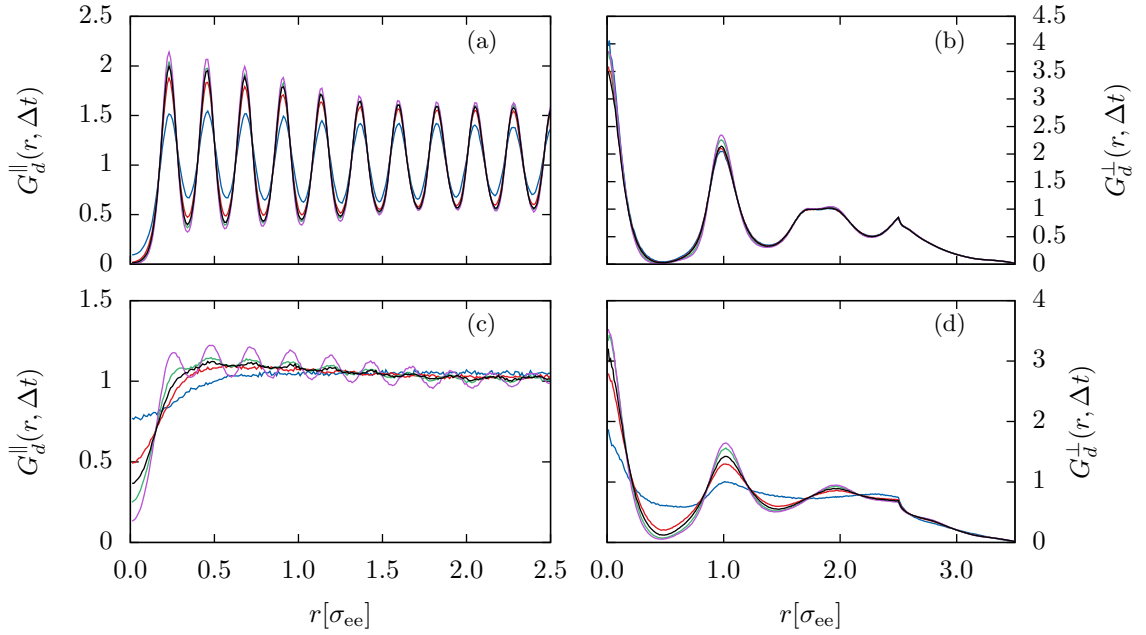


Figure 3.32: Confinement parallel DVHF (a) and (c), perpendicular DVHF (b) and (d). All panels at $P^* = 225$, **Top panels:** $T^* = 7.00$ - **bottom panels:** $T^* = 10.00$. The colours purple, green, black, red and blue correspond to curves for time intervals Δt^* equal to 2.5, 5, 10, 20 and 80, respectively.

Figures 3.39(b) and (d) reveal that the system is stable in the direction perpendicular to the pore axis for long times, but the blue curve representing the longest time interval shows that the lateral arrangement of the columns in the pore can change on long time scales. This changing of the structure disappears at $T^* = 9.00$.

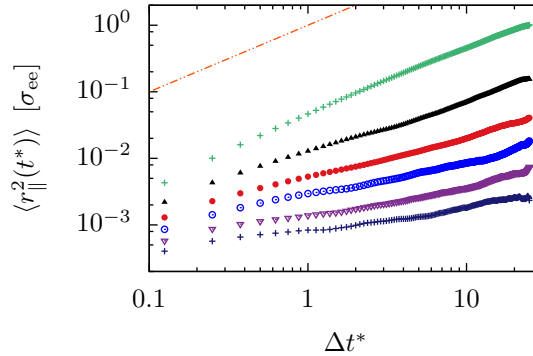


Figure 3.33: Mean square displacement parallel to the molecular orientation vector for $P^* = 225$. Blue crosses for $T^* = 7.00$, purple triangles for $T^* = 8.00$, empty yellow circles $T^* = 9.00$, red dots $T^* = 10.00$, black pyramids $T^* = 11.00$ and green crosses for $T^* = 12.00$. The grey line has the slope characteristic for the diffusive regime.

Further remarkably is that the system begins to exhibit an increase in Ψ_6 when the bulk system crystallises. The question arises how this trend ends. The MSD along the molecular director shows a slowing down of dynamics over the whole range of present columnar configuration. At the lowest $T^* = 7.0$, particles still move roughly 10% of their thickness.

3.2.1.3 Pore Diameter $3\sigma_{ee}$

In the thinnest pore, also the face-on mono-domain columnar phase gets a twist, resulting in a decrease of nematic order. In Fig. 3.34(c) this causes a plateau in Ψ_6 upon cooling, while in Fig. 3.34(a) this twist occurs after the rising of Ψ_6 to a value characteristic of a well ordered hexagonal columnar phase.

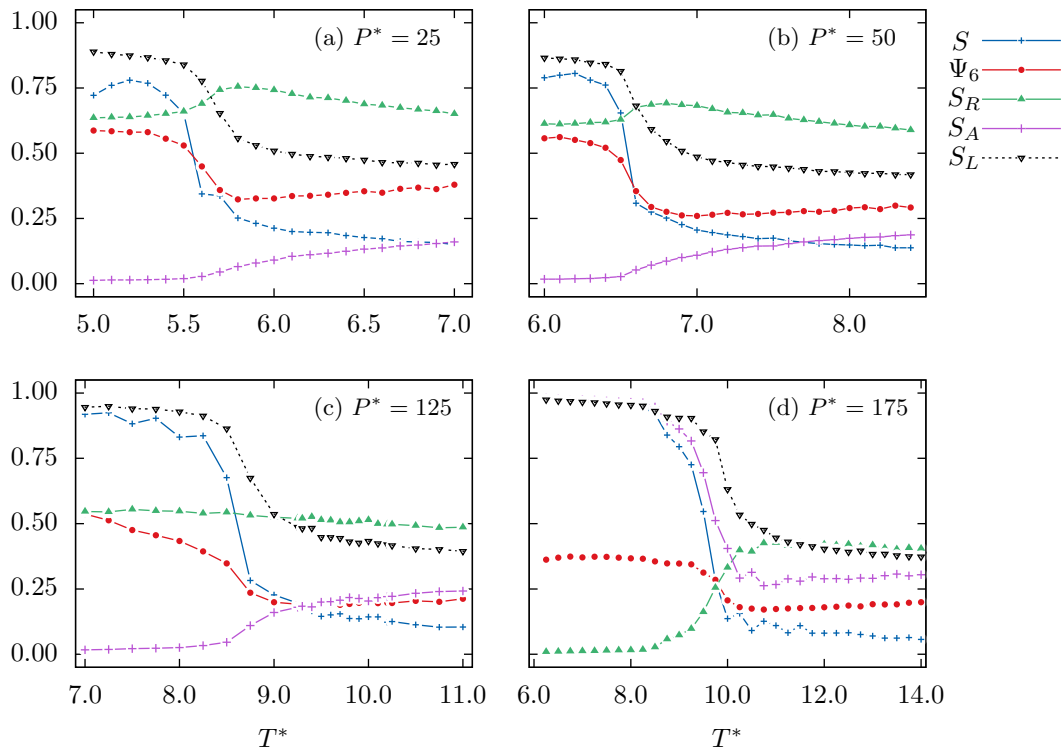


Figure 3.34: Temperature dependence of the nematic S (blue), local nematic S_L (black), radial nematic S_R (green), axial nematic S_A (purple) and hexagonal Ψ_6 (red) order parameters for different pressures.

The twist, indicated by the low global nematic order, shows that the nematic order, i.e. fluid-fluid force anisotropy, loses its dominance. Looking back at Fig. 3.28(b) this also explains the low global nematic order at $P^* = 100$ between $T^* = 7.75 - 6.75$.

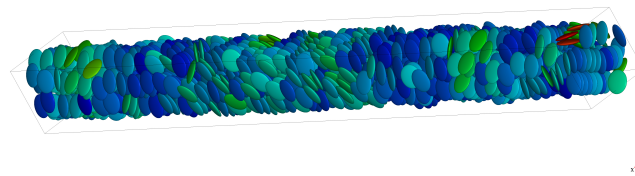


Figure 3.35: Snapshot of the confined discotic liquid crystal system at $P^* = 125$, $T^* = 7.00$. The pore diameter is $3\sigma_{ee}$

When columns begin aligning parallel to the pore axis at $P^* = 175$, the system exhibits fluid like behaviour along the columns clearly below the bulk's crystallisation point, c.f. 3.36(a).

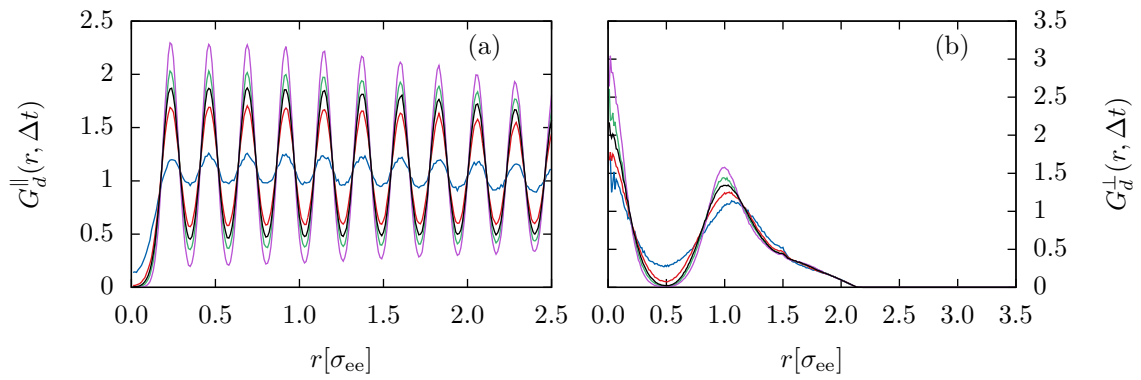


Figure 3.36: Parallel DVHF (a) and (c), perpendicular DVHF (b) and (d), $P^* = 175$ $T^* = 6.25$. The colours purple, green, black, red and blue correspond to curves for time intervals Δt^* equal to 1.25, 5, 10, 20 and 80, respectively

3.2.2 Edge-on Anchoring

3.2.2.1 Pore Diameter $10\sigma_{ee}$

Also the system with edge-on wall anchoring shows continuous phase transitions. The isotropic phase shows the opposite behaviour of its counterpart influenced by face-on wall anchoring.

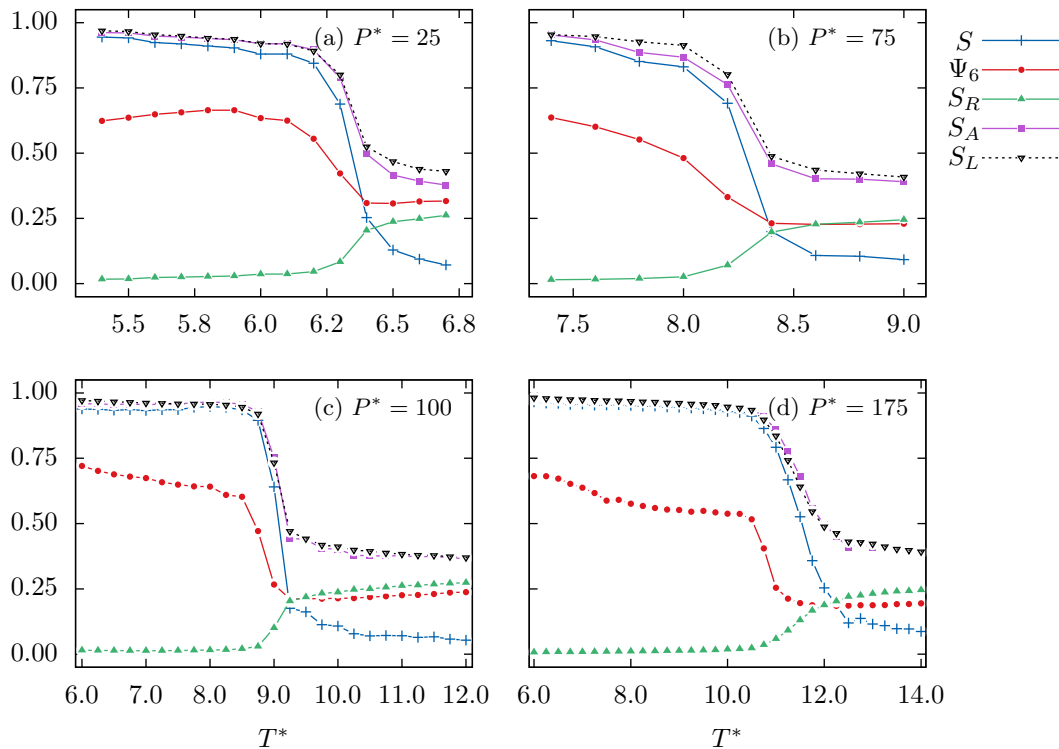


Figure 3.37: Temperature dependence of the nematic S (blue), local nematic S_L (black), radial nematic S_R (green), axial nematic S_A (purple) and hexagonal Ψ_6 (red) order parameters for different pressures.

The orientation of the particle director parallel to the pore axis is preferred, as indicated by the S_A , see Fig. 3.37. Upon cooling, after the transition into a mostly hexagonal columnar phase, the system enters a region with nearly constant nematic and hexagonal order parameters, e.g. Fig. 3.37(d) between $T^* = 8$ and $T^* = 10$. Upon further cooling the hexagonal order parameter increases again, accompanied with a slight decrease in the nematic order parameter (visible in the panel (c) of Fig. 3.37) for pressures higher than $P^* = 75$.

The spatially resolved developing of the local nematic order and hexagonal order parameter (Fig. 3.38) does not show a reason for that. Nevertheless it shows that, for this thickness of the pore, almost only the outer layer is influenced by the confinement, so that its phase behaviour deviates from the other regions.

In the region of the plateau of Ψ_6 after the the first increase, the liquid crystal exhibits properties of a columnar phase, as we can see at $P^* = 175$. In Fig. 3.39(c) and (d) we can see fluid like behaviour in the direction parallel to the pore axis. In the perpendicular direction there is a stable lattice which only foreshadows a hexagonal lattice. Panel (b) indicates a more hexagonal columnar phase at the corresponding lower temperature, panel (a) reveals that the dynamics along the column axes are slower though. The bulk system, for comparison, already transforms into a crystal at

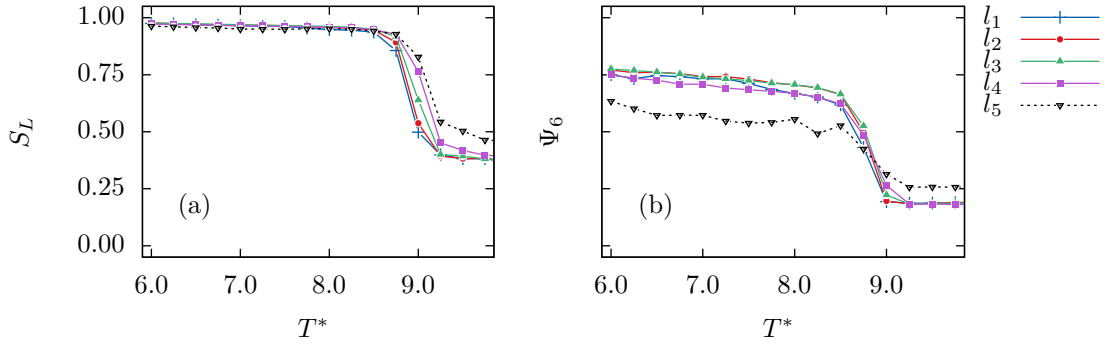


Figure 3.38: Local nematic (a) and hexagonal (b) order parameters for different layers l_i around the pore centre as a function of temperature at $P^* = 100$. The blue curve titled “ l_1 ” shows the central cylindrical shell of radius σ_{ee} , the other curves correspond to layers of thickness σ_{ee} , numbered from the inside to the outside.

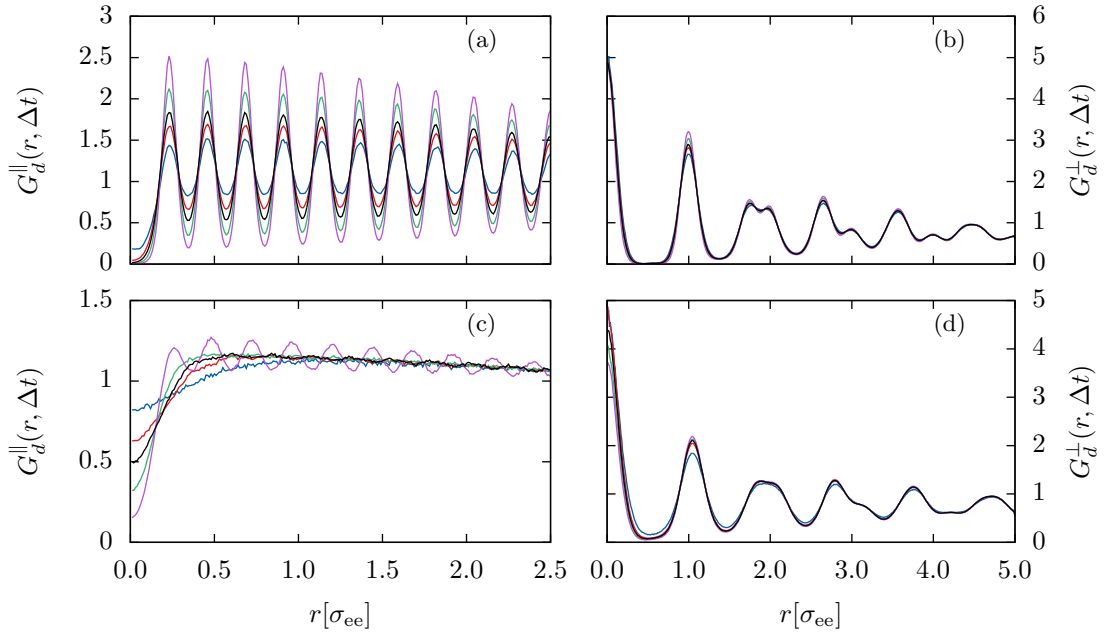


Figure 3.39: Confinement parallel DVHF (a) and (c), perpendicular DVHF (b) and (d). All panels at $P^* = 175$, **Top panels:** $T^* = 6.00$ - **bottom panels:** $T^* = 10.00$. The colours purple, green, black, red and blue correspond to curves for time intervals Δt^* equal to 2.5, 5, 10, 20 and 80, respectively.

$T^* = 7.8$. Also at the other pressures, the system remains in a columnar phase clearly below the crystallisation point of the bulk system, indicating geometrical frustration. The occurring of any hexagonal order, which always accompanies the transition into a columnar phase, remains at the same temperature. Only nematic order is developed at slightly warmer temperatures.

3.2.2.2 Pore Diameter $5\sigma_{ee}$

As shown in Fig. 3.40 the plateaus of Ψ_6 after the transition into an aligned phase are also present for the pore diameter of $5\sigma_{ee}$, being even stronger there. The behaviour responsible for this two

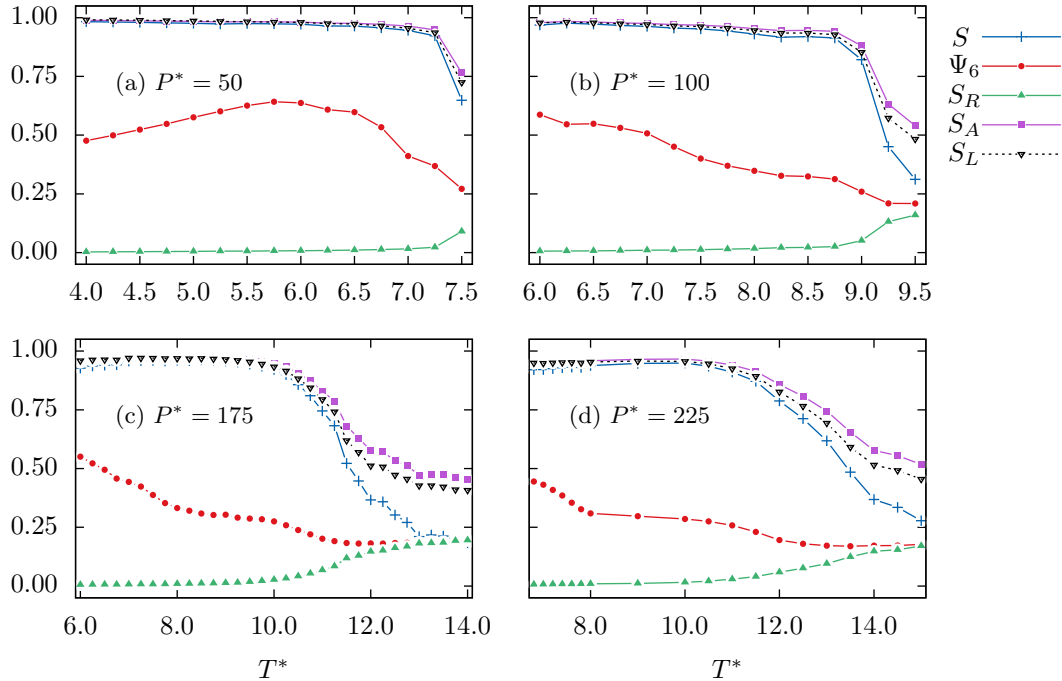


Figure 3.40: Temperature dependence of the nematic S (blue), local nematic S_L (black), radial nematic S_R (green), axial nematic S_A (purple) and hexagonal Ψ_6 (red) order parameters for different pressures.

regimes can be seen in snapshots of the thinner pore in Figs. 3.46 and 3.41. There are two regimes present in the columnar phase.

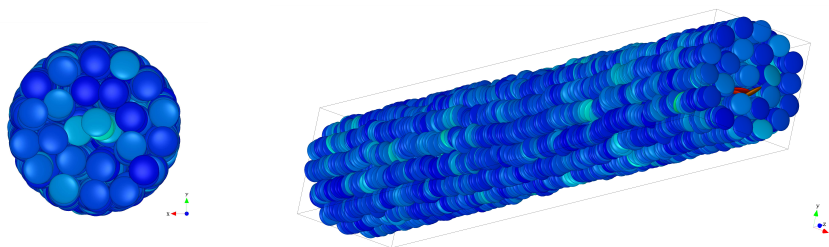


Figure 3.41: First columnar regime where the induced symmetry is dominant. Snapshots at $P^* = 175$, $T^* = 9.00$. The pore diameter is $5\sigma_{ee}$

In the first (Fig. 3.41), the lateral arrangement of columns is dominated by the confinement-induced symmetry. In fact, we can see that the effect gets stronger with increasing pressure, because the plateau in Ψ_6 grows.

In the second regime (Fig. 3.46) the fluid-fluid interaction beats the induced symmetry, causing the developing of a hexagonal columnar phase in the centre of the pore. But the hexagonal lattice does not fit into the cylinder, so that it becomes twisted and tilted, which is the reason for the

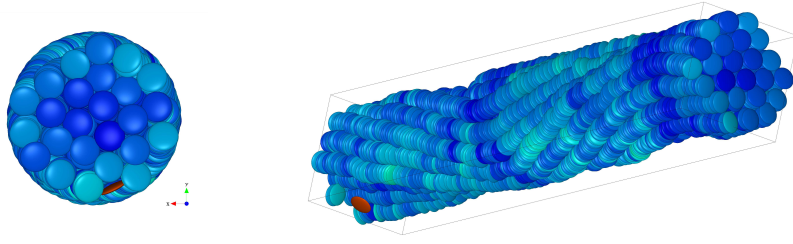


Figure 3.42: Second columnar regime in which the fluid-fluid interaction dominates the lateral arrangement of the columns. Snapshots at $P^* = 175$, $T^* = 6.00$. The pore diameter is $5\sigma_{ee}$

decrease in the global nematic order. For $P^* = 50$ in the thinner pore, i.e. $d = 5\sigma_{ee}$ (Fig. 3.40) and $P^* = 25$ in the thicker, i.e. $d = 10\sigma_{ee}$ (Fig. 3.37) this does not occur, the global nematic order rather increases as Ψ_6 increases, similarly to the behaviour in the bulk system. This indicates that the twist and tilt is caused by the high pressure.

The two columnar regimes differ in the decay of correlation in the confined DVHF along the pore axis. Comparison of Fig. 3.43(a) and 3.44(a) suggests that this has also to do with the tilting of columns in the $P^* = 175$ configuration, hindering collective columnar motion, because the configuration at $P^* = 100$ only differs in a higher global orientational order, indicating less tilt.

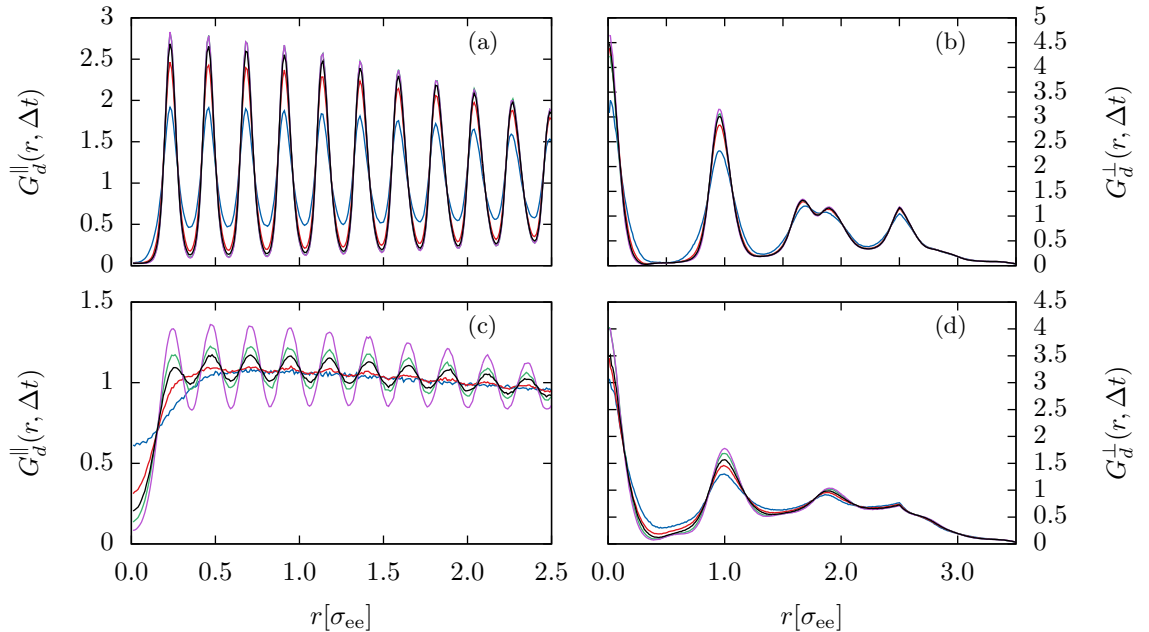


Figure 3.43: Parallel DVHF (a) and (c), perpendicular DVHF (b) and (d). All panels at $P^* = 175$, **Top panels:** $T^* = 6.00$ - **bottom panels:** $T^* = 9.00$. The colours purple, green, black, red and blue correspond to curves at time intervals Δt^* equal to 2.5, 5, 10, 20 and 80, respectively.

The non-tilted configuration at $P^* = 100$ shows more dynamics in the direction along the pore axis, i.e. column axes. But the dynamics shown in 3.43(a) will also be that slow because of the low temperature.

As a conclusion, the whole continuous transition between $T^* = 11.0$ and $T^* = 6.0$ at $P^* = 175$ can be described as follows. The liquid crystal continuously transforms from the nematic in a columnar phase, while the hexagonal arrangement of columns first occurs in the pore centre (cf. Fig. 3.45). Around $T^* = 10.0$ we find columns extended over the whole system close to the walls. The centre

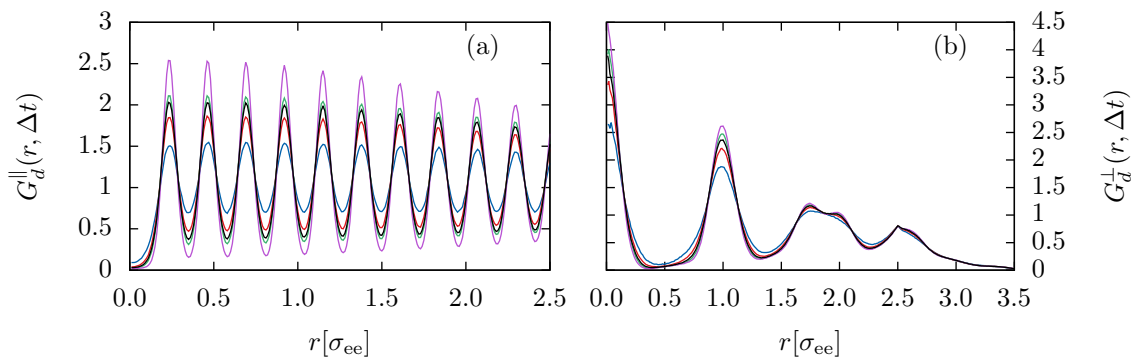


Figure 3.44: Parallel DVHF on the left, perpendicular DVHF on the right, $P^* = 100$ $T^* = 6.25$. The colours purple, green, black, red and blue correspond to curves for time intervals Δt^* equal to 1.25, 5, 10, 20 and 80, respectively

still shows slightly isotropic behaviour (cf. Fig. 3.46).

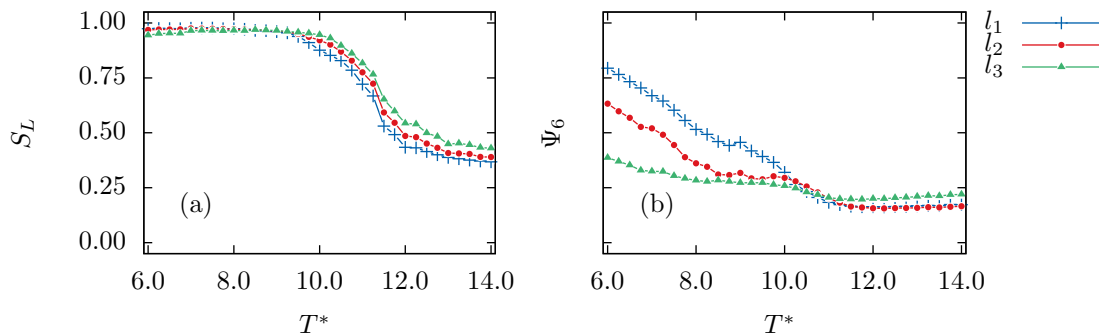


Figure 3.45: Local nematic (a) and hexagonal (b) order parameters for different layers l_i around the pore centre as a function of temperature at $P^* = 100$. The blue curve titled “ l_1 ” shows the central cylindrical shell of radius σ_{ee} , the other curves correspond to layers of thickness σ_{ee} , numbered from the inside to the outside.

The hexagonal lateral arrangement of columns first develops in the centre, then at $T^* = 9.0$ also in the middle layer. The outer layer only shows low hexagonal order, developing under $T^* = 7.5$. This could also arise from the deformation of columns only occurring in the outer layer.

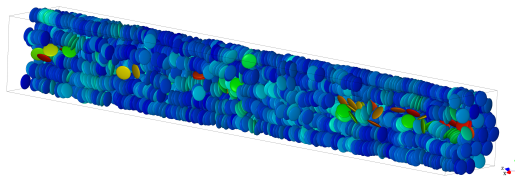


Figure 3.46: Snapshot of the confined discotic liquid crystal system at $P^* = 175$, $T^* = 10.00$. There is less nematic order in the core. The configuration is cut parallel to the pore axis to make the centre visible. The pore diameter is $5\sigma_{ee}$

A weakly isotropic core can also be found for the pressures above $P^* = 175$.

At $P^* = 50$, the system ends up in the crystal phase, as shown by the DVHF (Fig. 3.47). All the other cooling runs ended in a columnar phase.

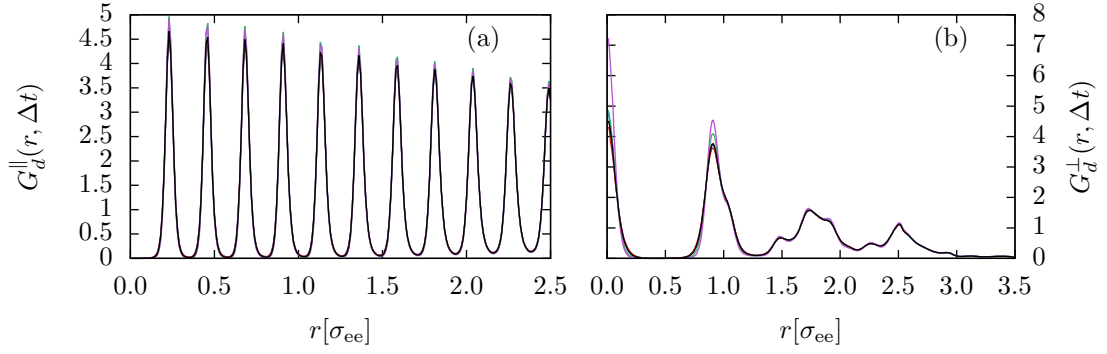


Figure 3.47: Parallel DVHF (a), perpendicular DVHF (b) at $P^* = 50$ $T^* = 4.00$. The colours purple, green, black, red and blue correspond to curves for time intervals Δt^* equal to 1.25, 5, 10, 20 and 80, respectively.

3.2.2.3 Pore Diameter $3\sigma_{ee}$

For the smallest pore diameter, the confinement-induced symmetry becomes even more noticeable. Already at $P^* = 25$, two columnar regimes are present. At the higher pressures shown in Fig. 3.48(b) and (c), the liquid crystal columns are prevented from arranging in hexagonal lattice clearly below the corresponding bulk's crystallisation point.

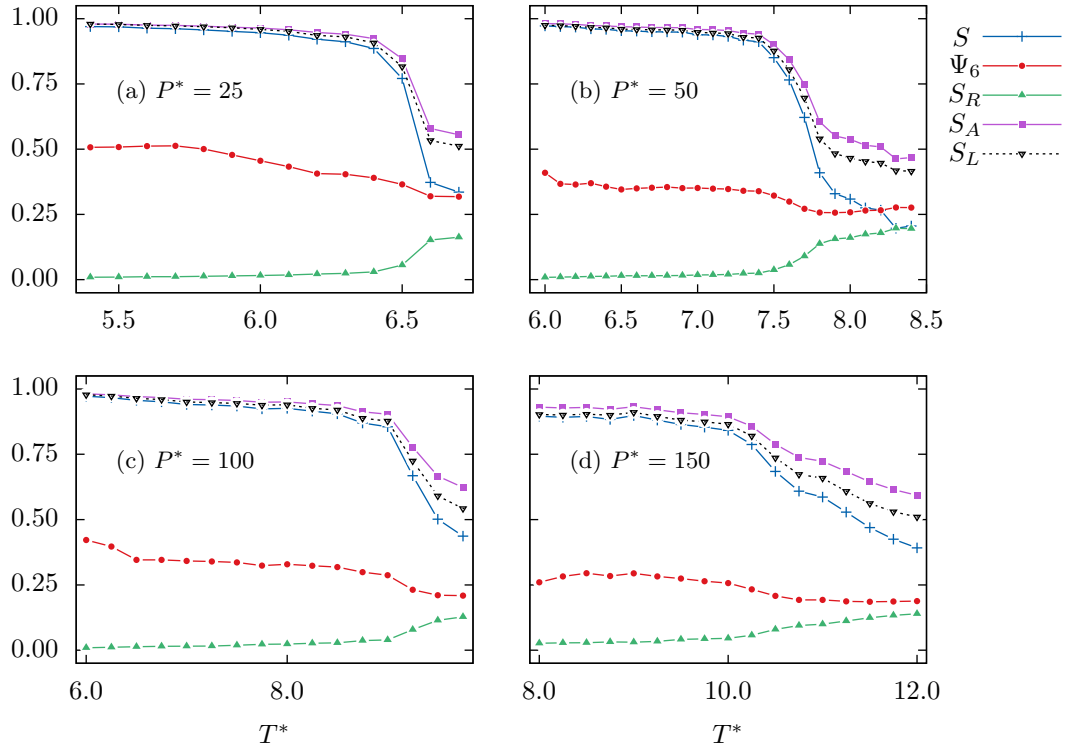


Figure 3.48: Temperature dependence of the nematic S (blue), local nematic S_L (black), radial nematic S_R (green), axial nematic S_A (purple) and hexagonal Ψ_6 (red) order parameters for different pressures.

Moreover, above and at $P^* = 150$ the system does not seem to develop a hexagonal columnar

phase at all.

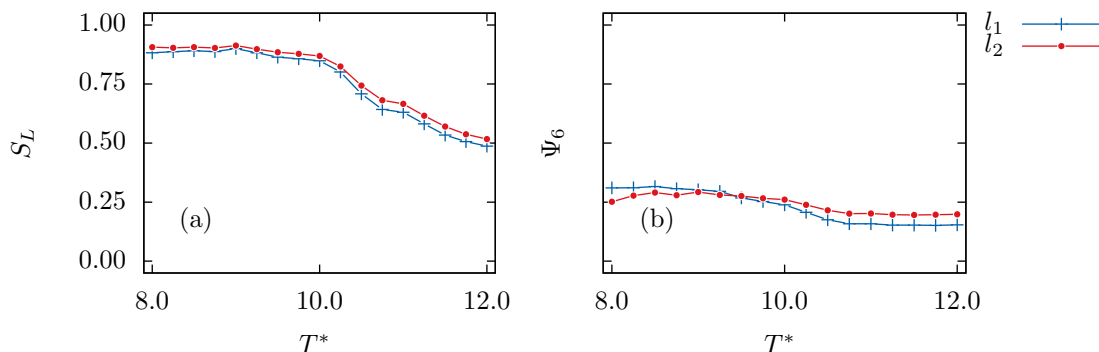


Figure 3.49: Local nematic (a) and hexagonal (b) order parameters for different layers l_i around the pore centre as a function of temperature at $P^* = 150$. The blue curve titled “ l_1 ” shows the central cylindrical shell of radius σ_{ee} , the other curves correspond to layers of thickness σ_{ee} , numbered from the inside to the outside.

Also the thinnest pore reveals an isotropic core, as indicated by the lower local nematic order in the centre. This is difficult to see in Fig. 3.49, on the one hand there is still orientational correlation, and on the other hand, the local nematic order is always quite high. This is because of the high force anisotropy of the fluid-fluid interaction model.

3.3 Discussion

We saw that the strength of the fluid-wall interaction also had a huge effect on the phase behaviour. Interaction energies weaker than the chosen one yield columns tilted with respect to the pore axis. This shows the competition between the tendency of the fluid to form long columns and the anchoring at the wall favouring their orientation in the radial direction.

For large large values of the fluid-wall interaction energy orientation parallel to the radial direction becomes dominant but strong geometrical frustration of the columnar phase is observed. However, the frustration is though varying over the pore’s radial direction.

For calamitic liquid crystals confined in a channel an escaped radial configuration, i.e. radially ordered rim and the core’s nematic director along the pore axis, has been experimentally observed [28, 29]. We do not see this configuration for our choice of model parameters. So, for the present setup a fluid-wall interaction strength stronger than the chosen value could be promising to yield similar configurations for discotics.

Our simulations agree with the experimental finding of face-on columnar phases, both mono-domain and poly-domain [20]. However, in our simulations the mono-domain configuration is dominant. We ascribe that to the flat, idealised wall surfaces. A rough surface would play an important role by allowing different locally ordered domains to grow [20].

Chapter 4: Conclusions

4.1 Face-on Anchoring

We have seen that the face-on anchoring wall interaction has a strong effect on the phase diagram. In the largest pore of diameter $10\sigma_{ee}$ the induced symmetry of the confinement is present but comparatively weak. At low pressure, i.e. up to $P^* = 50$, it allows the system to develop the radial symmetric phases, that are imposed by the wall anchoring, in a stable fashion. The system exhibits a radially aligned nematic phase and also a hexagonal columnar phase, with a large number of radially oriented domains. The radial alignment thereby extends over the whole pore radius. The phase transitions are continuous in contrast to the bulk system, but the insets of the transition roughly remain at the same temperature.

At higher pressures e.g. $P^* = 100$, the system is forced to adopt the geometry of the pore. The face-on anchoring wall interaction though is still comparatively strong enough to yield face-on columnar configurations. Right after the transition into an orientational ordered phase, a preferred global orientation is present. Spatially resolved radial and local nematic order indicate the nucleation of columns at the outer layer. At the bulk's T_{ICol}^- the centre then develops into columnar phase. Locally, this transition is similar to the bulk's developing. The centre thereat exhibits more hexagonal symmetry, due to the spatial restrictions. Upon further cooling, the domain then absorbs more and more particles, those close to the wall at last.

At the same temperature as the bulk system, hexagonal symmetry begins to decrease. This is the crystallisation point, as can be confirmed from inspecting the DVHF. The transition passes over a smaller range of temperature thereby.

At $P^* = 225$ the competing effects of the face-on anchoring and the symmetry become visible. The T_{IN}^- transition temperature is shifted to cooler temperatures. Concerning the columnar phase, the cylindrical geometry imposes an alignment parallel to the pore axis on the columns. The confinement is though not small enough to prohibit the hexagonal lateral arrangement between the columns.

In the pore with diameter $5\sigma_{ee}$ the radial columnar alignment is shifted to $P^* = 25$ or lower. Different columnar domains are present, the most of them extends over the whole pore diameter. At intermediate temperatures the columnar region in the phase diagram is represented in a mono-domain face-on configuration with less D_{6h} symmetry than the bulk system and the system confined in the $d = 10\sigma_{ee}$ pore. The transition into the columnar phase is thereby shifted about one reduced unit to cooler temperatures and a nematic phase suppressed. Additionally the crystallisation point is also shifted to lower temperature at higher pressure, i.e. $P^* = 175$.

The low D_{6h} is caused by the strongly imposed $D_{\infty h}$ symmetry of the pore, but as temperature get lower, the symmetry D_{6h} gets higher. The effect is strongest at high pressure i.e. $P^* = 225$, where columns align parallel to the pore axis. There the system does not exhibit remarkable hexagonal symmetry until getting close to the bulk's crystallisation point. Geometrical frustration prohibits crystallisation down to the lowest observed temperature $T^* = 7.0$, that is 1 reduced unit below the bulk's crystallisation point.

In the thinnest pore with diameter $3\sigma_{ee}$ only the radial mono-domain columnar configuration at lower pressure and parallel axial columnar configuration occur. At low pressure, columns expanding over the whole diameter are developed, but weakly correlated, so that a random twist in their orientation occurs along the pore axis. When the induced symmetry forces columns to align parallel to the pore axis, geometrical frustration hinders crystallisation even stronger.

4.2 Edge-on Anchoring

The simulations with edge-on anchoring always yield alignment of columns parallel to the pore axis. The thickest pore enlarges the columnar region for all pressures by shifting the crystallisation point to lower temperatures. For low pressures, we can observe the hexagonal order decreasing after reaching a maximum. The transition into a crystal was only observed at $P^* = 50$, due to the large shift of the transition line in the phase diagram. The crystallisation is continuous and shifted about 2 reduced units to cooler temperature.

At pressure $P^* = 100$ the columnar phase splits into two regimes. First the $D_{\infty h}$ symmetry of the pore dominates at the higher temperature end of the region. The D_{6h} symmetry of the liquid crystal dominates at the lower temperature part of the region. While the centre of the pore is only weakly affected, mostly the layer at the wall exhibits reduced hexagonal symmetry. As pressure increases the hexagonal symmetry is also lowered in the centre.

In the $d = 5\sigma_{ee}$ pore the model exhibits behaviour similar to the thicker pore at pressures up to $P^* = 50$, the columnar region is enlarged mostly by geometric frustration of the crystal phase.

At higher pressures, the continuous transition into an orientational correlated configurations expands over a range of two reduced temperature units, much more spread than observed before. The columnar phase again shows two different arrangements of columns, as described above. At pressure $P^* = 175$ and temperature $T \gtrsim 9.0$ columns are not arranged in a hexagonal lattice, but largely extended along the walls. The centre is found in an isotropic state thereat. With decreasing temperature columns arrange in a hexagonal lattice, columns the layer close to the wall are deformed, though.

We observe a similar trend also in the confined system with $d = 3\sigma_{ee}$. The crystallisation point for the different pressures is also shifted to lower temperatures, but has not been observed in the probed temperature ranges. For pressures above $P^* = 125$ a hexagonal arrangement between columns does not appear any more.

At $P^* = 200$ and $P^* = 225$, a disordered centre occurs again. The centre thereby is filled by a central column and some defects in the remaining space next to the outer layer.

Bibliography

- [1] F. P. Nicoletta, G. Chidichimo, D. Cupelli, G. De Filpo, M. De Benedittis, B. Gabriele, G. Salerno, and A. Fazio. Electrochromic polymer-dispersed liquid-crystal film: A new bi-functional device. *Advanced Functional Materials*, 15(6):995–999, 2005.
- [2] P. T. Ireland and T. V. Jones. Liquid crystal measurements of heat transfer and surface shear stress. *Meas. Sci. Technol.*, 11(7):969, 2000.
- [3] Tsung-Hsien Lin, Yi-Jan Chen, Chun-Hui Wu, Andy Y.-G. Fuh, J.-H. Liu, and P.-C. Yang. Cholesteric liquid crystal laser with wide tuning capability. *Appl. Phys. Lett.*, 86:161120, 2005.
- [4] M. Steinhart D. Gehrig F. Laquai X. Feng K. Müllen HJ. Butt H. Duran, B. Hartmann-Azanza and G. Floudas. Arrays of aligned supramolecular wires by macroscopic orientation of columnar discotic mesophases. *ACS Nano*, 6:9359–9365, 2012.
- [5] Wesley A. Henderson and Stefano Passerini. Phase behavior of ionic liquid-LiX mixtures: Pyrrolidinium cations and tfsi⁻ anions. *Chem. Mater.*, 16:2881–2885, 2004.
- [6] F. Reinitzer. *Monatsh. Chem.*, 9:421, 1888.
- [7] J. W. Goodby, P. J. Colligs, T. Kato, C. Tschierske, H. F. Gleeson, and P. Raynes. *Handbook of Liquid Crystals - Volume 1: Fundamentals of Liquid Crystals*. de Gruyter, 2nd edition, 2014.
- [8] Sergey Sergeev, Wojciech Pisula, and Yves Henri Geerts. *Chem. Soc. Rev.*, 36:1902–1929, 2007.
- [9] Adrian T Gabriel, Timm Meyer, and Guido Germano. Molecular graphics of convex body fluids. *Journal of Chemical Theory and Computation*, 4(3):468–476, 2008.
- [10] J. Gay and B. Berne. Modification of the overlap potential to mimic a linear site-site potential. *J. Chem. Phys.*, 74:3316, 1981.
- [11] M. Steinhart, S. Zimmermann, P. Göring, A. K. Schaper, U. Gösele, C. Weder, and J. H. Wendorff. Liquid crystalline nanowires in porous alumina. *Nano Lett.*, 5:429–434, 2005.
- [12] A. Emerson, G. Luckhurst, and S. Whatling. Computer simulation studies of anisotropic systems XXIII. the Gay-Berne discogen. *Molecular Physics*, 82(1):113–124, 1994.
- [13] M. P. Allen and D.J. Tildesley. *Computer Simulations of Liquids*. Calrendon Press, 1987.
- [14] Thomas Pruschke. Skriptum: Thermodynamik und statistische physik. 2014.
- [15] Seogjoo Jang and Gregory A Voth. Simple reversible molecular dynamics algorithms for nosé–hoover chain dynamics. *The Journal of Chemical Physics*, 107(22):9514–9526, 1997.
- [16] MA Bates and GR Luckhurst. Computer simulation studies of anisotropic systems. xxvi. monte carlo investigations of a gay–berne discotic at constant pressure. *The Journal of Chemical Physics*, 104(17):6696–6709, 1996.
- [17] Andriy V Kityk, Mark Busch, Daniel Rau, Sylwia Calus, Carole V Cerclier, Ronan Lefort, Denis Morineau, Eric Grelet, Christina Krause, Andreas Schönhals, et al. Thermotropic orientational order of discotic liquid crystals in nanochannels: an optical polarimetry study and a landau–de gennes analysis. *Soft Matter*, 10(25):4522–4534, 2014.
- [18] Rémi Busselez, Carole V Cerclier, Makha Ndao, Aziz Ghoufi, Ronan Lefort, and Denis Morineau. Discotic columnar liquid crystal studied in the bulk and nanoconfined states by molecular dynamics simulation. *The Journal of Chemical Physics*, 141(13):134902, 2014.

- [19] Tillmann Stieger, Martin Schoen, and Marco G Mazza. Effects of flow on topological defects in a nematic liquid crystal near a colloid. *The Journal of Chemical Physics*, 140(5):054905, 2014.
- [20] Sylwia Calus, Andriy V Kityk, and Patrick Huber. Molecular ordering of the discotic liquid crystal hat6 confined in mesoporous solids. *Microporous and Mesoporous Materials*, 197:26–32, 2014.
- [21] Iam-Choon Khoo. Liquid crystals: physical properties and nonlinear optical phenomena. *Liquid Crystals: Physical Properties and Nonlinear Optical Phenomena*, by Iam-Choon Khoo, pp. 320. ISBN 0-471-30362-3. Wiley-VCH, December 1994., 1, 1994.
- [22] Pierre-Gilles De Gennes and Jacques Prost. *The physics of liquid crystals*, volume 23. Clarendon Press Oxford, 1993.
- [23] Carole V Cerclier, Makha Ndao, Rémi Busselez, Ronan Lefort, Eric Grelet, Patrick Huber, Andriy V Kityk, Laurence Noirez, Andreas Schönhals, and Denis Morineau. Structure and phase behavior of a discotic columnar liquid crystal confined in nanochannels. *The Journal of Physical Chemistry C*, 116(35):18990–18998, 2012.
- [24] Léon Van Hove. Correlations in space and time and born approximation scattering in systems of interacting particles. *Physical Review*, 95(1):249, 1954.
- [25] Jean Pierre Boon and Sidney Yip. *Molecular hydrodynamics*. Courier Corporation, 1980.
- [26] Didier Caprion, L Bellier-Castella, and J-P Ryckaert. Influence of shape and energy anisotropies on the phase diagram of discotic molecules. *Physical Review E*, 67(4):041703, 2003.
- [27] Jaroslav M Ilnytskyi and Mark R Wilson. A domain decomposition molecular dynamics program for the simulation of flexible molecules of spherically-symmetrical and nonspherical sites. ii. extension to nvt and npt ensembles. *Computer Physics Communications*, 148(1):43–58, 2002.
- [28] GP Crawford, David W Allender, J William Doane, Marija Vilfan, and Igor Vilfan. Finite molecular anchoring in the escaped-radial nematic configuration: A nmr 2 study. *Physical Review A*, 44(4):2570, 1991.
- [29] Gregory Philip Crawford and Slobodan Zumer. *Liquid crystals in complex geometries: formed by polymer and porous networks*. CRC Press, 1996.

Appendix

A.1 Fluid-Wall Force

$$\begin{aligned}
\mathbf{F}_x &= -\partial_x V(\hat{\mathbf{e}}, \mathbf{r}) = -\epsilon_{fw} \left[\partial_x \frac{2}{15} \left(\frac{\sigma_o}{d_w} \right)^9 - \left(\partial_x \left(\frac{\sigma_o}{d_w} \right)^3 \right) g_{orient} - \left(\frac{\sigma_o}{d_w} \right)^3 (\partial_x g_{orient}) \right] \\
&= -\epsilon_{fw} \left[\frac{2 \cdot (-9)}{15} \cdot \left(\frac{\sigma_o^9}{d_w^{10}} \right) \cdot (\partial_x d_w) - (-3) \cdot \left(\frac{\sigma_o^3}{d_w^4} \right) \cdot (\partial_x d_w) \cdot g_{ori} - \left(\frac{\sigma_o}{d_w} \right)^3 (\partial_x g_{ori}) \right] \\
&= -\epsilon_{fw} \left[-3 \cdot \frac{(\partial_x d_w)}{d_w} \left(\frac{2}{5} \cdot \left(\frac{\sigma_o}{d_w} \right)^9 - \left(\frac{\sigma_o}{d_w} \right)^3 \cdot g_{ori} \right) - \left(\frac{\sigma_o}{d_w} \right)^3 (\partial_x g_{ori}) \right] \\
&= \epsilon_{fw} \left[\frac{3}{d_w} \cdot \frac{-x}{|\mathbf{r}|} \left(\frac{2}{5} \cdot \left(\frac{\sigma_o}{d_w} \right)^9 - \left(\frac{\sigma_o}{d_w} \right)^3 \cdot g_{ori} \right) - \left(\frac{\sigma_o}{d_w} \right)^3 (\partial_x g_{ori}) \right] \\
\boldsymbol{\tau}_{e_x} &= -\partial_{e_x} V(\hat{\mathbf{e}}, \mathbf{r}) = -\epsilon_{fw} \left[- \left(\frac{\sigma_o}{d_w} \right)^3 (\partial_{e_x} g_{orient}) \right]
\end{aligned}$$

$$\begin{aligned}
\partial_x g_{orient \parallel} &= \partial_x (\hat{\mathbf{r}} \cdot \hat{\mathbf{e}})^2 = 2 (\hat{\mathbf{r}} \cdot \hat{\mathbf{e}}) \cdot \partial_x \left(\frac{\mathbf{r} \cdot \hat{\mathbf{e}}}{|\mathbf{r}|} \right) \\
&= 2 (\hat{\mathbf{r}} \cdot \hat{\mathbf{e}}) \cdot \left(\frac{|\mathbf{r}| \cdot e_x - \frac{x \cdot \mathbf{r} \cdot \hat{\mathbf{e}}}{|\mathbf{r}|}}{|\mathbf{r}|^2} \right) = 2 (\hat{\mathbf{r}} \cdot \hat{\mathbf{e}}) \cdot \frac{1}{|\mathbf{r}|} \left(e_x - \frac{x \cdot \hat{\mathbf{r}} \cdot \hat{\mathbf{e}}}{|\mathbf{r}|^2} \right)
\end{aligned}$$

$$\begin{aligned}
\partial_x g_{orient \perp} &= \partial_x (1 - |\hat{\mathbf{r}} \cdot \hat{\mathbf{e}}|)^2 = 2 (1 - |\hat{\mathbf{r}} \cdot \hat{\mathbf{e}}|) \cdot \left(-\partial_x \sqrt{(\hat{\mathbf{r}} \cdot \hat{\mathbf{e}})^2} \right) \\
&= 2 (1 - |\hat{\mathbf{r}} \cdot \hat{\mathbf{e}}|) \cdot \left(-\frac{1}{2} \cdot \frac{\partial_x (\hat{\mathbf{r}} \cdot \hat{\mathbf{e}})^2}{\sqrt{(\hat{\mathbf{r}} \cdot \hat{\mathbf{e}})^2}} \right) \\
&= -2 (1 - |\hat{\mathbf{r}} \cdot \hat{\mathbf{e}}|) \cdot \left(\text{sign}(\hat{\mathbf{r}} \cdot \hat{\mathbf{e}}) \cdot \frac{1}{|\mathbf{r}|} \left(e_x - \frac{x \cdot \hat{\mathbf{r}} \cdot \hat{\mathbf{e}}}{|\mathbf{r}|^2} \right) \right)
\end{aligned}$$

$$\partial_{e_x} g_{orient \parallel} = \partial_{e_x} (\hat{\mathbf{r}} \cdot \hat{\mathbf{e}})^2 = 2 (\hat{\mathbf{r}} \cdot \hat{\mathbf{e}}) \cdot \frac{x}{|\mathbf{r}|}$$

$$\begin{aligned}\partial_{e_x} g_{orient \perp} &= \partial_{e_x} (1 - |\hat{\mathbf{r}} \cdot \hat{\mathbf{e}}|)^2 = 2 (1 - |\hat{\mathbf{r}} \cdot \hat{\mathbf{e}}|) \cdot \left(- \partial_{e_x} \sqrt{(\hat{\mathbf{r}} \cdot \hat{\mathbf{e}})^2} \right) \\ &= -2 (1 - |\hat{\mathbf{r}} \cdot \hat{\mathbf{e}}|) \cdot \frac{1}{2} \cdot \frac{2 (\hat{\mathbf{r}} \cdot \hat{\mathbf{e}})}{|\hat{\mathbf{r}} \cdot \hat{\mathbf{e}}|} \cdot \frac{x}{|\mathbf{r}|} \\ &= -2 (1 - |\hat{\mathbf{r}} \cdot \hat{\mathbf{e}}|) \cdot \text{sign}(\hat{\mathbf{r}} \cdot \hat{\mathbf{e}}) \cdot \frac{x}{|\mathbf{r}|}\end{aligned}$$

A.2 Code

A.2.1 Maier-Saupe Theory

This code produces the data shown in Fig. 1.9.

```

1  #include <stdio.h>
2  #include <stdlib.h>
3  #include <math.h>
4  #define PI 3.14159265358
5  #define k.inv (1./1.38e-23)
6  #define Uint 2.5e-20
7
8  char file[300], at[20];
9  FILE * fp;
10 double T, Tinv, Sm, x, x2, Z, N, dZ, up, middle, down, temp, value, increment;
11 int i;
12 double Si(double S);
13
14 int main(int argc, char *argv[])
15 {
16     sprintf(file, "MaierSaupe.dat");
17     fp = fopen(file, "w");
18     increment = .5;
19     for (T = .5; T < 500; T += increment) { // Two parts, for the two solutions
20         Tinv = 1./T;
21         up = 1.;
22         middle = .6;
23         down = .3;
24         for (i = 0; i < 40; i++) {
25             value = Si(middle);
26             if (value > middle) {
27                 down = middle;
28                 middle = (up + middle)/2.;
29             }else{
30                 up = middle;
31                 middle = (down + middle)/2.;
32             }
33         }
34         if (value > (middle - 0.0000001) && value < (middle + 0.0000001))
35             fprintf(fp, "%1f %1f\n", T, middle);
36
37         if (T > 390. && T < 407.)
38             increment = .16666;
39         else
40             increment = .5;
41     }
42     for (T = 410.; T > 350.; T -= increment) {
43         Tinv = 1./T;
44         up = .34;
45         middle = .15;
46         down = .00001;
47         for (i = 0; i < 50; i++) {
48             value = Si(middle);
49             if (value < middle) {
50                 down = middle;
51                 middle = (up + middle)/2.;
52             }else{
53                 up = middle;
54                 middle = (down + middle)/2.;
55             }
56         }
57         if (value > (middle - 0.0000001) && value < (middle + 0.0000001))
58             fprintf(fp, "%1f %1f\n", T, middle);
59
60         if (T > 390. && T < 407.)
61             increment = .16666;
62         else
63             increment = .5;
64     }
65     fprintf(fp, "\n");
66
67     for (T = .5; T < 500; T += increment) {
68         fprintf(fp, "%1f %1f\n", T, 0.);
69
70         if (T > 390. && T < 407.)
71             increment = .25;
72         else
73             increment = .5;
74     }
75     close(fp);
76 }
77 double Si(double S) {
78     int i;
79     Z = 0.;
80     N = 0.;
81     for (i = -2000; i <= 2000; i++)
82     {
83         x = i * 0.0005;
84         x2 = 1.5 * x * x;
85         dZ = 0.001 * exp(Uint * k.inv * S * Tinv * x2);
86         Z += dZ;
87         N += (x2 - .5) * dZ;
88     }
89     Sm = N/Z;
90     return Sm;
91 }

```

A.2.2 Hexagonal Order Parameter

This is a section of the code that produces the data shown in Chapter 3.

```

1
2
3
4
5
6
7
8
9
10
11
12
13
14
15
16
17
18
19
20
21
22
23
24
25
26
27
28
29
30
31
32
33
34
35
36
37
38
39
40
41
42
43
44
45
46
47
48
49
50
51
52
53
54
55
56
57
58
59
60
61
62
63
64
65
66
67
68
69
70
71
72
73
74
75
76
77
78
79
80
81
82
83
84
85
86
87
88
89
90
91
92
93
94
95
96
97
98
99
100
101

```

```

/*****
Hexagonal Order parameter *****/
printf("Calculating Hexagonal Order Parameter   ");
fflush(NULL);

double Hexagonal = 0;
/***** Multithreading *****/
#pragma omp parallel for reduction(+:Hexagonal) schedule( static , CHUNKSIZE )
for ( t=0; t < nconf ; t++ )
{
    printf("\b\b\b\b\b3.0f%%", 100.0*(double)t/(double)nconf);
    fflush(NULL);
    Hexagonal += hexOp ( t );
}
/*****

printf("\b\b\b\b\b100% done");
fflush(NULL);

/***** sum the time array into t = 0 and clear the rest *****/
for ( i = 0 ; i < RCHANNELS ; i++ ) {
    for ( t = 1 ; t < nconf ; t++ ) {
        nem_distrib[0][i] += nem_distrib[t][i] ;
        nem_distrib[t][i] = 0.;
    }
    nem_distrib[0][i] *= 0.005 ; // 1./nconf
}
for ( i = 0 ; i < delta_order ; i++ ) {
    for ( t = 1 ; t < nconf ; t++ ) {
        radialdistri[0][i] += radialdistri[t][i] ;
        radialdistri[t][i] = 0.;
    }
    radialdistri[0][i] *= 0.005 ; // 1./nconf
}

#if CONF
for ( i = 0 ; i < delta_order ; i++ ) /***** The different layers
{
    fprintf( Hshellfp[i] , "%lf %le\n" , temp , radialdistri[0][i] );
    radialdistri[0][i] = 0.;
}

sprintf( fname , "Data/HEX.dist-P%3.1fT%3.2f.dat" , pres , temp );
fp=fopen( fname , "w" );

printf( " , " );
/***** don't forget clearing the first *****/
distance = 0.;
for ( i = 0 ; i < RCHANNELS ; i++ )
{
    distance+=delta_radial;
    fprintf( fp , "%lf %le\n" , distance , nem_distrib[0][i] );
    nem_distrib[0][i] = 0.;
}
fclose( fp );

#endif
fprintf( fpHex , "%lf %lf\n" , temp , Hexagonal/((double) Npart * nconf) );
printf( " written\n" );

double hexOp ( int t )
{
    double rr , u_x , u_y , u_z , r_2 , dx , dy , dz , r_perp , r_para;
    double rpar_x , rperp_x1 , rperp_x2;
    double rpar_y , rperp_y1 , rperp_y2;
    double rpar_z , rperp_z1 , rperp_z2;
    double r , rpar , rperp1 , rperp2 , u_dor_r;
    double real , imagin , tetha , HexOP = 0. ;
    int **neighbours , i , j , l , k , m , count;
    int *channel , *channel2 , index_rad , index_order;
    channel = (int*) calloc( RCHANNELS , sizeof(int) );
    channel2 = (int*) calloc( 6 , sizeof(int) );

    neighbours = calloc( Npart , sizeof( int * ) );
    for ( i = 0 ; i < Npart ; i++ ) {
        neighbours[i] = calloc( 40 , sizeof( int ) );
    }
    /***** Build neighbour list *****/
    for ( i = 0 ; i < Npart ; i++ ) {

        u_x=u[t][i][0];
        u_y=u[t][i][1];
        u_z=u[t][i][2];

        normed:

        for(j = i+1 ; j < Npart ; j++){

            dx=x[t][i][0]-x[t][j][0];
            dy=x[t][i][1]-x[t][j][1];
            dz=x[t][i][2]-x[t][j][2];

#if CONF
            dx=-anint(dx*invL[0])*side[0];
            dy=-anint(dy*invL[1])*side[1];
#endif
            dz=-anint(dz*invL[2])*side[2];

```

```

102
103     u.dor.r = dx*u.x + dy*u.y + dz*u.z ;
104     rpar.x = u.dor.r * u.x ;
105     rpar.y = u.dor.r * u.y ;
106     rpar.z = u.dor.r * u.z ;
107     rpar = rpar.x*rpar.x + rpar.y*rpar.y + rpar.z*rpar.z;
108
109     rperp.x1 = dx - rpar.x;
110     rperp.y1 = dy - rpar.y;
111     rperp.z1 = dz - rpar.z;
112     rperp1 = rperp.x1*rperp.x1 + rperp.y1*rperp.y1 + rperp.z1*rperp.z1;
113
114     if( ( ( rperp1 <= 2.25 ) && ( rperp1 >= .25 ) ) && ( RPARS >= rpar ) ) {
115         neighbours[i][0]++; //first field is a counter
116         neighbours[j][0]++;
117
118         neighbours[i][neighbours[i][0]] = j;
119         neighbours[j][neighbours[j][0]] = i;
120     }
121 }
122 neighbours[i][neighbours[i][0]+1] = -1; //end of list
123 //double len = sqrt( u.x*u.x + u.y*u.y + u.z*u.z );
124 if ( 0 == neighbours[i][0] )
125 {
126     neighbours[i][neighbours[i][0]+2] = -1;
127 }
128 }
129 // ***** end build neighbour list
130
131 for ( i = 0 ; i < Npart ; i++ ) {
132
133     rr = sqrt( x[t][i][0]*x[t][i][0] + x[t][i][1]*x[t][i][1] );
134
135     u.x=u[t][i][0];
136     u.y=u[t][i][1];
137     u.z=u[t][i][2];
138
139     count = 0;
140     double real = 0. , imagin = 0.;
141     for ( k = 1 ; neighbours[i][k+1] != -1 ; k++ ) {
142
143         j = neighbours[i][k];
144         // ***** first intermolecular vector
145
146         dx=x[t][i][0]-x[t][j][0];
147         dy=x[t][i][1]-x[t][j][1];
148         dz=x[t][i][2]-x[t][j][2];
149 #if CONF
150         dx--=anint(dx*invL[0])*side[0];
151         dy--=anint(dy*invL[1])*side[1];
152 #endif
153         dz--=anint(dz*invL[2])*side[2];
154
155         u.dor.r = dx*u.x + dy*u.y + dz*u.z ;
156         rpar.x = u.dor.r * u.x ;
157         rpar.y = u.dor.r * u.y ;
158         rpar.z = u.dor.r * u.z;
159
160         rperp.x1 = dx - rpar.x;
161         rperp.y1 = dy - rpar.y;
162         rperp.z1 = dz - rpar.z;
163         rperp1 = sqrt(rperp.x1*rperp.x1 + rperp.y1*rperp.y1 + rperp.z1*rperp.z1);
164
165         for ( l = k+1 ; neighbours[i][l] != -1 ; l++ ) {
166
167             count++;
168             m = neighbours[i][l];
169             // ***** second intermolecular vector
170
171             dx=x[t][i][0]-x[t][m][0];
172             dy=x[t][i][1]-x[t][m][1];
173             dz=x[t][i][2]-x[t][m][2];
174 #if CONF
175             dx--=anint(dx*invL[0])*side[0];
176             dy--=anint(dy*invL[1])*side[1];
177 #endif
178             dz--=anint(dz*invL[2])*side[2];
179
180             u.dor.r = dx*u.x + dy*u.y + dz*u.z ;
181             rpar.x = u.dor.r * u.x ;
182             rpar.y = u.dor.r * u.y ;
183             rpar.z = u.dor.r * u.z;
184
185             rperp.x2 = dx - rpar.x;
186             rperp.y2 = dy - rpar.y;
187             rperp.z2 = dz - rpar.z;
188             rperp2 = sqrt(rperp.x2*rperp.x2 + rperp.y2*rperp.y2 + rperp.z2*rperp.z2);
189
190             // ***** angle projected on the plane perpendicular to e.i
191
192             tetha = acos( ( rperp.x1*rperp.x2 + rperp.y1*rperp.y2 + rperp.z1*rperp.z2 ) / (rperp1*rperp2) );
193             real += cos( 6. * tetha );
194             imagin += sin( 6. * tetha );
195
196         }
197     }
198     real = sqrt( real*real + imagin*imagin ) / ((double) count);
199     if ( !isnan(real) )
200     {
201         HexOP += real ;
202
203         index.rad = ( rr ) / delta.radial;
204         index.order = rr ;
205
206         channel2[index.order]++;
207         radialdistrib[t][index.order] += real;

```

```
208     channel[index.rad]++;
209     nem_distrib[t][index.rad] += real ;
210
211 }
212
213 }
214 for ( i = 0 ; i < Npart ; i++) {
215     free( neighbours[i] );
216 }
217 free( neighbours );
218 for ( i = 0 ; i < R_CHANNELS ; i++ ) {
219     if( channel[i] > 0 )
220         nem_distrib[t][i] /= channel[i] ;
221 }
222 for ( i = 0 ; i < delta_order ; i++ ) {
223     if( channel2[i] > 0 )
224         radialdistri[t][i] /= channel2[i];
225 }
226 free(channel);
227 free(channel2);
228 return HexOP ;
229 }
```

Acknowledgements

I want to thank my friends and family very much for supporting me the whole time. Thanks to Marco G. Mazza for the steady help and encouragement. I was also very happy about the nice and very friendly working environment at the MPIDS, the company and help from all the group members. I also want to thank my flatmates for tolerating the dirty kitchen.

Erklärung

nach §13(8) der Prüfungsordnung für den Bachelor-Studiengang Physik und den Master-Studiengang Physik an der Universität Göttingen:

Hiermit erkläre ich, dass ich diese Abschlussarbeit selbständig verfasst habe, keine anderen als die angegebenen Quellen und Hilfsmittel benutzt habe und alle Stellen, die wörtlich oder sinn- gemäß aus veröffentlichten Schriften entnommen wurden, als solche kenntlich gemacht habe. Darüber hinaus erkläre ich, dass diese Abschlussarbeit nicht, auch nicht auszugsweise, im Rahmen einer nichtbestanden Prüfung an dieser oder einer anderen Hochschule eingereicht wurde.

Göttingen, den 13. Mai 2015

(Arne Wolf Zantop)